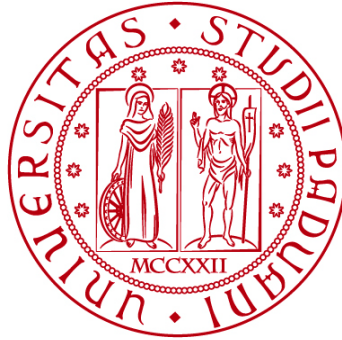


UNIVERSITÀ DEGLI STUDI DI PADOVA

DIPARTIMENTO DI BIOLOGIA

Corso di Laurea in Biologia Molecolare



ELABORATO DI LAUREA

Cellule mieloidi che esprimono trombospodina1, in associazione a TREM1, sono arricchite nel carcinoma epatocellulare associato a steatosi epatica contribuendo a creare un ambiente immunosoppressivo e ad una prognosi sfavorevole.

**Tutor: Dott.ssa Gaia Codolo
Dipartimento di Biologia**

Laureanda: Francesca Cornea

ANNO ACCADEMICO 2023/2024

INDICE

1. STATO DELL'ARTE	5
1.1 CARCINOMA EPATOCELLULARE (HCC)	5
1.2 HCC ASSOCIATO A PATOLOGIE STEATOSICHE EPATICHE SLDs	6
1.3 MICROAMBIENTE TUMORALE	6
1.3.1 Componente stromale CAF	6
1.3.2 Componente immunitaria linfoide	7
1.3.3 Componente immunitaria mieloide	7
1.4 RECETTORE TREM1	8
2. APROCCIO SPERIMENTALE	9
2.1 MODELLO ANIMALE	9
2.2 GENERAZIONE DI CELLULE SOPPRESSORIE DI ORIGINE MONOCITA DI DERIVAZIONE UMANA HU _M OSC	9
2.3 DISSOCIAZIONE DI TESSUTI UMANI E PREPARAZIONE PER LA CITOMETRIA A FLUSSO	9
2.4 SINGLE-CELL FACS SORTING	10
2.5 SCRNA-SEQ	11
2.6 ESPERIMENTI DI CO-COLTURA	11
2.7 TRASCRIPTOMICA SPAZIALE	12
2.8 KNOCK-OUT DI TREM1 MEDIANTE CRISPR/CAS9	12
3. RISULTATI	14
3.1 DEFINIZIONE DELL'INFILTRATO IMMUNITARIO INNATO NEL HCC	14
3.2 RE-CLUSTERING DI CELLULE MIELOIDI	14
3.3 RICLASSIFICAZIONE DELLA COMPONENTE MIELOIDE IN HCC E IDENTIFICAZIONE DI 3 SOTTOGRUPPI DI CELLULE THBS1 ⁺	15
3.4 IDENTIFICAZIONE DEL SOTTOGRUPPO CELLULARE THBS1 ⁺ M _{REG} COME UN PRINCIPALE RESPONSABILE DELL'IMMUNOSOPPRESSIONE	17
3.5 CORRELAZIONE SPAZIALE TRA LE CELLULE THBS1 ⁺ REG E LESIONI FIBROTICHE	18
3.6 LE CELLULE THBS1 ⁺ M _{REG} SONO CORRELATE A ESITI CLINICI NEGATIVI E SONO PARTICOLARMENTE ABBONDANTI IN PATOLOGIE DI HCC ASSOCIATO A SLD	19
3.7 RUOLO DEL RECETTORE TREM1 ED EFFETTI DI UNA SUA INIBIZIONE	20
4. DISCUSSIONI E LIMITI DELLO STUDIO	23
BIBLIOGRAFIA	26

ABSTRACT

Il carcinoma epatocellulare è una tra le neoplasie più comuni nel mondo, l'insorgenza dell'epatocarcinoma può essere associato a infezioni virali o essere correlato ad un eccessivo consumo di alcool e disfunzioni metaboliche. Numerosi studi hanno dimostrato il ruolo cruciale svolto dal microambiente tumorale nel determinare la risposta alle terapie, evidenziando quanto alcune popolazioni di cellule mieloidi possano inficiare l'efficacia dell'immunoterapia. Risulta pertanto di fondamentale importanza caratterizzarne in modo sempre più preciso l'eterogeneità al fine di definire il ruolo preciso nella resistenza all'immunoterapia. In particolare, nei pazienti con carcinoma epatocellulare associato a steatosi, è stata rilevata una porzione abbondante di cellule mieloidi THBS1⁺, che presentano geni affini a monociti e neutrofili, caratterizzate dalla co-espressione di TREM1 e CD163. Si ritiene che queste cellule contribuiscano a generare un ambiente immunosoppressivo e che la loro presenza sia associata a una prognosi sfavorevole. La loro capacità immunosoppressiva è associata al Triggering receptor expressed on myeloid cells 1 (TREM1), recettore che è espresso da granulociti, monociti e macrofagi tissutali.

Sono stati eseguiti test su modelli murini in cui si andava ad inibire TREM1, osservando come l'inibizione di quest'ultimo portava ad una rapida eradicazione del tumore. Questi risultati hanno portato ad identificare le cellule THBS1⁺ M_{reg} come marcatori della patologia HCC e un potenziale target immunoterapeutico.

1. STATO DELL'ARTE

1.1 Carcinoma epatocellulare (HCC)

Il carcinoma epatocellulare rappresenta il tumore primario al fegato più comune ed è una delle principali cause di morte correlate a cancro nel mondo. Le cellule responsabili dell'insorgenza della patologia sono gli epatociti e nel 85% dei casi viene riscontrata in pazienti affetti da cirrosi. Tra i fattori che ne portano l'insorgenza possono esservi: epatite B e epatite C, malattie al fegato associate ad un consumo di alcol e steato epatite non alcolica, e alla base di quest'ultima si ha spesso una sindrome metabolica, che si associa ad obesità e ad insulino resistenza aumentata.

Gli epatociti, che sono le principali cellule del fegato, in questo contesto assumono aspetto tumorale con una morfologia alterata. Basandosi sull'aspetto di tali cellule cancerogene, è possibile avere una classificazione del tumore in tre principali categorie: ben differenziato, in cui le cellule tumorali, rispetto agli epatociti sani, risultano essere più piccole e presentano una densità nucleare doppia incrementando il rapporto nucleo/citoplasma, ma comunque con una diversità non particolarmente accentuata; moderatamente differenziato, in cui le cellule sono più grandi del normale con un'abbondanza citoplasmatica evidente, inoltre presentano nucleoli ben distinti, accumulo di bile al loro interno e spesso si organizzano formando strutture ghiandolari. L'ultima tipologia di neoplasia è definita scarsamente differenziata, contraddistinta dalle altre per la presenza di cellule tumorali con un aspetto fortemente alterato rispetto agli epatociti normali: generalmente sono multinucleate, presentano grandi dimensioni, citoplasma abbondante, nuclei pleiomorfici e ipercromatici.

L'epatocarcinoma è un tumore in rapida espansione, e vi sono in corso di sviluppo diverse terapie per la sua eradicazione attuate in base alla stadiazione e alle caratteristiche morfologiche del tumore stesso. Quando il paziente si trova in una stadiazione precoce, stadio 0 e 1, il trattamento ideale sarebbe quello di incorrere al trapianto di fegato, attuabile solo nel caso in cui il carcinoma si presenta con un solo nodulo di grandezza non maggiore di 5 cm, o con un massimo 3 noduli, ciascuno di dimensione massima di 3 cm; nel caso in cui il paziente non dovesse rispecchiare questi requisiti si ricorre all'ablazione tumorale. Nella maggior parte dei casi però la diagnosi avviene ad uno stadio avanzato non potendo più ricorrere a questi metodi, sfruttando trattamenti che tutt'ora danno scarsi risultati, tra cui l'utilizzo di inibitori della tirosin chinasi. Negli ultimi anni ci si è invece spostati verso un trattamento focalizzato sull'immunoterapia, sfruttando inibitori di checkpoint immunitari come trattamento di prima linea; nonostante al momento neanche questo approccio risulti essere particolarmente efficace si è comunque notata un'importante differenza della risposta immunoterapica tra individui con eziologie diverse di HCC. Questo si verifica principalmente a causa del diverso microambiente tumorale che influisce sull'efficienza dell'immunoterapia, con scarsi risultati principalmente in coloro che manifestano una condizione di steatosi.[1]. In accordo con la differente risposta all'immunoterapia in base all'eziologia patologica, è interessante mettere a confronto la composizione totale di cellule mieloidi del microambiente tumorale tra i diversi pazienti.

1.2 HCC associato a patologie steatosiche epatiche SLDs

Uno dei principali fattori in aumento negli ultimi anni che contribuisce all'insorgenza di HCC è la presenza di patologie steatosiche epatiche raggruppate sotto il nome SLD comprendenti sia disfunzioni metaboliche associate a steatoepatite non alcolica (NAFLD) che steatoepatite associata ad un eccessivo consumo di alcool (ALDS). La NAFLD è una patologia relazionata ad obesità e sindromi metaboliche, caratterizzata da una prima stadiazione con manifestazione patologica lieve, ma che può sfociare in una patologia più grave (NASH) associata ad un maggior rischio di mortalità e incidenza di fibrosi epatica progressiva. Il metabolismo di acidi grassi, presenti in abbondanza negli epatociti di individui affetti da NASH, porta ad un aumento di specie reattive dell'ossigeno ROS e conseguente danno al DNA, incrementati data l'incapacità delle cellule di intervenire per la riparazione dei danni. Il rischio di insorgenza di HCC è maggiore nei pazienti che presentano la forma più acuta di steatosi epatica, influenzata sia da un aumento di ligandi di recettori nucleari pro-tumorali derivati dal metabolismo anomalo del colesterolo, che per la presenza di cellule immunitarie e citochine non consone che favoriscono la tumorigenesi.

Nel caso di pazienti affetti da ALD, si ha un aumento del tasso di mortalità nel momento in cui si incorre nello sviluppo di una forma aggravata (ASH), dove vi è un'insufficienza epatica acuta cronica, con un maggior rischio di sfociare in una condizione di carcinogenesi epatica. Questa è favorita dalla sintesi di acetaldeide e specie reattive dell'ossigeno, e da una modifica indotta a livello del sistema immunitario; infatti l'abuso di alcool porta ad una mancata sorveglianza nei confronti del tumore e influisce sulla permeabilità intestinale, permettendo l'ingresso nel fegato del lipopolisaccaride LPS di origine batterica, che viene riconosciuto dal recettore TLR4 delle cellule Kupffer portando alla sintesi di citochine pro infiammatorie, sostenendo ulteriormente l'epatocarcinogenesi. [3]

1.3 Microambiente tumorale

Il microambiente tumorale e la sua composizione è un fattore fondamentale per la messa a punto di terapie mirate ed efficaci, e risulta quindi necessario approfondirne la composizione. Nonostante questa sia peculiare per ciascuna patologia, si ha la costante presenza di cellule immunitarie e stromali, vasi sanguigni e componenti della matrice extracellulare. Comprende però anche altre due componenti che sono le principali responsabili del mantenimento e progressione tumorale: cellule infiltranti il tumore che risiedono nel microambiente penetrando nel tessuto stesso e cellule tumorali residenti nel tessuto con la capacità di alterarne la morfologia. [4]

1.3.1 Componente stromale CAF

La componente cellulare stromale varia a seconda del tumore considerato e solitamente comprende cellule endoteliali vascolari, fibroblasti, adipociti e cellule stellate. I fibroblasti in una situazione non patologica secernono componenti della matrice extracellulare, agiscono come cellule di segnalazione, costituiscono i progenitori di cellule di linee mesenchimali e sono anche modulatori di funzioni immunitarie, sia adattative che innate. Quando invece si è in una condizione di

carcinogenesi, vengono denominati fibroblasti associati al cancro CAFs che attivati da TGF- β e altri fattori rilasciati dagli epatociti danneggiati.

Nella condizione di HCC i CAFs possono derivare da cellule stellate epatiche che a causa della presenza di danno epatico cronico differenziano, fibroblasti portalici, fibrociti, o in seguito a cellule epiteliali che vanno in contro al fenomeno di transizione epitelio-mesenchima, acquisendo fenotipo migratorio e l'espressione di marcatori tipici mesenchimali. La rigidità epatica sembrerebbe essere uno dei principali fattori a rischio che porta l'insorgenza di HCC, e questa è indotta dai CAFs, che partecipando al rimodellamento della matrice extracellulare, inducono un'eccessiva deposizione di collagene fibrillare, generando irrigidimento della matrice e promuovendo proliferazione e invasione delle cellule tumorali. Il loro ruolo è sostenuto dal fatto che producono una serie di citochine e proteine a sostegno della metastasi e mediano il cross-talk con cellule immunitarie. [5]

1.3.2 Componente immunitaria linfoide

Nel microambiente tumorale vi è anche la componente linfoide, costituita da cellule T, cellule B e Natural Killer NK.

Il microambiente immunitario tumorale (TIME) è costituito da diverse tipologie di linfociti T che influenzano la tumorigenesi: tra le più ricorrenti vi sono i CD8⁺ che hanno ruolo citotossico bersagliando cellule tumorali e sopprimendo l'angiogenesi, a supporto di queste vi sono i linfociti T helper CD4⁺, in particolare la sottocategoria T_{H1} che assume ruolo pro-infiammatorio sintetizzando IL-2 e IFN- γ . In HCC si è riscontrata la presenza di cellule T CD8⁺ disfunzionali, identificate a causa della ridotta proliferazione e capacità di produrre molecole effettrici. I linfociti T regolatori invece hanno il ruolo di sopprimere la risposta infiammatoria ed evitare che vi siano eventuali azioni autoresponsive da parte dei T stessi; la loro funzione è associata anche ad una capacità di smorzare le risposte antitumorali, supportando però la progressione della patologia. Una loro abbondanza in HCC è tipicamente correlata a prognosi sfavorevole in quanto interferiscono con le attività citotossiche dei linfociti T CD8⁺.

Nonostante i linfociti B siano meno presenti rispetto ai T nel microambiente, nuove evidenze hanno mostrato una potenziale capacità da parte di queste cellule nel mediare un cross-talk tra sistema immunitario adattativo e cancro, e di come l'immunoglobulina IgA possa alterare la funzionalità citotossica dei T CD8; inoltre un'infiammazione cronica promuove la formazione di cluster di linfociti B secondo un'organizzazione spaziale che allude ad organi linfoidi secondari, definiti strutture linfoidi terziarie, con un ruolo anti o pro-tumorale. [1]

Le NK invece sono cellule citotossiche che possono agire nei confronti della cellula bersaglio con meccanismo cellulo-mediato, oppure possono produrre citochine; in ogni caso la loro funzione citotossica risulta più efficiente in circolo sanguigno piuttosto che nell'ambiente tumorale.

1.3.3 Componente immunitaria mieloide

La componente mieloide presente nel microambiente tumorale comprende principalmente macrofagi, neutrofili e cellule dendritiche.

La categoria dei macrofagi associati al tumore (TAM) comprende un gruppo di cellule che modulano la risposta immunitaria innata e si possono suddividere in due sottocategorie sulla base dei mediatori che le hanno attivate e delle loro proprietà: gruppo M1 comprende macrofagi infiammatori, implicati nella fagocitosi e uccisione di patogeni che vengono attivati da IFN γ , TNF α e GMS-CSF. Il gruppo M2 è sostenuto da un ambiente ipossico e dalle citochine IL-4, IL-10, IL-13 e comprende cellule che hanno ruolo immunosoppressorio promuovendo la crescita del tumore data la loro capacità di reclutare cellule T regolatorie. Alla macrocategoria dei TAM epatici appartengono anche le cellule di Kupffer che risiedono a livello del fegato.

I neutrofili costituiscono circa il 70% dei leucociti circolanti, non hanno un ruolo pre-stabilito, ma possono sia inibire che favorire la crescita tumorale.

Le cellule dendritiche invece sono importanti in quanto fanno da collegamento tra sistema immunitario innato e adattativo, e hanno la funzione di presentare gli antigeni a linfociti T naïve attivandoli ad effettori. Il TIME in questo caso ha un'azione modulatoria su queste cellule, portandole ad avere un profilo tollerante nei confronti di cellule tumorali sopprimendo l'insorgenza di una risposta immunitaria. Vi è un ulteriore gruppo di cui fanno parte cellule soppressive di derivazione mieloide MDSC che nella condizione di fegato tumorale partecipano alla progressione del tumore producendo TGF- β che inibisce la proliferazione di linfociti T e delle NK, inoltre aumenta la neoangiogenesi e promuove la polarizzazione di tipo M2 dei TAM.[6]

1.4 Recettore TREM1

Alla famiglia dei recettori TREM appartengono i recettori della superficie cellulare di granulociti, monociti e macrofagi, e tra questi vi sono TREM1 e TREM2. Sebbene questi due abbiano una struttura simile la loro funzione è estremamente diversa in quanto TREM2 inibisce l'infiammazione e al contrario vi è TREM1 che la stimola mediante la produzione di citochine pro-infiammatorie.

TREM1 viene codificato da un gene che si trova sul cromosoma 6p21 umano, presenta 2 isoforme una di membrana e una citosolica; mTREM1 di membrana ha massa molecolare di 30 kDa, 234 aminoacidi ed è costituito da 3 regioni: un dominio citoplasmatico, un dominio immunoglobulinico extracellulare, responsabile del legame ai ligandi, una regione transmembrana che, una volta attivato il recettore, si associa alla proteina DAP12, importante per l'attivazione di domini ITAM permettendo di avviare una cascata di segnalazioni a valle. [7]

In seguito a necrosi cellulare e la morte degli epatociti, vengono rilasciate numerose molecole, tra le quali la proteina della cromatina HMGB-1, interagiscono con il recettore TREM-1 sulla superficie delle cellule mieloidi e con i TLRs che attivano il pathway di segnale a valle portando all'attivazione di fattori di trascrizione, tra i quali NF-kB e conseguente produzione di citochine pro-infiammatorie (IL-6, TNF- α); sebbene queste in un primo momento risultano svolgere una funzione positiva, possono poi assumere ruolo negativo esacerbando l'infiammazione e la produzione di fattori di trascrizione. Questo si verifica anche a causa di una massiccia espressione di TREM1, sostenuta sia dalle citochine, che dal fattore NF-kB. [8][9]

2. APROCCIO SPERIMENTALE

2.1 Modello animale

Per l'esperimento trattato in questo articolo gli studiosi hanno utilizzato i topi come modello animale assegnandoli casualmente ai gruppi sperimentali e alle diverse condizioni ancora prima di iniziare l'esperimento. I topi adoperati appartengono alla linea C57BL/6J e sono tutti di sesso maschile e dall'età di circa 8-10 settimane sono stati mantenuti in un ambiente supervisionato in cui vi era assenza di agenti patogeni, un'umidità compresa tra 50% e 70%, una temperatura mantenuta intorno ai 20-22 ° C, ed esposti a 12h di luce alternate ad altrettante ore di buio. Questi periodicamente ricevevano acqua e cibo in quantità controllata.

2.2 Generazione di cellule soppressorie di origine monocita di derivazione umana HuMoSC

È di rilevante importanza avere a disposizione un pool di cellule con caratteristiche immunosoppressorie, sia per il trattamento di disturbi immuno-mediati che per poter condurre eventuali analisi. Per la generazione delle cellule soppressorie di origine monocita di derivazione umana HuMoSC, si è seguito un protocollo che prevedeva prima l'isolamento di cellule mononucleate del sangue periferico (PBMC), a partire da campioni di sangue contenenti la maggior parte di globuli bianchi e piastrine di donatori sani tramite centrifugazione del gradiente di densità di Ficoll. Poi dalle PBMC sono stati isolati i monociti mediante centrifugazione di gradiente di densità Percoll, e poi si sono messe in coltura con RPMI 20% FBS, fattore di crescita M-CSF umano ricombinante e IL-6 per 7 giorni. La IL-6 è una citochina che se prodotta in quantità sproporzionata ha un ruolo patologico inducendo infiammazione cronica e autoimmunità.

Nell'arco di questi 7 giorni il medium veniva cambiato del 60% ogni tre giorni, e al sesto giorno è stato aggiunto PGLYRP1 complessato ad un peptidoglicano (complesso PP) per 24 ore.

2.3 Dissociazione di tessuti umani e preparazione per la citometria a flusso

Per poter compiere un'analisi con la citometria a flusso è necessario prima preparare adeguatamente i campioni.

Si parte raccogliendo i tessuti umani in un medium indipendente dalla CO₂ e mantenuti in ghiaccio fino ad 1h prima dell'utilizzo. Una fetta istologica è stata assegnata alla fissazione e colorazione istologica con emotossina-eosina-safranina e Tricromo di Masson, una seconda fetta è stata preparata per la crioconservazione, mentre l'ultima porzione è stata adoperata per la dissociazione. Questa sezione istologica è stata sottoposta inizialmente ad un risciacquo in RPMI, e poi taglia in pezzettini con dimensione entro i 2mm³ in una piastra di coltura sterile. Questi sono stati poi posti in tubi Gentle MACS C e incubati in una soluzione per la

dissociazione del tessuto usufruendo del kit di dissociazione tumorale Milteny, e del dissociatore Gentle MACS C. I campioni sono stati poi centrifugati a 400 xg per 8 minuti a 4°C, filtrati attraverso un filtro da 40µm, risciacquati in RPMI e infine centrifugati nuovamente alla stessa velocità e temperatura ma per 5 minuti. Si è proseguito poi con l'eliminazione dei globuli rossi inducendone la lisi mediante la soluzione Roche. Per evitare l'interferenza con le analisi a cui dovranno essere sottoposti i campioni, si sono fatti 2 lavaggi con buffer FACS contenente PBS, 2mM EDT e 0,1 PBS limitando la formazione di aggregati cellulari. Le cellule dissociate vengono mantenute nel FACS buffer con anticorpi contro marker di superficie cellulare per 25 min a 4°C; questo passaggio si può in alternativa fare anche a temperatura ambiente, mantenendo il campione al buio per 15 minuti, in entrambi i casi vengono fatti altri due lavaggi prima di proseguire con l'analisi. Per la colorazione delle citochine intracellulari, le cellule sono state prima fissate e permeabilizzate in una soluzione apposita. Le cellule derivanti dai campioni murini sono state prima incubate con anticorpi anti-topo CD16/32 in concentrazione 1:200, per bloccare eventuali siti aspecifici, e poi con gli anticorpi che riconoscono molecole di superficie.

2.4 Single-cell FACS sorting

La tecnica del single-cell FACS sorting viene usata per purificare sottopopolazioni di cellule di una sospensione eterogenea sulla base delle loro caratteristiche fenotipiche, sfruttando la citometria.

È fondamentale che i campioni vengano caricati mediante un sistema fluidico in grado di allineare le singole cellule in fila facendole fluire una alla volta per avere una corretta separazione tra le diverse cellule evitando una sovrapposizione di segnale; e queste verranno successivamente irradiate mediante un raggio laser. La luce deviata dalla cellula, definita "scatter", è in grado fornire informazioni riguardanti la dimensione (forward scatter) e granulosità (side scatter) della singola cellula, mentre la fluorescenza di emissione permette di identificare gli anticorpi ad esse coniugati.

Per gli esperimenti di immunosoppressione le singole cellule tumorali precedentemente dissociate vengono scongelate in RPMI completo e incubate per 10 minuti a 37°C per eliminare il DMSO residuo e poi pellettate e risospese nel tampone FACS freddo, procedendo infine con la colorazione mediante anticorpi di superficie adoperando: Vi-green-CD45⁺ APC Vio770-Lin⁻ (identifica CD3, CD19 e CD56) FITC-CD36⁺ PE-Vio880-CD163^{+/-} APC-LOC1^{+/-}. Vengono prima analizzate le cellule vitali mediante il colorante di vitalità "Sytox blue" in concentrazione 1:5000 e le caratteristiche date dalla "side scatter".

Le cellule vengono separate e analizzate mediante FACS Aria II a 4°C e raccolte in eppendorf a bassa adesione da 1,5 mL, precedentemente trattate con PBS 10% FCS per 2 ore a 37°C, nel caso in cui le cellule dovessero essere adibite all'analisi di scRNA-seq vengono raccolte in PBS-0,04% BSA puro, per gli esperimenti di co-coltura la raccolta avviene in RPMI completo.

In questo esperimento per la successiva analisi di scRNA-seq, vengono selezionate le cellule positive per FITC-CD45 e le cellule negative per Apc Vio770panTCRαβ e PE Vio770-CD19.

2.5 scRNA-seq

La tecnica del Single cell RNA sequencing, è stata messa a punto nel 2009, fornisce il trascrittoma della singola cellula consentendo di rilevare l'eterogeneità e complessità della popolazione di RNA. La maggior parte delle cellule di un organismo presentano lo stesso assetto genomico, con gli stessi geni e le stesse varianti alleliche, ma ciò che le differenzia è la popolazione di mRNA trascritti. Questo evidenzia che l'attivazione dei geni non avviene allo stesso modo in tutte le cellule, e che l'espressione genica ha una grossa influenza sullo stato, l'identità, la funzione e le risposte cellulari.

Per la scRNA-seq vengono utilizzate le cellule dell'immunità innata precedentemente separate e selezionate mediante single cell-FACS sorting. All'interno di un chip vengono caricate 15000 cellule, assieme alla trascrittasi inversa RT, sfere di gel ciascuna con una sequenza oligonucleotidica lunga 10 pb che funge da indice (Barcode Gel Beads), e un olio di ripartizione, per permettere la formazione di sfere di Gel (GEMs). Ciascuna di queste vescicole neoformate contiene al suo interno un'unica cellula, una Barcode Gel Bead e una RT, e una volta fatta partire la reazione di trascrizione tutti i cDNA che ne derivano presenteranno la stessa sequenza indice in comune.

Vengono prima effettuati 12 cicli di PCR per l'amplificazione del cDNA, e in seguito altri 12 per la preparazione della libreria, queste vengono raggruppate e poi sequenziate mediante NovaSeq 6000, questo ultimo step permette di risalire alla sequenza codificante.

2.6 Esperimenti di co-coltura

Per valutare e confermare il potere immunosoppressivo delle cellule THBS1⁺ nei confronti dei linfociti T si è allestita una co-coltura con il sottogruppo di cellule mieloidi derivate da sezioni di tumore e una componente linfoide costituita da linfociti T.

In un primo test si fa una co-coltura tra cellule mieloidi che sono state pre-incubate per 4 ore in piastra da 96 pozzetti in rapporto 5:1 con un clone di linfociti T CD4⁺ reattivi nei confronti della trascrittasi inversa della telomerasi (TERT) e sottoposti a stimolazione per 12 ore con peptidi UCP4 TERT concentrati 1 µg/mL per indurre una risposta immunitaria in presenza di 1 µg/mL di BD Golgi Plug, inibitore del trasporto di citochine dal reticolo endoplasmatico all'apparato di Golgi permettendo il loro accumulo all'interno della cellula. Per il controllo invece le cellule T sono state trattate mediante ionomicina 0,5 µg/mL e stimulate con Phorbol 12-myristate 13-acetate (PMA) a 12,5 ng/mL responsabile dell'attivazione della proteina chinasi C. La combinazione delle sostanze induce una stimolazione forte ma aspecifica, necessaria per valutare la capacità funzionale dei linfociti T.

In un altro esperimento invece si sono utilizzati linfociti T purificati mediante un kit di isolamento basato su una selezione magnetica a partire da pool di cellule mononucleate del sangue prelevate da donatori sani, attivati mediante l'utilizzo di sfere rivestite con anti-CD3/CD28 e co-coltivate sia in assenza che in presenza di cellule mieloidi, derivanti o da resezioni chirurgiche di HCC o dal gruppo delle HuMoSC, in rapporto 1:1 e 1:4.

In entrambi i casi le cellule vengono pellettizzate, risospese nella soluzione FACS e trattate prima con una soluzione di anticorpi contro molecole della superficie cellulare (CD4-PE Vio770 e CD3-APC-Vio770). In seguito a lavaggio, fissazione e successiva permeabilizzazione vengono trattati con una seconda soluzione di anticorpi che riconoscono molecole intracellulari (IFN γ -APC e TNF-FITC). Confrontando la percentuale di cellule T che risultano essere positive per TNF α ⁺ CD4⁺ o CD8⁺ in seguito alla stimolazione con UCP4 TERT nel primo caso, o con anti-CD3/CD28 nel secondo caso; e la percentuale delle cellule T con la stessa caratteristica di positività nei vari campioni che vengono testati, permette di avere una stima del potere immunosoppressorio di queste cellule.

2.7 Trascrittomica spaziale

Data la necessità di avere informazioni precise riguardanti le possibili interazioni che si instaurano tra le diverse popolazioni cellulari diverse e l'ambiente tumorale, è stata messa appunto la tecnica della trascrittomica spaziale. Permette di avere informazioni sull'eterogeneità del tessuto in termini di localizzazione spaziale di determinati trascritti o gruppi cellulari.

In questo articolo viene adoperata per verificare il possibile cross-talk tra le cellule fibrotiche CAF e l'ambiente tumorale, con tutte le sue componenti annesse.

I dati spaziali ottenuti vengono sottoposti prima ad una pre-elaborazione e poi si passa all'allineamento con il genoma umano di riferimento GRCh38 mediante il software Space ranger che fornisce i risultati sotto forma di una matrice di conteggio UMI grezzi per ogni regione epatica. Per rendere adeguato l'eventuale confronto tra dati derivati da campioni diversi viene successivamente fatta una normalizzazione dei dati mediante la tecnica SCTransform e una riduzione della dimensionalità. In un primo momento si definiscono i diversi gruppi cellulari basati sull'espressione genica effettuata mediante l'algoritmo di clustering Louving con le funzioni FindNeighbors e FindCluster e poi tramite la funzione AddModuleScore viene calcolato il punteggio di specifici gruppi di geni (firme geniche). Sulla base di questi valori si selezionano le regioni di tessuto epatico, definite spot, che con una probabilità maggiore di 0,9 risultano positive ad una determinata firma genica.

L'analisi si focalizza poi sugli spot co-localizzati, ovvero quelli in cui si ha positività per due firme geniche differenti, ad indicare che vi è co-presenza di determinati tipi cellulari.

Mediante la regressione lineare si stabilisce come varia la co-localizzazione nelle diverse condizioni considerate, e per mezzo del test del Chi-quadrato di Pearson si stabilisce se vi è una differenza significativa nel numero di spot co-localizzati tra regioni fibrotiche e non fibrotiche in contesto HCC.

2.8 Knock-out di TREM1 mediante CRISPR/Cas9

La tecnologia CRISPR-Cas9 è un approccio di ingegneria genetica che permette di modificare una porzione del genoma di interesse in maniera semplice, rapida ma

allo stesso tempo precisa. In questo caso viene adoperata per generare topi Knock-out per il gene codificante TREM1.

Questo sistema prevede l'utilizzo di un RNA guida che è complementare alla sequenza che si vuole trargettare e l'endonucleasi cas9 associata a CRISPR che verrà guidata dal nostro sgRNA a livello della sequenza target.

Per la sintesi degli RNA guida specifici nei confronti del gene di interesse vi sono vari software validi, nel nostro caso è stato usato CRISPOR, generando due sequenze di RNA guida a singolo filamento sgRNA che andassero a bersagliare in maniera precisa il gene codificante TREM1. La molecola Alt-R-crRNA, ovvero quella deputata all'indirizzamento dell'enzima cas9 a livello della sequenza di DNA d'interesse, e le 2 molecole umane crRNA che fungono una da controllo negativo e uno positivo nei confronti di HPRT, acquistati dall'IDT (Integrate DNA technologies). È fondamentale avere i due controlli, positivo e negativo, per garantire la specificità della tecnica e valutarne l'efficacia facendo un confronto con questi. Queste sono state risospese in 200 μ M in un buffer di TE e successivamente equamente mescolate con 200 μ M Alt-R-tracrRNA, ibridati riscaldandoli a 95° C per 5 minuti e successivamente fatti raffreddare a temperatura ambiente. I due gRNA sono stati separati e mescolati ciascuno in un rapporto 1.6 con 10 μ g di Alt-R S.p-Cas9HIF1v3. Dopo 10 minuti a temperatura ambiente vengono aggiunti a questa mix dei monociti in una quantità che va dai 2,5 ai 2,8 milioni, e che erano precedentemente lavati in PBS e risospesi in 20 μ L di soluzione Lonza P3 contenente mix di sostanze elettrolitiche, tamponi per mantenere il pH e 1 μ g di un additivo per favorire l'efficacia dell'elettroporazione.

3. RISULTATI

3.1 Definizione dell'infiltrato immunitario innato nel HCC

È stata condotta una prima analisi su 10 pazienti affetti da HCC per valutare la differenza della composizione immunitaria tra tessuto tumorale e tessuto non tumorale adiacente, in un primo momento mediante la tecnica del single cell RNA FACS sorting e poi ampliata mediante la trascrittomica spaziale.

Si sono identificati 11 gruppi di linfociti innati comprendenti un sottogruppo di cellule linfoidi innate di tipo 3 e 10 di Natural Killer tra cui un cluster di cycling NK, due cluster di NK1 citotossici, 4 cluster di NK2 di cui 2 esprimenti effettori antinfiammatori e antitumorali, mentre gli altri due esprimenti fattori tollerogenici responsabili dell'immunotolleranza, 2 cluster di NK3 mixed $\gamma\delta$ T e un cluster più piccolo di NK4.

Dalla componente mieloide si sono identificati 10 cluster differenti comprendenti granulociti, tra i quali mastociti, basofili e neutrofilo, fagociti mononucleati comprendenti cellule dendritiche e macrofagi e un cluster di NK esprimenti sia geni linfoidi che mieloidi. (Fig. 1A)

La principale differenza emersa dal confronto dei risultati ottenuti nelle 2 condizioni è che nel tessuto sano vi è un'abbondanza di NK antitumorali, assenti nel tessuto tumorale che al contrario è caratterizzato dalla presenza di specifici sottogruppi mieloidi infiltranti il tumore; per quanto riguarda la quantità di neutrofilo invece restava pressoché invariata nelle due circostanze. (Fig. 1B)

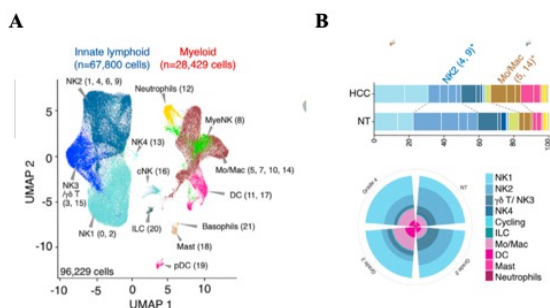


Figura 1: Caratterizzazione delle componenti del sistema immunitario innato nel carcinoma epatocellulare HCC. (A) Clusterizzazione Louvain di 96,229 trascrittomi scRNA-seq delle cellule immunitarie innate in tessuti tumorali e non tumorali (NT) da 10 pazienti con HCC (22 cluster identificati). (B) Cluster prevalenti nei tessuti HCC e NT. * $p < 0.05$ test multiparametrico Wilcoxon test.

3.2 Re-clustering di cellule mieloidi

Per una visuale più ampia si è proseguito con un re-clustering prima della componente mieloide, ricavando due cluster distinti, uno di neutrofilo e uno di fagociti mononucleati. Focalizzandosi su quest'ultimo e implementando un ulteriore re-clustering si sono distinti due differenti gruppi: cellule dendritiche e macrofagi. (Fig. 2) I monociti sono stati suddivisi in 3 sottogruppi sulla base dell'espressione di FCGR3A (Fc gamma receptor 3 A) in $CD14^+CD16^-$ monociti classici, $CD14^+CD16^+$ monociti intermedi e $CD14^-CD16^+$ monociti non classici.

Per i macrofagi sono stati identificati 7 cluster: uno infiammatorio, due di macrofagi associati al tumore FOL2-TREM2⁺ esprimenti SPP1⁺ i quali avevano un'ulteriore suddivisione sulla base dell'espressione di CD163 in CD163^{low} e CD163^{high}, e quattro FOL2⁺TREM2⁻ di cui 3 macrofagi residenti nel tessuto e uno comprendente cellule Kupffer, queste ultime sono un sottogruppo di macrofagi residenti nel tessuto che si trovano a livello del fegato e che hanno il ruolo di mantenere in condizioni fisiologiche l'organo.

Dal cluster di cellule dendritiche sono stati identificati 9 sottogruppi sulla base di marker fenotipici: 2 di cellule dendritiche plasmoidi, e 7 di cellule dendritiche convenzionali, suddivisibile in ulteriori 4 gruppi: DC1, AS-DC, DCregolatorie e DC2, queste ultime a loro volta suddivisibili in ulteriori 4 sottogruppi.

Dal confronto tra la condizione tumorale e non, si è notato che vi era una differenza significativa per quanto riguarda la presenza delle DC2, in particolare il sottogruppo esprime marcatori per IFN di tipo I e le DCregolatorie, che risultavano essere particolarmente arricchite nella sezione di tessuto tumorale.

Oltre a questi 3 sottogruppi ben caratterizzati, è stato identificato un ulteriore gruppo di cellule esprime geni affini sia a monociti FCN1, a neutrofili CSF3R TREM1 e CLEC4E e caratterizzati da marcatori associabili a cellule di derivazione mieloidi con funzione immunosoppressiva (identificato con c10).

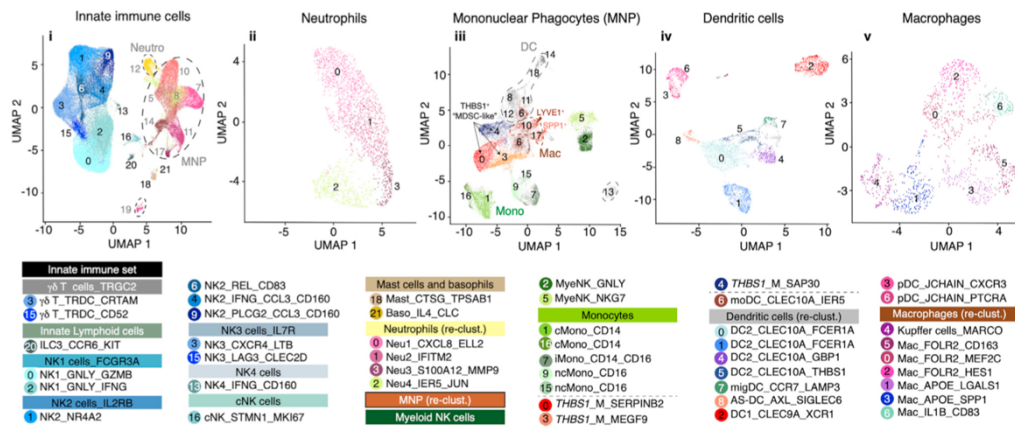


Figura 2: Caratterizzazione delle componenti del sistema immunitario innato nel carcinoma epatocellulare HCC. Louvain clusters rappresentati in diversi colori in base alle annotazioni dei tipi cellulari definiti tramite il dataset globale delle cellule immunitarie innate e successiva riclusterizzazione delle popolazioni cellulari indicate dai cerchi tratteggiati. Neutrofili (ii) e fagociti mononucleati (iii) sono stati riclusterizzati a partire dal set immunitario innato di partenza (i), mentre cellule dendritiche (iv) e macrofagi (v) sono stati riclusterizzati dal dataset relativo ai fagociti mononucleati (iii).

3.3 Riclassificazione della componente mieloide in HCC e identificazione di 3 sottogruppi di cellule THBS1⁺

Le cellule soppressorie di derivazione mieloide MDSC, comprende diverse popolazioni cellulari che si espandono in condizioni patologiche, tra le quali neoplasie, infiammazioni e infezioni. Data la loro capacità inibitoria nei confronti dell'attività antitumorale mediata dai linfociti T, rappresentano uno dei gruppi cellulari maggiormente coinvolti nella progressione del cancro. A sfavore vi è

anche il fatto che non si è identificato uno specifico marcatore cellulare, ma vengono ancora utilizzati marker che riconoscono anche altre tipologie cellulari, con l'incapacità di avere un pool di estrazione delle MDSC sufficientemente puro rendendone difficile la caratterizzazione. [10]

Da una prima classificazione del set di cellule immunitarie innate è stato individuato un cluster di fagociti mononucleati MNP, comprendente a sua volta diversi sottogruppi. Il 27,4 % della macrocategoria di MNP è rappresentata da un cluster di cellule (denominato c10 nel cluster delle cellule immunitarie innate) definite THBS1 e identificate sulla base dell'espressione di un set di 10 geni (THBS1, VCAN, SS100A12, SERPINB2, SAP30, MEGF9, TREM1, VEGFA, OLR1, PHLDA1) con la particolarità di risultare positive per le firme geniche identificative delle MDSCs e marcatori genetici tipici di monociti e neutrofili.

La ri-classificazione della popolazione di MNP, ha fornito dati più precisi, permettendo di focalizzarsi sul cluster c10, osservando come nonostante queste cellule avessero molti aspetti in comune, si poteva fare comunque un'ulteriore sotto classificazione sulla base di geni differenzialmente espressi.

La principale caratteristica condivisa dai 3 gruppi è l'espressione di CD36, gene che codifica per il recettore scavenger receptor CD36, glicoproteina di superficie che riconosce lipoproteine ossidate a bassa densità; in particolare riconosce fosfatidil serina che è presente sulla superficie di cellule apoptotiche, e questo recettore ha un ruolo nella trasduzione del segnale portando alla regolazione dello sviluppo cellulare, attivazione, crescita e mobilità, e in questo caso, come in molti altri è associata ad una progressione tumorale.

Sulla base dei geni differenzialmente espressi si sono descritti i 3 diversi cluster: un primo gruppo c0 di cellule THBS1 esprimenti geni affini a neutrofili, aventi una bassa espressione di CD163 e alta espressione di LOX-1, proteina codificata dal gene OLR1; un secondo gruppo c3 di cellule con geni affini a monociti ma con una bassa espressione sia di TREM1 che di CD163 e LOX-1, e un ultimo gruppo c4 presentante geni affini a macrofagi, cellule dendritiche e neutrofili, caratterizzati da un'alta espressione di CD13, TREM1 e CLEC4E, e un livello di espressione intermedio di LOX-1; queste ultime vengono anche denominate come CD36^{high}CD163⁺LOX-1^{med}TREM1^{high}CLEC4E⁺.

Sulla base di queste caratteristiche si assegnano le seguenti nomenclature: CD163⁻LOX1⁺ per quanto riguarda il gruppo c0; CD163⁻LOX1⁻ per quanto riguarda il gruppo c3, e CD163⁺LOX1^{med} per il gruppo c4. (Fig. 3)

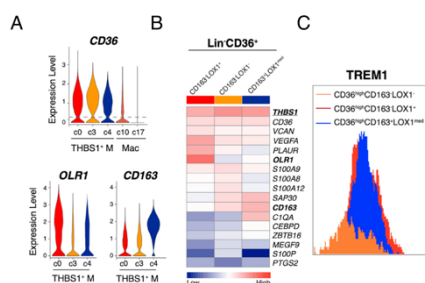


Figura 3: caratterizzazione dell'espressione genica dei 3 gruppi di cellule THBS1⁺. (A) Grafici a violino che rappresentano l'espressione di CD36, OLR1 e CD163 nei cluster MNP indicati. (B) Livello di espressione dei geni selezionati nei diversi sottogruppi mieloidi isolati tramite FACS e normalizzati utilizzando la media geometrica dell'espressione genica delle cellule immunitarie innate isolate da sei pazienti con HCC. (C) Istogramma raffigurante l'espressione di TREM1 nei 3 diversi gruppi di cellule THBS1⁺ esprimenti tutti alti livelli di CD36 e classificati sulla base della differente espressione di LOX-1, CD163.

Per identificare la possibile origine delle cellule c4 è stata implementata la tecnica del RNA-velocity sul set di dati del sistema immunitario innato (Fig. 4A) e poi sul sottogruppo di MNP (Fig. 4B), osservando una loro possibile origine a partire da cellule dendritiche derivanti da monociti (moDC). Per capire al meglio la regolazione di queste viene sfruttata la tecnica dello pseudotime ordering, identificando 3 stati trascrizionali differenti, e ponendo le c4, migDC e moDC in uno stato trascrizionale intermedio tra monociti, macrofagi e cellule dendritiche (Fig. 4C). Tramite una stima del potere di differenziazione si è visto che queste specifiche cellule hanno una maggior capacità di differenziamento in linee cellulari differenti rispetto alle altre due e ai macrofagi.

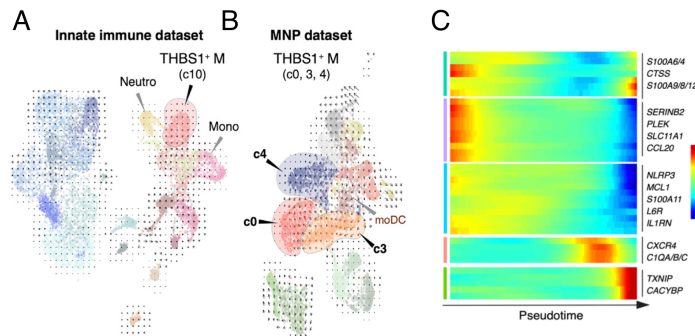


Figura 4: Caratterizzazione del gruppo cellulare THBS1⁺ per definirne l'origine e lo stato trascrizionale. (A) Evidenza del cluster THBS1⁺M tramite RNA-velocity implementato sul gruppo di cellule immunitarie innate. (B) Evidenza dei 3 diversi tipi cellule THBS1⁺M e moDC tramite RNA-velocity implementato sul gruppo di MNP. (C) Rappresentazione tramite la tecnica Pseudotime ordering del differente livello di espressione di geni nell'arco temporale definito Pseudotime.

3.4 Identificazione del sottogruppo cellulare THBS1⁺ M_{reg} come un principale responsabile dell'immunosoppressione

Per avere una conferma della capacità immunosoppressiva di questo gruppo mieloide e vedere eventuali differenze tra i diversi subset precedentemente identificati, gli studiosi hanno allestito una co-coltura tra cellule THBS1⁺ con linfociti T CD4 derivati da pazienti sani e CD8 attivati. Nonostante l'evidente effetto inibitorio che mostravano tutti e tre i sottogruppi di cellule THBS1⁺, l'azione più marcata la si aveva con il sottogruppo delle CD163⁺LOX1^{med} (Fig. 5A).

Come controllo si sono usate le HuMOSCs, confermando il ruolo immunosoppressorio inibendo la produzione di citochine da parte dei linfociti T, e siccome queste, come le CD163⁺LOX1^{med}, mostravano un'elevata espressione di TREM1 e CD163, si è giunti all'ipotesi che fosse proprio la co-espressione di questi ad attribuire una funzione immunosoppressiva alle cellule. Inoltre, sia il campione in esame che il controllo mieloide esibivano un alto livello di espressione di TGF1B.

Le THBS1⁺ CD163⁺LOX1^{med} rispetto agli altri due sottogruppi THBS1⁺ e in aggiunta rispetto al controllo mieloide presentavano altre caratteristiche: elevati livelli di espressione di IL13RA1, gene codificante catena del recettore di IL-13, citochina che stimola e induce la produzione di TGF-β, PTGES2 e PTGER2 che sono la prostaglandina E2 sintetasi e il suo recettore, ODC1 gene codificante un

enzima che limita la velocità di biosintesi della poliammina, ATF4 che codifica per fattore di trascrizione 4 necessario per l'immunosoppressione. (Fig. 5B)
 Grazie alle loro caratteristiche l'ambiente immunosoppressivo è generato mediante la produzione di ROS, ossido nitrico, arginasi, prostaglandina, citochine infiammatorie (TGF- β e IL-10) e checkpoint immunitari (PD-L1).

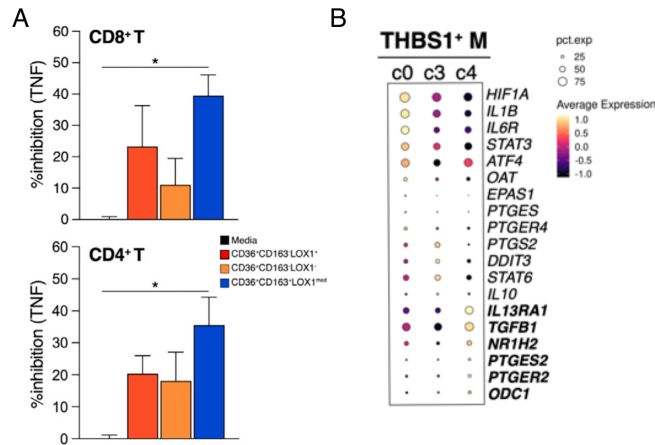


Figura 5: Evidenza delle differenze tra i 3 subset cellulari THBS1⁺. (A) Quantificazione della % di inibizione di produzione di TNF da parte dei linfociti T CD8 e CD4 tramite Box-plot con un maggior potere inibitorio derivato dal cluster c4 rispetto a c0 e c3. (B) Illustrazione mediante il diagramma a punti dell'espressione media dei geni associati alle funzioni immunosoppressive e pro fibrotiche nei 3 cluster di THBS1⁺.

3.5 Correlazione spaziale tra le cellule THBS1⁺ reg e lesioni fibrotiche

Per comprendere la correlazione eziologica e TIME si sono definiti 5 subset cellulari notando che nei pazienti affetti da HCC relazione a SLD presentavano una maggior porzione di neutrofili e cellule immunosoppressive. Per convalidare quest prima osservazione si è quantificata in particolare la quantità di cellule c4 trattando il campione con anticorpi anti-CD163 e anti-CLEC4E, che riconoscono marker di superficie, evidenziando che vi era una differenza sostanziale tra le differenti eziologie.

Inoltre, si sono identificati dei geni specifici in grado di discriminare le THBS1⁺ rispetto altre popolazioni mieloidi, ma coincidenti con quelli caratteristici dei fibroblasti, ad indicare che le cellule THBS1⁺ potrebbero essere state generate con un profilo pro-fibrotico.

Per verificarne la localizzazione cellulare si è implementata la trascrittomiche spaziale analizzando la sezione di tessuto di due pazienti affetti da HCC, (Fig. 6) osservando una costante presenza di queste a livello di regioni fibrotiche. Da

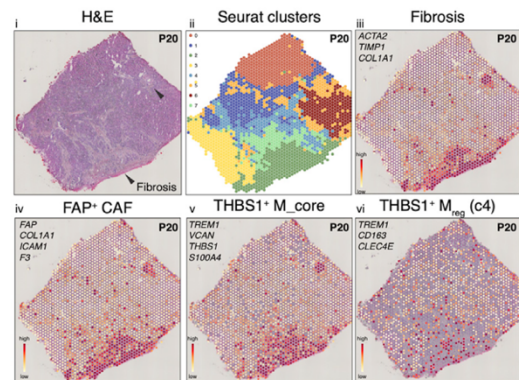


Figura 6: Sezione di tumore da un paziente affetto da HCC analizzata mediante st-RNA-seq. (i) sezione istologica colorata con H&E (ii) sovrapposizione spaziale dei cluster rilevati mediante il metodo "clustering Louvian Seurat" (iii) localizzazione delle regioni fibrotiche (iv) localizzazione di FAP⁺CAF (v) localizzazione delle cellule THBS1⁺ (vi) localizzazione del cluster c4.

un'ulteriore analisi si sono evidenziati anche CAFs con funzione immunosoppressoria identificati sulla base dell'espressione di FAP; con una localizzazione spaziale sovrapponibile a quella delle THBS1⁺ M_{reg}. Questa co-presenza non era casuale ma rilevata principalmente a livello delle regioni fibrotiche, suggerendo un possibile cross talk tra le due componenti e con l'ambiente tumorale. (Fig. 7)

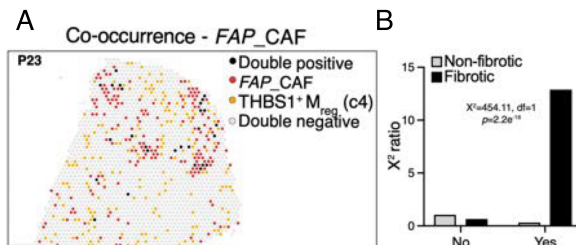


Figura 7: Co-localizzazione spaziale di FAP-CAF. (A) Distribuzione dei diversi tipi cellulari identificati sulla base dell'espressione di FAP, CAF e THBS1⁺. (B) Evidenza della significativa differenza che si ha del tipo cellulare presente tra regioni fibrotiche e non fibrotiche

3.6 Le cellule THBS1⁺ M_{reg} sono correlate a esiti clinici negativi e sono particolarmente abbondanti in patologie di HCC associato a SLD

Lo studio riguardante le popolazioni mieloidi è stato ampliato, usufruendo dell'algoritmo CIBERSORTx per dedurre l'abbondanza dei diversi sottogruppi cellulari intratumorali, addestrato su dati derivati da single-cell ottenuti dall'analisi di tessuto tumorale e non tumorale da due coorti di pazienti.

Si è avuta un'ulteriore conferma della componente immunitaria nelle due condizioni: i macrofagi esprimenti SPP1 e le MEGF9^{high} erano distribuiti in maniera variabile tra le due coorti di pazienti, mentre si aveva una costante deplezione dei macrofagi LYVE1⁺ e OLR1^{high} nella condizione tumorale. I dati hanno mostrato inoltre come in questa condizione le sottopopolazioni di THBS1⁺M_{reg}, iMono e moDC erano molto più abbondanti e correlate ad uno stadio tumorale avanzato (3 o 4), alti livelli del marker di mortalità AFP, sottoclasse Hoshida S2 e silenziamento della via di segnalazione HIPPO. (Fig. 8A) Si è implementato un cluster gerarchico su una delle due coorti appena analizzate basato sui dati forniti da CIBERSORTx, fornendo una correlazione tra gruppi cellulari mieloidi infiltranti il tumore e l'esito clinico atteso, permettendo di suddividere gli individui della coorte presa in esame in 3 diversi gruppi. (Fig. 8B)

Gruppo A: pazienti con una probabilità media di sopravvivenza alta e un'elevata porzione di macrofagi esprimenti LYVE1⁺.

Gruppo B: pazienti con una probabilità di sopravvivenza media minore rispetto ai precedenti e caratterizzati da una maggior porzione di macrofagi SPP1⁺.

Gruppo C: pazienti con una sopravvivenza media decisamente ridotta, mostravano un'elevata porzione di THBS1⁺ M_{reg}, iMono e moDC.

Per avere una visione ancora più chiara si è esteso lo studio sull'arricchimento di cellule THBS1⁺ M_{reg} in pazienti con HCC correlato a SLD su due coorti di pazienti diverse, dimostrando che vi era una porzione del sottogruppo cellulare THBS1⁺M_{reg} maggiore nei pazienti che mostravano alla base della patologia una condizione di

steatosi epatica, confermando ulteriormente l'esistenza di una correlazione tra eziologia patologica e componente immunitaria. (Fig. 8C)

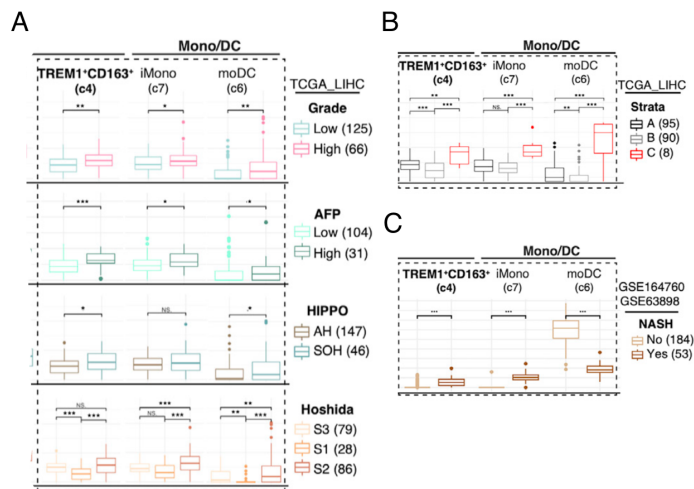


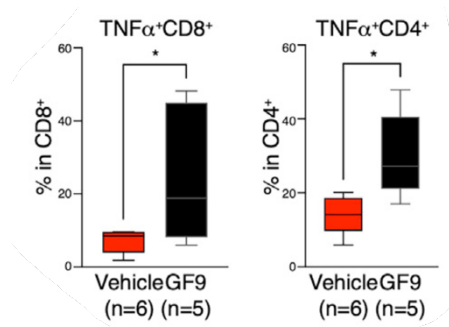
Figura 8: Rappresentazione mediante box plot dei diversi punteggi previsti mediante CIBERSORTx delle cellule TREM1⁺CD163⁺, iMono e moDC. (A) Rappresentazione dei punteggi in correlazione al grado tumorale, livello di AFP, attivazione o inattivazione della via di segnalazione di HIPPO, classe Hoshida. (B) Rappresentazione dei punteggi e stratificazione dei pazienti in 3 gruppi sulla base della sopravvivenza media. (C) Rappresentazione dei punteggi in correlazione a presenza o assenza della patologia NASH.

3.7 Ruolo del recettore TREM1 ed effetti di una sua inibizione

Nonostante i risultati fossero evidenti sul fatto che la popolazione di macrofagi THBS1⁺ M_{reg} fosse quella maggiormente presente a livello tumorale, e che tra tutti i geni che le identificavano, TREM1 fosse quello maggiormente correlato ad un elevato rischio sulla sopravvivenza; si è comunque voluti andare più nello specifico per confermare o smentire il fatto che era proprio la presenza di questo recettore a conferire loro una capacità immunosoppressoria.

La sua espressione è particolarmente elevata nei pazienti caratterizzati da una probabilità di sopravvivenza media scarsa ed è correlato a fibrosi, silenziamento della via HIPPO e classe Hoshida S2; inoltre è associata a quella di TGF-β, IL-10, PTGES2 e IL-8 e alla presenza di effettori dell'immunosoppressione e una minor porzione di cellule T CD8.

Per verificare l'impatto che tale recettore ha nel contesto tumorale si sono presi in esame modelli murini in presenza di steatosi epatica indotta tramite dieta, e in condizioni normali, inibendolo mediante il peptide GF9 che ha la capacità di interferire nel legame intracellulare di TREM1 con DAP12. Si riscontra una rapida eradicazione tumorale e un aumento del rapporto tra la quantità di cellule CD8 e CD4 FoxP3⁺T nel microambiente tumorale, ad indicare che la quantità di cellule citotossiche è maggiore rispetto alle cellule regolatorie, con un aumento degli effetti citotossici mediati dai linfociti T CD8. L'effetto di questa inibizione di TREM1



mediata da GF9 genera un effetto che è paragonabile a quello che si osservava tramite trattamenti anti-Gr1 che eliminava le cellule intratumorali Ly6G⁺Ly6C⁻ esprimenti TREM1, consolidando ulteriormente l'ipotesi secondo la quale fosse proprio TREM1 il responsabile di questo effetto. (Fig. 9)

Figura 9: effetto dell'inibizione di TREM1 sulla produzione di TNFα. Confronto della produzione di TNFα da parte dei linfociti CD8 e CD4 in situazione normale e nel caso di TREM1 inibito. Le barre di errore rappresentano SEM. $p^* < 0,05$ utilizzando test-T per dati non appaiati.

Per un'ulteriore conferma è stata fatta una contro prova in cui si stimolava l'espressione di TREM1 su un gruppo di cellule HuMoSCs in co-cultura con cellule T, osservando come anche in questo caso si aveva un'inibizione dell'attività dei linfociti T. Questa seconda condizione la si è ottenuta andando a trattare il gruppo di HuMoSC con il ligando di TREM1 che è il PGLYRP1 complessato con un peptiloglucano, generando il complesso PP che portava ad un'ulteriore incremento sia dell'espressione di TREM1 sulla superficie cellulare che un suo rilascio in forma solubile (Fig. 10A), inducendo inoltre l'espressione di LOX-1 e CD15. (Fig. 10B)

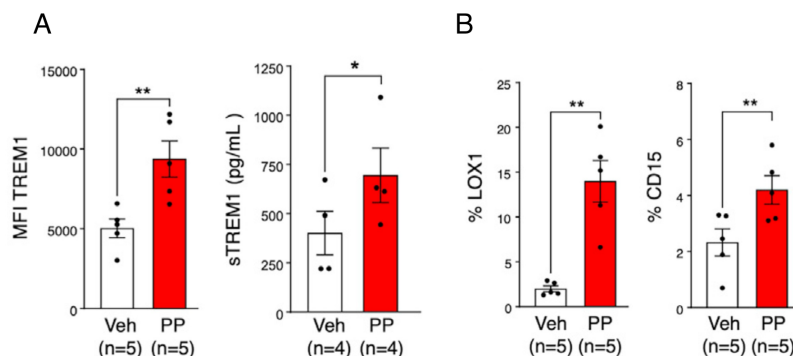


Figura 10: Confronto tra campioni di controllo e campioni trattati con PP. (A) Evidenza mediante box plot dell'aumento della concentrazioni di TREM1 sulla superficie (pannello a sinistra) e di TREM1 solubile (pannello a destra) in campioni trattati con PP rispetto ai campioni di controllo. (B) Evidenza mediante box plot dell'aumento della concentrazioni di LOX1 (pannello a sinistra) e di CD15 solubile (pannello a destra) in campioni tratti con PP rispetto ai campioni di controllo.

Il complesso di peptiloglucano PGN e PGLYRP1 (PP) e TREM1 si influenzano a vicenda: si ha PP che stimola TREM1 ad inibire la proliferazione e la funzione dei linfociti T CD8, andando ad ostacolare la produzione di TNFα da parte di questi ultimi, e mediata anche da IL-10; la cui sintesi però è controllata e incrementata da PP ma con funzione TREM1 dipendente, osservando come in esperimenti di KO del gene codificante per TREM1, la produzione di questa citochina era ridotta. Risulta particolarmente interessante vedere come TREM1 in un fegato sano abbia un'espressione fisiologica relativamente bassa, mentre in un contesto di fibrosi epatica questa è particolarmente aumentata portando ad un rilascio di fattori

infiammatori che contribuiscono ulteriormente all'aggravare della situazione, inducendo la proliferazione dei macrofagi in un profilo di tipo M1. Parallelamente sembrerebbe che TREM1 contribuisca ad un'inibizione dell'attività delle cellule T andando a favorire la produzione di una citochina antinfiammatoria IL-10.

Questi ultimi risultati hanno dato un'ulteriore conferma del fatto che l'ambiente cellulare presente in pazienti con steatosi epatica promuove l'espansione delle THBS1⁺ M_{reg}.

Tutti questi studi confermano il fatto che risulta necessario avanzare una terapia mirata che abbia come target il recettore TREM1.

4. DISCUSSIONI E LIMITI DELLO STUDIO

Questo studio ha rivelato la presenza di cellule mieloidi in un contesto HCC non precedentemente identificate, e le analisi condotte hanno portato a stipulare 4 risultati: 1) la presenza di epatocarcinoma cellulare è correlata alla presenza di stati misti inter-mieloidi, ovvero differenti gruppi di cellule mieloidi che co-esistono, ipotizzando che questi possano derivare sia da ematopoiesi di emergenza che da risposte immunitarie propense a sostenere la crescita tumorale 2) la capacità di assumere l'aspetto di "cellule infiltranti il tumore" non è casuale ma è relativa sia alla tipologia cellulare che allo stato di differenziamento in cui esse si trovano 3) la popolazione di cellule THBS1⁺ M_{reg} si trova principalmente a livello di regioni fibrotiche, hanno un'attività immunosoppressoria e sono correlate ad esiti clinici negativi 4) il duplice ruolo di TREM1 nel sostenere la crescita tumorale in vitro, e nell'accrescere l'azione immunosoppressiva delle cellule immunosoppressive mieloidi di derivazione umana.

Ci si è focalizzati specialmente su due aspetti fondamentali quali le nuove cellule mieloidi rilevate, esprimenti marker fenotipici associabili alla popolazione di cellule immunosoppressive di derivazione mieloide e il recettore TREM1.

Per quanto riguarda il subset cellulare THBS1 M_{reg} questo ha portato all'identificazione di un sottogruppo particolare con caratteristiche fenotipiche assimilabili a macrofagi/Dc e granulociti, dove l'attività immunosoppressiva era particolarmente marcata a confronto degli altri due gruppi cellulari appartenenti alla stessa tipologia, e che era associato a fibroblasti pro-fibrotici e tumorigenici con la particolarità di espandersi a livello tumorale in un contesto di SLD.

Il secondo aspetto fondamentale riguarda il recettore TREM1, che permette anche di discriminare le cellule THBS1⁺ dalle altre cellule fagocitiche mononucleate presenti a livello del fegato; inizialmente ad esso erano state attribuite proprietà pro-infiammatorie mediate da citochine pro-infiammatorie sintetizzate dalle cellule Kupffer le quali porterebbero a sostenere la crescita tumorale, ma questi studi erano stati fatti mediante colorazioni non sufficientemente adeguate per identificare il subset cellulare preciso. Studi successivi, mediante scRNAseq, hanno portato ad avere una correlazione valida tra la presenza di TREM1 e un risultato clinico negativo, immunosoppressione, fibrosi epatica e regioni fibrotiche.

Studi più recenti hanno portato ad identificare sTREM1 come una molecola avente un effetto nocivo a livello del fegato portando le cellule che lo esprimono ad assumere un profilo immunosoppressorio aumentando la loro capacità di sopprimere l'attività funzionale delle cellule T, ipotizzando inoltre che questa possa portare all'attivazione delle cellule epatiche stellate e generare fibrosi epatica. [11]

Si è arrivati alla conclusione che è opportuno suddividere i pazienti in base all'eziologia che vi è alla base della patologia per poter progettare terapie mirate alla situazione. Nel caso di HCC relazionato a SLD un buon target potrebbe essere la proteina TREM1.

Il principale limite di questo studio è il fatto di aver raccolto dati su piccole coorti di pazienti; sarebbe opportuno estendere la ricerca a coorti di pazienti più grandi implementando la tecnica dell'immunofluorescenza multiplex, per poter avere una panoramica più chiara anche riguardo alla relazione che vi è tra la presenza di questa

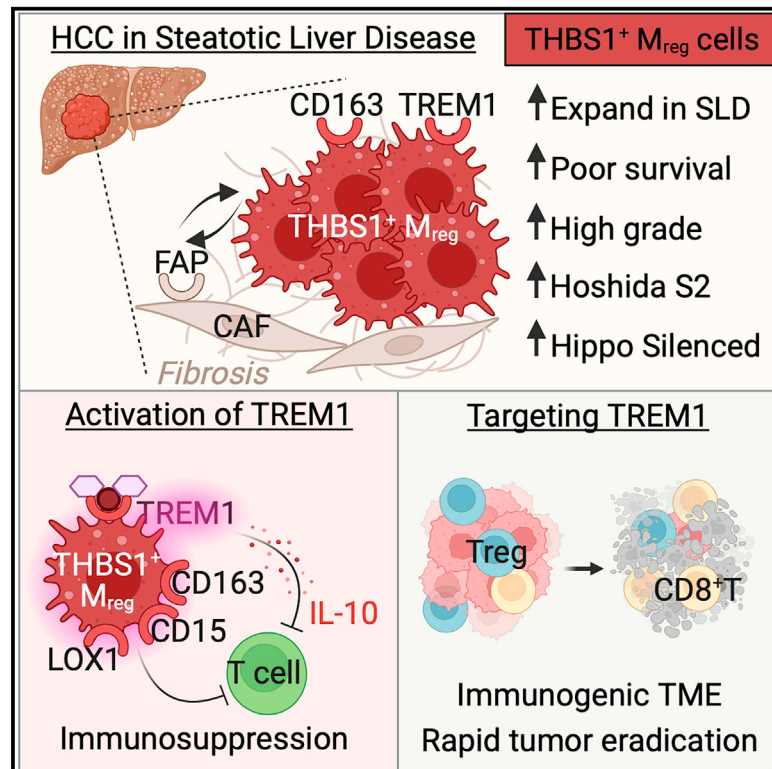
popolazione cellulare con altre cellule nell'ambiente tumorale e quali siano i fattori scatenanti relazionati a SLD che inducano la differenziazione di questo subset cellulare.

BIBLIOGRAFIA

1. Asafo-Agyei KO, Samant H. *Hepatocellular Carcinoma*. StatPearls 2024 Jan
2. Llovet, J.M., Kelley, R.K., Villanueva, A. et al. *Hepatocellular carcinoma*. Nat Rev Dis Primers 7, 6 (2021)
3. Stauffer K, Stauber RE. *Steatotic Liver Disease: Metabolic Dysfunction, Alcohol, or Both?* Biomedicines. 2023; 11(8):2108.
4. Nicole M. Anderson and M. Celeste Simon. *Tumor Microenvironment*. Current Biology. 2020 Aug 17 30(16): R921-925
5. Ying F, Chan MSM, Lee TKW. *Cancer-Associated Fibroblasts in Hepatocellular Carcinoma and Cholangiocarcinoma*. Cell Mol Gastroenterol Hepatol. 2023;15(4):985-999.
6. Gryziak M, Wozniak K, Kraj L, Rog L, Stec R. *The immune landscape of hepatocellular carcinoma-where we are?* Oncol Lett. 2022 Sep 27; 24(5):410.
7. Colonna, M. *The biology of TREM receptors*. Nature Reviews Immunology. 23, 2023 Feb: 580–594.
8. Ashwin Ajith, Kenza Mamouni, Daniel D. Horuzsko, Abu Musa, Amiran K. Dzutsev, Jennifer R. Fang, Ahmed Chadli, Xingguo Zhu, Iryna Lebedyeva, Giorgio Trinchieri, and Anatolij Horuzsko. *Targeting TREM1 augments antitumor T cell immunity by inhibiting myeloid-derived suppressor cells and restraining anti-PD-1 resistance*. The journal of Clinical Investigation 2023 Nov 1: 133
9. Rai V, Agrawal DK. *Regulation of TREM1-Mediated Inflammation in Hepatocellular Carcinoma Cells*. Reports. 2021; 4(2):17.
10. Veglia, F., Sanseviero, E., and Gabrilovich, D.I. (2021). *Myeloid-derived suppressor cells in the era of increasing myeloid cell diversity*. Nature Reviews Immunology. 2021 Feb, 485–498.
11. Huifang Sun, Jianguo Feng, Liling Tang. *Function of TREM1 and TREM2 in Liver-Related Diseases*. Cells 2020, 9, 2626.

THBS1⁺ myeloid cells expand in SLD hepatocellular carcinoma and contribute to immunosuppression and unfavorable prognosis through TREM1

Graphical abstract



Authors

Julie Giraud, Domitille Chalopin, Eloïse Ramel, ..., Marc Derive, Macha Nikolski, Maya Saleh

Correspondence

maya.saleh@inrs.ca

In brief

Giraud et al. characterize the innate immune landscape of HCC. They identify an immunosuppressive THBS1⁺ myeloid population co-expressing TREM1 and CD163 that expands in the steatotic liver disease etiology of HCC and contributes to unfavorable prognosis through TREM1. TREM1 blockade elicits an immunogenic TME and rapid tumor eradication.

Highlights

- Atlas of hepatic innate immune cells from patients with HCC
- THBS1⁺ M_{reg} cells expand in SLD-associated HCC and populate fibrotic lesions
- TREM1 engagement potentiates immunosuppression and HCC growth *in vivo*
- THBS1⁺ M_{reg} density and TREM1 expression associate with HCC poor prognosis



Article

THBS1⁺ myeloid cells expand in SLD hepatocellular carcinoma and contribute to immunosuppression and unfavorable prognosis through TREM1

Julie Giraud,^{1,10} Domitille Chalopin,^{1,8,10} Eloïse Ramel,¹ Thomas Boyer,¹ Atika Zouine,² Marie-Alix Derieppe,³ Nicolas Larmonier,¹ Olivier Adotevi,⁴ Brigitte Le Bail,⁵ Jean-Frédéric Blanc,⁶ Christophe Laurent,⁶ Laurence Chiche,⁶ Marc Derive,⁷ Macha Nikolski,⁸ and Maya Saleh^{1,9,11,*}

¹University of Bordeaux, CNRS, ImmunoConcEpT, UMR 5164, 33000 Bordeaux, France

²Bordeaux University, CNRS UMS3427, INSERM US05, Flow Cytometry Facility, TransBioMed Core, 33000 Bordeaux, France

³University of Bordeaux Animal Facilities, 33600 Pessac, France

⁴Université Bourgogne Franche-Comté, INSERM, UMR1098, 25000 Besançon, France

⁵Bordeaux University Hospital, Division of Pathology, Pellegrin Hospital, 33000 Bordeaux, France

⁶University of Bordeaux Hospital, Division of Gastrohepatology and Oncology, Haut Leveque Hospital, 33604 Pessac, France

⁷Inotrem SA, Nancy, France

⁸University of Bordeaux, CNRS, IBGC, UMR 5095, 33000 Bordeaux, France

⁹Institut National de la Recherche Scientifique (INRS), Armand Frappier Health & Biotechnology (AFSB) Research Center, Laval, QC H7V 1B7, Canada

¹⁰These authors contributed equally

¹¹Lead contact

*Correspondence: maya.saleh@inrs.ca

<https://doi.org/10.1016/j.celrep.2024.113773>

SUMMARY

Hepatocellular carcinoma (HCC) is an inflammation-associated cancer arising from viral or non-viral etiologies including steatotic liver diseases (SLDs). Expansion of immunosuppressive myeloid cells is a hallmark of inflammation and cancer, but their heterogeneity in HCC is not fully resolved and might underlie immunotherapy resistance. Here, we present a high-resolution atlas of innate immune cells from patients with HCC that unravels an SLD-associated contexture characterized by influx of inflammatory and immunosuppressive myeloid cells, including a discrete population of THBS1⁺ regulatory myeloid (M_{reg}) cells expressing monocyte- and neutrophil-affiliated genes. THBS1⁺ M_{reg} cells expand in SLD-associated HCC, populate fibrotic lesions, and are associated with poor prognosis. THBS1⁺ M_{reg} cells are CD163⁺ but distinguished from macrophages by high expression of triggering receptor expressed on myeloid cells 1 (TREM1), which contributes to their immunosuppressive activity and promotes HCC tumor growth *in vivo*. Our data support myeloid subset-targeted immunotherapies to treat HCC.

INTRODUCTION

Hepatocellular carcinoma (HCC) ranks among the most common malignancies worldwide, with a rising incidence in the Western world. Despite well-known risk factors, i.e., chronic viral infection with hepatitis B virus, primarily in Asia, and hepatitis C virus in Western countries, and steatotic liver diseases (SLDs)¹ including alcohol consumption-associated steatohepatitis and metabolic dysfunction-associated steatohepatitis (previously referred to as non-alcoholic steatohepatitis [NASH]), HCC is diagnosed late in most patients.² While several systemic treatments have been approved for advanced HCC, e.g., tyrosine kinase inhibitors, they provide small clinical benefit.³ The landscape of clinical trials for HCC has shifted to immunotherapy, with the approval of immune checkpoint inhibitors (ICIs), in first-line treatment (atezolizumab/bevacizumab and durvalumab/tremelimumab).^{3,4} However, ~75% of patients do not respond to these

treatments for unclear reasons.⁵ A previous meta-analysis of three randomized phase 3 clinical trials administering ICI to patients with advanced HCC showed a superior efficacy of immunotherapies in virally infected patients compared to NASH-affected patients with HCC,⁶ pointing to the tumor microenvironment (TME) as an important determinant of therapeutic success and highlighting the urgent need to identify theranostic immune biomarkers for patient stratification and to develop additional immunotherapies.

Myeloid cells are a main immune infiltrate in several solid tumors and are considered an impediment to all cancer therapeutic modalities, particularly immunotherapy. Modulating their recruitment, differentiation, or functions is being actively pursued as a therapeutic option.⁷ However, their indiscriminate depletion has failed to improve cancer patient overall survival, indicating that a better characterization of myeloid subsets is required for a targeted approach. Myeloid cells encompass



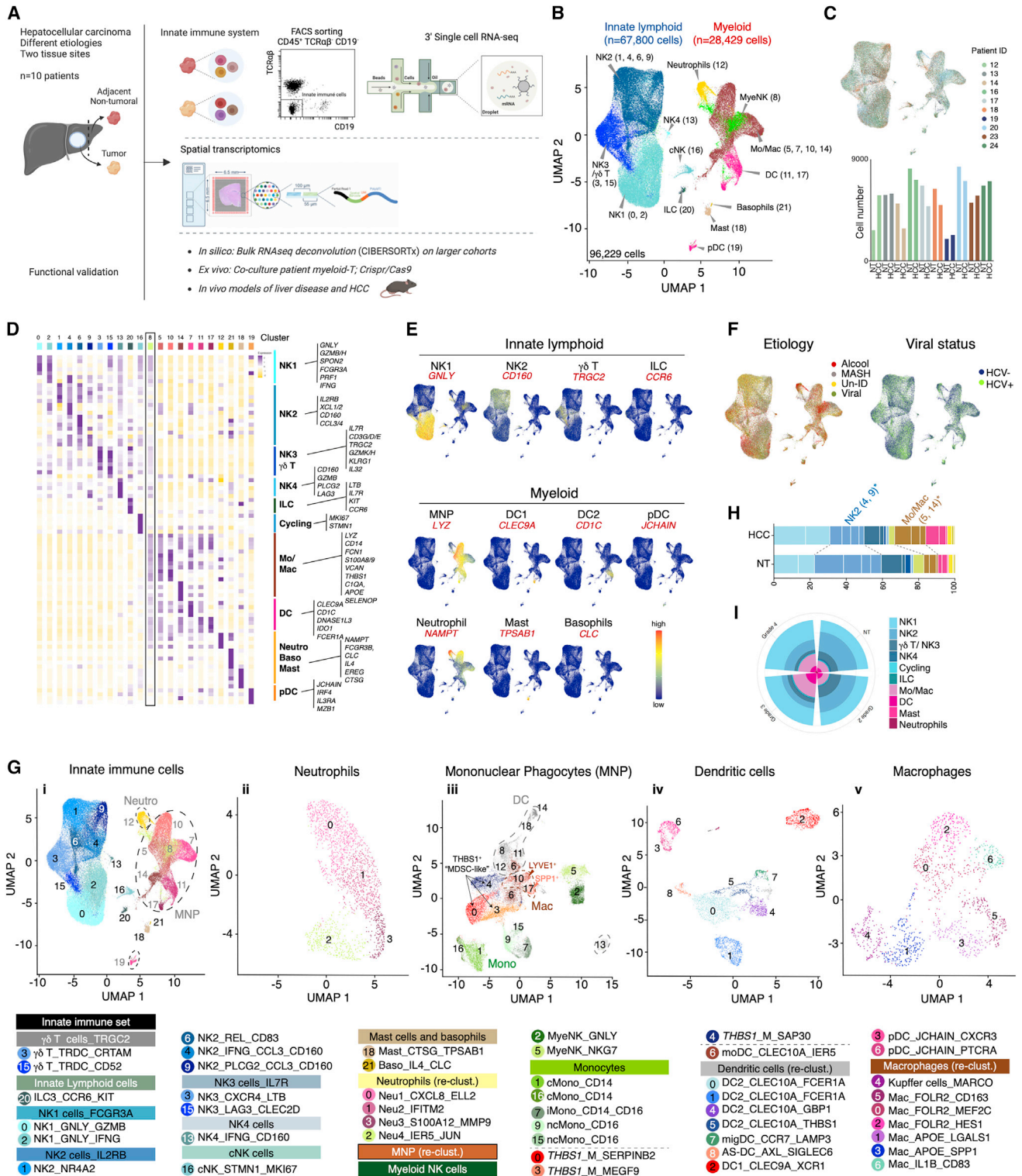


Figure 1. The innate immune landscape of hepatocellular carcinoma (HCC)

(A) Characterization of the hepatic innate immune cell landscape using scRNA-seq and stRNA-seq of tumors and adjacent NT tissue of 10 patients with hepatocellular carcinoma (HCC) of different etiologies.

(B) Louvain clustering of 96,229 scRNA-seq transcriptomes of innate immune cells in tumoral and NT tissues from 10 patients with HCC identifies 22 clusters.

(C) UMAP visualization and bar graph depicting cell numbers colored according to patient identity (ID).

(legend continued on next page)

mononuclear phagocytes (MNPs) and granulocytes, which exhibit remarkable heterogeneity according to ontogeny, inflammatory and metabolic signals, and tissue environments. The advent of single-cell and tracing technologies has unraveled the complexity of myeloid cell states, warranting context-specific characterization of deleterious subsets to direct targeted therapies.

While the cellular landscape of HCC has been previously described using single-cell approaches,^{8–14} the impact of etiology on the diversity of the innate immune compartment, particularly myeloid cells, has not been fully characterized. Here, we implemented scRNA-seq on purified innate immune cells freshly isolated from tumoral and juxta-tumoral tissues from patients with HCC of different etiologies and performed spatial transcriptomics (stRNA-seq) to map their localization. We unravel a discrete thrombospondin (THBS)1⁺ myeloid cell population, abundant in the tumor of patients with SLD-associated HCC that expresses monocyte- and neutrophil-affiliated genes and can be identified by co-expression of TREM1 and CD163. We refer to these cells as THBS1⁺ regulatory myeloid (M_{reg}) cells, as they are potent suppressors of T cell activity *ex vivo*, a function further potentiated by TREM1 engagement, are spatially enriched at HCC fibrotic lesions, and co-occur with FAP⁺ cancer-associated fibroblasts (CAFs) as revealed by stRNA-seq. Both THBS1⁺ M_{reg} intra-tumoral density and *TREM1* median expression associate with high-grade HCC and poor prognosis. In experimental mouse models, specific inhibition of TREM1 signaling results in an immunogenic TME and rapid HCC tumor eradication. Our results elucidate THBS1⁺ M_{reg} cells as a biomarker of severe HCC and a potential immunotherapeutic target.

RESULTS

The hepatic innate immune landscape in HCC

To characterize the innate immune landscape of HCC at high resolution, we implemented scRNA-seq (10x Genomics) on fluorescence-activated cell sorting (FACS)-enriched CD45⁺ panTCR $\alpha\beta$ ⁻ CD19⁻ cells freshly isolated from tumors (HCC) and adjacent non-tumoral (NT) liver sections. In parallel, we applied stRNA-seq (Visium, 10x Genomics) on frozen tissue sections from the same patients (Figure 1A). We included 10 HCC patients with different etiologies (HCV [n = 3], obesity [n = 5], excessive alcohol consumption [n = 3]) (Table S1). Steatohepatitis and fibrotic lesions were confirmed in liver NT and HCC sections by hematoxylin/eosin/saffron and trichrome staining (Figure S1A). For scRNA-seq, 15,000 innate immune viable cells were loaded on the 10x chip. Following putative doublet removal and exclusion of stressed or dead cells (Figure S1B; Table S2),

we analyzed the transcriptomes of ~96,000 cells (~2,300 genes/cell) across 10 HCC (~46,000 cells) and 10 NT (~50,000 cells) samples. Following data processing, 22 Louvain clusters were identified (Figure 1B), containing cells from all patients and tissue sites (Figure 1C; Table S2). Using a scoring method based on signatures from Panglao DB, the expression of discriminatory features, and canonical markers (Figures 1D and 1E; Table S3), we identified the major innate immune cell populations (Figure 1B). At this initial resolution, we observed a lack of any specific population according to etiology or viral status (Figure 1F), consistent with previous studies.^{9,10}

In total, we identified 11 innate lymphoid clusters (~68,000 cells), encompassing one innate lymphoid cell (ILC3) cluster (c20) and 10 clusters of natural killer (NK) cells (Figure 1G). These included one cycling NK cluster (c16; *STMN1*; *MKI67*), two NK1 clusters (c0, 2) representing *FCGR3A* (CD16)⁺ cytotoxic NK cells (*FGFBP2*, *GNLY*, *CX3CR1*, *GZMB*, *PRF1*), and four liver-resident NK2 clusters (c1, 4, 6, 9) commonly expressing *IL2RB* and *CXCR6* but distinguished based on expression of inflammatory/anti-tumoral effectors (c4, 9; *IFNG*, *CCL3*, *CCL4L1*) versus tolerogenic factors (c1, 6; *NR4A2*).^{15–18} Two mixed NK3/ $\gamma\delta$ T clusters (c3, 15) and a smaller NK4 cluster (c13) were also unraveled (Figure 1G; Table S3).

For myeloid populations, our analysis revealed 10 clusters (~28,000 cells) including granulocytes, MNPs, and one cluster of NK cells (c8) expressing both lymphoid (*IL7R*, *GNLY*, *KLRF1*, *KLRD1*, *GZMH/K/B*, *IFNG*) and myeloid (*LYZ*, *HLA-DRA/B1*, *S100A8/9*, *SAT1*, *CST3*) genes (Figures 1D [box] and 1G; Table S3). Among the granulocytes, we identified mast cells (c18), a residual cluster of basophils (c21), and one subset of neutrophils, which formed a continuum of four states (Figure 1G). Neu1–3 expressed chemokines, matrix remodeling, and immunosuppressive factors (*CXCL8*, *CXCR4*, *MMP9*, *PTGS2*, *S100A12*, *PADI4*),¹⁹ while Neu4 encompassed neutrophil-like monocytes (*IER5*, *JUN*).²⁰ While the frequency of neutrophils was not significantly different in HCC compared to NT in our dataset, specific myeloid subsets significantly infiltrated the tumor, whereas anti-tumoral NK2s (c4, 9) were excluded from the tumor core (Figures 1H and 1I; Table S2).

Identification of THBS1⁺ myeloid cells distinct from monocytes, macrophages, and dendritic cells

To reliably identify and discriminate different MNP and granulocyte populations, we next established core signatures and validated their specificity by testing their performance in both the innate immune and MNP datasets. Macrophages, conventional dendritic cells (cDCs), and plasmacytoid DCs (pDCs) were well identified with our core signatures (Figures S1C and S1D), and their states were characterized by independent re-clustering

(D) Heatmap representing average expression of discriminating genes for each cluster.

(E) Feature plots representing the expression of innate immune cells canonical markers.

(F) UMAP visualization colored according to patient disease etiology or viral status.

(G) Louvain clusters colored based on cell type annotation of the global innate immune dataset and downstream re-clustering of populations marked by dotted lines. Neutrophils (ii) and MNPs (iii) were re-clustered from the initial innate immune set (i), while DCs (iv) and macrophages (v) were re-clustered from the MNP dataset (iii).

(H) Main cluster frequencies in HCC and NT tissue. *p < 0.05 using the multiple Wilcoxon test.

(I) Circular plot of major cell type frequencies in NT tissue and HCC of different tumor grades. See also Figure S1 and Tables S1, S2, and S3.

(Figures 1G and S1E). Among the MNPs, we identified two macrophage subsets, LYVE1⁺ macrophages (c10), expressing lymphatic vessel endothelial hyaluronan receptor-1 (LYVE1), which marks tissue-resident peri-vascular macrophages, and SPP1⁺ macrophages (c17), expressing Secreted Phospho-Protein 1 (SPP1, also known as osteopontin), which marks pro-tumoral macrophages²¹ (Figure S1K; Table S3). Higher resolution clustering of their transcriptomes further distinguished seven macrophage subsets (Figures 1Gv and S1E, left), including one inflammatory (c6; *IL1B*, *CD83*, *CD86*), two FOLR2⁻TREM2⁺ (c1, 3), expressing in common *CD9*, *SPP1*, and *GNMB* among others, and four FOLR2⁺TREM2⁻ (c0, c2, c4, c5). The latter included three tissue-resident macrophage (TRM)-like clusters²² and one Kupffer cell (KC) cluster (c4; *MARCO*, *TIMD4*) expressing lower levels of *MRC1* (*CD206*). A previous study implicated NOTCH signaling in re-programming a subset of bone marrow (BM)-derived macrophages into FOLR2⁺ TRM-like macrophages.¹⁰ Cells in c2 expressed high levels of the NOTCH effector HES1 and scored highly for our TRM signature (Figure S1F; Table S3), suggesting that they might represent such a population. Among the TREM2⁺SPP1⁺ tumor-associated macrophages (TAMs) (Figure S1G), two subsets were distinguished based on differential expression of *CD163*, a *CD163*^{low} subset (TAM1 [c1]) with discriminatory expression of metallothioneins (*MT1X*, *MT1G*, *MT2A*), and a *CD163*^{high} subset (TAM3 [c3]) expressing higher levels of immune checkpoints, including *HAVCR2* (TIM3), *LGALS9* (galectin-9), *VSIR* (VISTA), *CD58*, and the metabolic immune checkpoint interleukin-4-induced-1 (*IL4I1*)²³ (Figure S1H).

DC re-clustering distinguished nine subsets including two subsets of pDCs (c3, 6; *JCHAIN*, *LILRA4*, *MZB1*, and *IL3RA*) and seven subsets of cDCs (Figures 1Giv and S1E right). DC1s (c2) were identified based on *CLEC9A*, *XCR1*, and *DNASE1L3* expression, and AS-DC (c8) expressed *AXL* and *SIGLEC6*, whereas migratory DCs (migDCs, c7),²⁴ also referred to as mature regulatory DCs (mregDCs),²⁵ expressed maturation and migration genes (*LAMP3*, *CCL19*, *CCR7*) (Figure S2C). While these subsets formed one cluster each, a notable heterogeneity was observed for DC2 forming four clusters that expressed in common *CD1C* and *CLEC10A* (Figure S2C). *FCER1A* marked DC2 c0 and c1, with c1 distinguished by high expression of *CD163*. c4 found in HCV-infected HCC patients exhibited a type I IFN signature (*IFITM3*, *GBP5*, *GBP1*, *VAMP5*), while c5 shared features with monocyte-derived DCs (moDCs), expressing monocyte-associated genes (*FCN1*, *S100A8/9*). migDC (c7) and DC2 (c4) were the only DC subsets significantly enriched in HCC compared to NT (Figure S1I).

Our analysis also distinguished different monocyte states. While all monocyte-related subsets (MNP c0, 1, 3, 4, 6, 7, 9, 15, 16) could be identified by selective expression of *FCN1* (Figure S1J), c1, 7, 9, 15, and 16 expressed the highest levels of *LILRB1* (Figure S1J), a marker of mature circulating monocytes.²⁶ These monocytes could be classified according to their *FCGR3A* (*CD16*) expression into CD14⁺CD16⁻ classical monocytes (cMonos) (c1, 16), CD14⁺CD16⁺ intermediate monocytes (iMonos) (c7), and CD14⁻CD16⁺ non-classical monocytes (ncMonos) (c9, 15) (Figure S1K). In contrast, three discrete clusters (c0, 3, 4) distinct from monocytes, macrophages, and DCs were identified

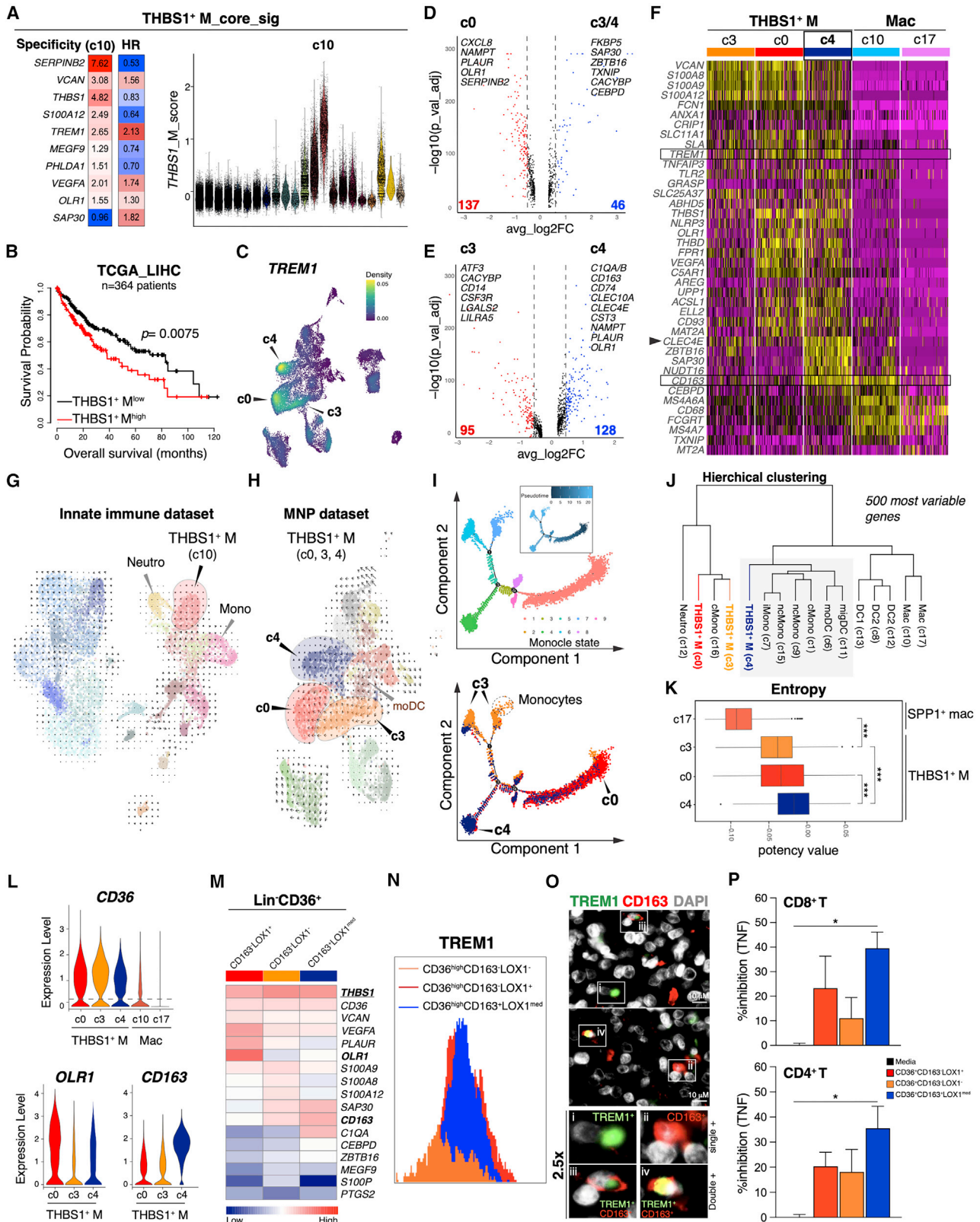
based on selective expression of THBS1 (Figures S1J–S1M). These cells express both monocyte- (*FCN1*) and neutrophil- (*CSF3R*, *TREM1*, *CLEC4E*) affiliated genes (Figures S1J–S1L) and are enriched for signatures previously ascribed to myeloid-derived suppressor cells (MDSCs).²⁷

Together, our data confirm the previously reported heterogeneity of myeloid cells in HCC^{9,10,12} but unravel THBS1⁺ M cells expressing MDSC-affiliated genes as distinct from monocytes, macrophages, DCs, and neutrophils.

Reclassification of MDSC states in HCC

Despite their significance in cancer progression, MDSCs are poorly annotated, and the phenotypic markers used to isolate them overlap with those of normal neutrophils and monocytes in both mice and humans.²⁸ Our analysis revealed three clusters of THBS1⁺ M cells representing 27.4% of all MNPs analyzed. To better characterize them, we first elucidated a core signature of 10 genes (*THBS1*, *VCAN*, *S100A12*, *SERPINB2*, *SAP30*, *MEGF9*, *TREM1*, *VEGFA*, *OLR1*, *PHLDA1*) that identify them as c10 of the innate immune dataset (Figure 2A) and c0, 3, 4 of the MNP dataset (Figure S1D). Patients in TCGA_LIHC with higher mean expression of the THBS1⁺ M core_signature have significantly poorer median overall survival (mOS) compared to patients with lower expression, independently of cancer stage, pathological features, or etiology (Figure 2B). *TREM1* encoding “triggering receptor expressed on myeloid cells 1” discriminated THBS1⁺ M cells from all other MNPs (Figure 2C). The lectin-type oxidized low-density lipoprotein (LDL) receptor 1 (LOX-1, encoded by *OLR1*), previously described as a specific marker of human polymorphonuclear (PMN)-MDSC,²⁷ had the highest expression in c0 but was also detected in other monocytes at lower levels (Figure S2A), as in Travaglini et al.²⁹ In contrast, we identified *SERPINB2* that encodes the plasminogen activator inhibitor type 2 as a more robust marker of THBS1⁺ M (c0) (Figure S2A). *MEGF9* (multiple EGF-like domains 9) was most highly expressed in THBS1⁺ M (c3), while *SAP30* (Sin3A-associated protein 30) discriminated THBS1⁺ M (c4) (Figure S2A).

To elucidate the nature of the three THBS1⁺ M subsets, we performed an analysis of differentially expressed genes (DEGs). This revealed that c0 top DEGs were neutrophil-affiliated genes, e.g., *CXCL8*, *NAMPT*, and *PLAUR* (Figure 2D; Table S4), and c3 was discriminated by monocyte lineage genes *ATF3*, *CD14*, *CSF3R*, *CACYBP*, *LGALS2*, and *LILRA5* (Figure 2E; Table S4), whereas c4 DEGs included genes affiliated to macrophages and DCs (*C1QA/B/C*, *CD163* and *CLEC10A*, *CST3*) in addition to genes shared with c0 and highly expressed in neutrophils (*NAMPT*, *OLR1*, *PHLDA1/2*, *PLAUR*) (Figures 2E and 2F; Table S4). To identify the possible origin of THBS1⁺ M cells, we applied RNA velocity on the innate immune dataset, which revealed that the THBS1⁺ M population does not originate from differentiated monocytes or neutrophils (Figure 2G) but from a moDC precursor, as shown by higher resolution velocity analysis of the MNP dataset (Figure 2H). To explore the dynamic regulation among the three THBS1⁺ M subsets, we mapped their position along an inferred trajectory through Pseudotime ordering, which revealed three states (Figure 2I) with distinct temporally expressed genes along the Pseudotime (Figure S2B). Principal component analysis revealed that moDC (c6), migDC (c11),



(legend on next page)

and THBS1⁺ M (c4) occupied an intermediate transcriptional state between monocytes, macrophages, and DCs (Figure S2C). This was further confirmed by hierarchical clustering that connected THBS1⁺ M (c4) to a branch containing moDC (c6) and migDC (c7) (Figure 2J). Calculation of differentiation potency estimates^{31,32} revealed that THBS1⁺ M (c4) had higher signaling promiscuity/entropy (higher capacity to differentiate to different lineages) compared to THBS1⁺ M (c0), THBS1⁺ M (c3), and SPP1⁺ mac (c17) (Figure 2K). Similar results were obtained with predicted ordering of differentiation states by CYTOTRACE, which positioned THBS1⁺ M (c4) in an intermediate state compared to DCs and monocytes/macrophages (Figure S2D).

We next sought to investigate the function of the three THBS1⁺ M populations. We searched for cell surface proteins differentially expressed among them. We found that the scavenger receptor CD36 was highly expressed on all three THBS1⁺ M subsets compared to macrophages (Figure 2L) or other MNPs (Figure S1K), and we identified *OLR1* (encoding LOX-1) and *CD163* as selective markers capable of distinguishing the three subsets apart (Figure 2L). This was validated by FACS (Figure S2E) and bulk RNA-seq of the sorted populations (Figures 2M–S2I; Table S4). Consistent with our scRNA-seq data (Figure 2C), *TREM1* was expressed on all three THBS1⁺ M subsets albeit with higher surface expression on the CD36^{high}CD163[–]LOX-1[–] (corresponding to c0) and CD36^{high}CD163⁺LOX-1^{med} (corresponding to c4) populations (Figure 2N). Besides *TREM1*, THBS1⁺ M (c4) selectively expressed *CLEC4E* (also primarily expressed on neutrophils) (Figures 2F and S1L). THBS1⁺ M (c4) can thus be identified as CD36^{high}CD163⁺LOX-1^{med}TREM1^{high}CLEC4E⁺, which we validated by immunofluorescence (IF) analysis of HCC patient tumors *in situ* using anti-CD163 with either anti-TREM1 or anti-CLEC4E (Figures 2O–S3C) and by FACS us-

ing a conventional “MDSC” staining strategy,³³ which further identified this CD163⁺TREM1⁺ population as CD33⁺HLA-DR^{med} population (Figure S2F). To assess immunosuppressive activity, we co-cultured FACS-sorted myeloid subsets according to the strategy in Figure S2E with activated CD8⁺ T or CD4⁺ T cells purified from healthy donors or with a high-avidity Th1-polarized CD4⁺ T cell clone reactive to telomerase (TERT) peptide UCP4, as in Lauret Marie Joseph et al.³⁴ All three subsets inhibited T cell production of effector cytokines (Figures 2P, S2G, and S2H), albeit the CD36⁺CD163⁺LOX-1^{med} population (corresponding to c4) showed the most potent inhibitory effect. As a control, we generated human monocyte-derived suppressor cells (HuMoSCs)³⁵ and confirmed that they suppressed cytokine production by activated T cells (Figures S2J and S2K). Phenotypic characterization of these HuMoSCs showed that they were primarily CD163⁺ (>85%) and highly expressed *TREM1* (Figures S2L and S2M), suggesting that an immunosuppressive capacity can be identified by dual expression of *TREM1* and *CD163*. Myeloid cells exert their immunosuppressive functions through different mechanisms, e.g., via reactive oxygen species, nitric oxide, arginase, prostaglandin E2 (PGE₂), anti-inflammatory cytokines (e.g., IL-10 and TGFβ), and cell surface immune checkpoints such as PD-L1.³⁶ Interrogation of the expression of central effectors in these pathways revealed that THBS1⁺ M (c4) expressed the highest levels of *TGFB1* (Figure S2N), which was also observed in *ex vivo*-generated HuMoSCs (Figure S2O). They also exhibited the highest levels of *IL13RA1*, which encodes a chain of the receptor for IL-13, a cytokine implicated in TGFβ induction.^{37,38} In addition, they had elevated levels of *PTGES2* and *PTGER2*, encoding a PGE₂ synthase and receptor, respectively, as well as *ODC1*, encoding ornithine decarboxylase that acts downstream of arginase as the rate-limiting enzyme in the polyamine biosynthesis

Figure 2. Identification and characterization of THBS1⁺ M_{reg} cells

- (A) Left, THBS1⁺ M (c10, innate immune dataset) core signature specificity and association with mOS in patients with HCC from TCGA_LIHC. HR, hazard ratio; right, violin plot depicting c10 signature score in innate immune clusters.
- (B) Kaplan-Meier survival curves of patients with HCC (n = 364)³⁰ according to expression of the THBS1⁺ M_{core} signature.
- (C) Density plot representing the expression of *TREM1* as a discriminatory marker of the three THBS1⁺ M clusters of the MNP re-clustering.
- (D) Volcano plot depicting DEGs between THBS1⁺ M (c0) and other THBS1⁺ M cells (c3+c4).
- (E) Volcano plot depicting DEGs between THBS1⁺ M (c3) and THBS1⁺ M (c4).
- (F) Heatmap representing the expression of selected genes from CIBERSORTx top 40 scored genes of THBS1⁺ M (c4) signature. 100 cells in each cluster are shown.
- (G) RNA velocity of innate immune cells.
- (H) RNA velocity of MNPs.
- (I) Pseudotime trajectory analysis using Monocle2 of the three THBS1⁺ M clusters, colored by Monocle state (upper panel), Pseudotime (upper small panel), or Seurat cluster (lower panel).
- (J) Phylogenetic relationships of MNPs and neutrophils based on the expression of top 500 most variable genes.
- (K) Boxplots of signaling entropy rates (y axis, also named differentiation potency) in the three THBS1⁺ M clusters and the SPP1⁺ Mac cluster (c17). Center line, median; box limits, upper and lower quartiles; whiskers, maximum and minimum values. ***p < 0.001 using the Wilcoxon test.
- (L) Violin plots depicting expression of *CD36*, *OLR1*, and *CD163* in the indicated MNP clusters.
- (M) Expression of selected genes among the different FACS-sorted myeloid subsets (bulk transcriptomics data), normalized using the geometric mean expression of FACS-sorted innate immune cells from 6 HCC patients.
- (N) Histograms depicting *TREM1* expression among the different THBS1⁺ M subsets according to differential expression of LOX-1 and CD163 in the Lin[–]CD36^{high} population.
- (O) Epifluorescence images of HCC tumor sections stained with antibodies against *TREM1* (OPAL 520) and *CD163* (OPAL 650) together with DAPI (gray) to label nuclei. Insets correspond to boxed regions.
- (P) Quantification of the % inhibition of TNFα production by CD8⁺ T and CD4⁺ T cells stimulated with anti-CD3/CD28 beads in co-culture with different myeloid subsets sorted from HCC surgical resections according to the gating strategy in Figure S3E. n = 3 HCC patients. Error bars represent SEM. *p < 0.05 using the Kruskal-Wallis test. See also Figure S2 and Table S4.

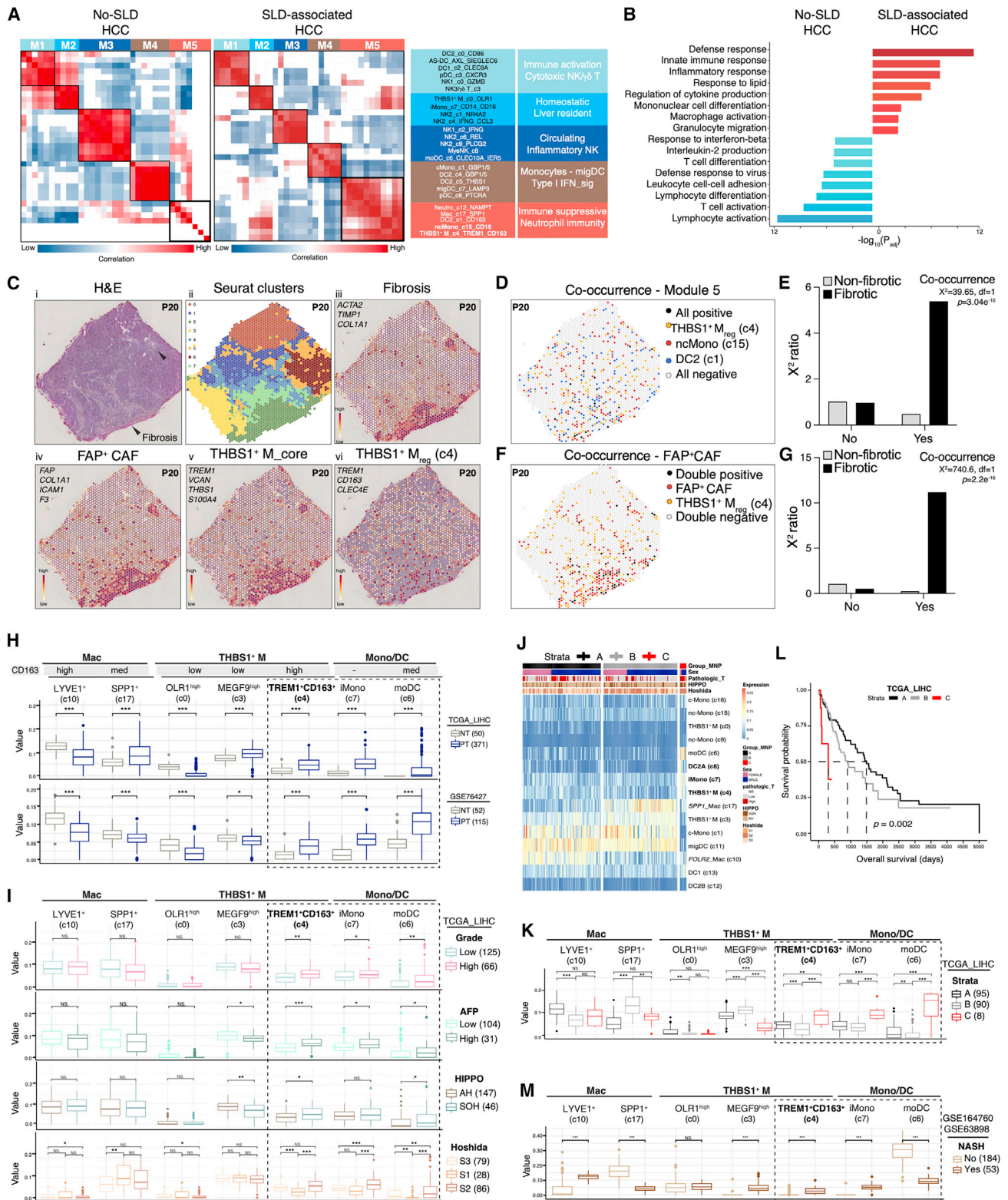


Figure 3. THBS1⁺ M_{reg} cells expand in SLD-associated HCC and populate fibrotic lesions

(A) Cellular modules based on Pearson's correlations of cluster cell counts and further hierarchical clustering (SLD-associated HCC, n = 5; non-SLD HCC, n = 5). Non-significant correlations are represented by white squares ($p > 0.05$). Key clusters in each module are shown on the right. TIME, tumor immune microenvironment.

(legend continued on next page)

pathway. They shared with THBS1⁺ M (c0) high expression of *ATF4*, encoding activating transcription factor 4, an endoplasmic reticulum stress effector required for MDSC immunosuppressive function.³⁹

THBS1⁺ M_{reg} cells expand in SLD-associated HCC and are enriched at fibrotic lesions

To elucidate the impact of HCC etiology on the tumor immune microenvironment (TIME), we first defined innate immune cell subset co-occurrence by Pearson correlations among cluster counts from all patients (Figures 3A and S3A). This identified five cellular modules, including one (M5) enriched in neutrophil immunity and immunosuppressive pathways, encompassing THBS1⁺ M_{reg} (c4), which was significantly expanded in SLD-associated HCC in our discovery cohort (n = 10) (Figures 3A, 3B, S3A, and S3B; Table S4). To validate this observation, we quantified THBS1⁺ M_{reg} cells in tumor tissue sections from 10 additional HCC patients with or without SLD (n = 5 each) by IF staining with anti-CD163 and anti-CLEC4E antibodies. This analysis revealed increased CD163⁺CLEC4E⁺ cell numbers in SLD-compared to non-SLD-associated HCC (Figure S3C). To map the *in situ* distribution of these cells within tumors, we used stRNA-seq to analyze tissue sections from two patients with HCC containing fibrotic lesions. Transcriptomics from 2,261 to 1,987 spots were obtained at a median depth of 34,526 and 26,017 unique molecular identifiers (UMIs)/spot and 5,882 and 4,954 genes/spot for patients #20 and #23, respectively (Table S2). Unbiased clustering identified eight clusters in patient #20 (Figure 3C) and ten clusters in patient #23 (not shown). Based on spot feature expression, we identified clusters 2 and 5 in patient #20 and cluster 8 in patient #23 as scoring highly for a fibrosis signature (*COL1A1*, *TIMP1*, *ACTA2*) (Figures 3C and S3D). We next interrogated the *in situ* expression of a gene set (*TREM1*, *VCAN*, *THBS1*, *S100A4*) that discriminated THBS1⁺ M cells from other innate immune cells (Figure S1M). Our results revealed an overlap in the expression of this gene set with

that marking fibrotic lesions (Figures 3C and S3D). *VCAN*, *THBS1*, and *S100A4* may also be expressed by fibroblasts indicating that THBS1⁺ M cells are geared with a pro-fibrotic machinery, consistent with their high expression of *TGFB1*, *IL13RA1* (Figure S2N), and *TIMP1* (Figure S1M). To ensure specific detection of THBS1⁺ M (c4) cells, we next examined the expression of a more-restricted signature composed of *TREM1*, *CD163*, and *CLEC4E* (Figure S1K; Table S3). Our results revealed that THBS1⁺ M (c4) cells were found at fibrotic lesions (Figures 3C and S3D). We next used linear regression and Pearson's chi-squared (χ^2) to test the number of spots significantly enriched in multiple immune populations in both fibrotic and non-fibrotic regions of HCC. This analysis showed significant fibrosis-associated spatial cell-to-cell co-occurrence of THBS1⁺ M_{reg} (c4), ncMono (c15), and DC2 (c1), subsets enriched in the SLD-HCC-associated module M5 (Figures 3D, 3E, S3E, and S3F). Specific CAF sub-populations promote immunosuppression in the TME and have been linked to immunotherapy resistance.^{40,41} Immunosuppressive CAFs exhibit an activated phenotype and express markers such as fibroblast-activation protein (*FAP*) and components of the desmoplastic structures, including collagens (*COL1A1*, *COL3A1*), integrins (*ICAM1*), and tissue factor (*F3*). We interrogated the spot feature expression of an FAP⁺ CAF signature (*FAP*, *COL1A1*, *ICAM1*, *F3*) in our stRNA-seq data and observed overlapping spatial distribution with that of THBS1⁺ M (c4) (Figures 3C and S3D), suggesting potential crosstalk between these two populations. This was further validated using spot co-occurrence (Figures 3F, 3G, S3G, and S3H) and cell-cell communication (CellChat) analyses uncovering significant pathways (Figure S3I) and cytokine ligand-receptor pairs (Figure S3J) predicted to mediate their functional interactions.

Together, these results point to a module of cells encompassing THBS1⁺ M (c4) that expands in SLD-associated HCC and correlates with pro-fibrogenic, immunosuppressive CAFs in tumors.

(B) Pathway enrichment analysis using g:Profiler according to DEGs between SLD versus non-SLD in the innate immune dataset.

(C) Tumor section from a patient with HCC (P20) analyzed by stRNA-seq using Visium. i, tumor section stained with H&E; ii, overlapping localization of spatial Louvain Seurat clusters; spatial scoring of a gene signature marking (iii) fibrosis (*ACTA2*, *TIMP1*, *COL1A1*); (iv) FAP⁺ CAFs (*FAP*, *COL1A1*, *ICAM1*, *F3*); (v) THBS1⁺ M core (*TREM1*, *VCAN*, *THBS1*, *S100A4*); and (vi) THBS1⁺ M_{reg} (*TREM1*, *CD163*, *CLEC4E*).

(D) Spatial co-occurrence analysis of THBS1⁺ M_{reg} (c4), ncMono (c15), and DC2 (c1). Spots are colored according to absence of these populations (gray), presence of only one of them (yellow, red, or blue), or presence of the three populations (black).

(E) Chi-squared (χ^2) statistics to test the co-occurrence of populations ("yes" for black spots or "no" for gray spots in D) in non-fibrotic (gray) or fibrotic (black) regions. χ^2 ratio corresponds to observed/expected ratios (Roe).

(F) As in (D) but for spatial co-occurrence of THBS1⁺ M_{reg} (c4) and FAP⁺ CAFs.

(G) As in (E).

(H) Boxplots depicting the predicted scores of macrophage, THBS1⁺ M, and Mono/DC subsets by CIBERSORTx deconvolution of bulk transcriptomics data from two liver cancer cohorts (TCGA_LIHC and GSE76427). NT, non-tumoral; PT, primary tumor.

(I) Boxplots depicting the predicted scores of macrophage, THBS1⁺ M, and Mono/DC subsets by CIBERSORTx deconvolution of bulk transcriptomics data from TCGA_LIHC according to tumor grade (low, pathologic T grade 1 and 2; high, pathologic T grade 3 and 4), serum AFP (<300 or >300), HIPPO status, or Hoshida class.

(J) Heatmap depicting predicted scores of MNP populations by CIBERSORTx deconvolution of bulk transcriptomics data from TCGA_LIHC. Unsupervised hierarchical clustering of patients depicts three strata: A, B, and C.

(K) Boxplots depicting the predicted scores of macrophage, THBS1⁺ M, and Mono/DC subsets by CIBERSORTx deconvolution of bulk transcriptomics data from TCGA_LIHC according to strata identified in (J).

(L) Kaplan-Meier survival curves of patients with HCC (n = 193) from TCGA_LIHC stratified according to the three strata identified in (J) based on MNP infiltrate profiles.

(M) Boxplots depicting the predicted scores of macrophage, THBS1⁺ M, and Mono/DC subsets by CIBERSORTx deconvolution of microarray expression data from patients with NASH-HCC or non-NASH-HCC (GSE164760 and GSE63898). Center line, median; box limits, upper and lower quartiles; whiskers, maximum and minimum values. ***p < 0.001, **p < 0.01, *p < 0.05 using Wilcoxon tests for (H), (I), (K), and (M). See also Figure S3 and Table S4.

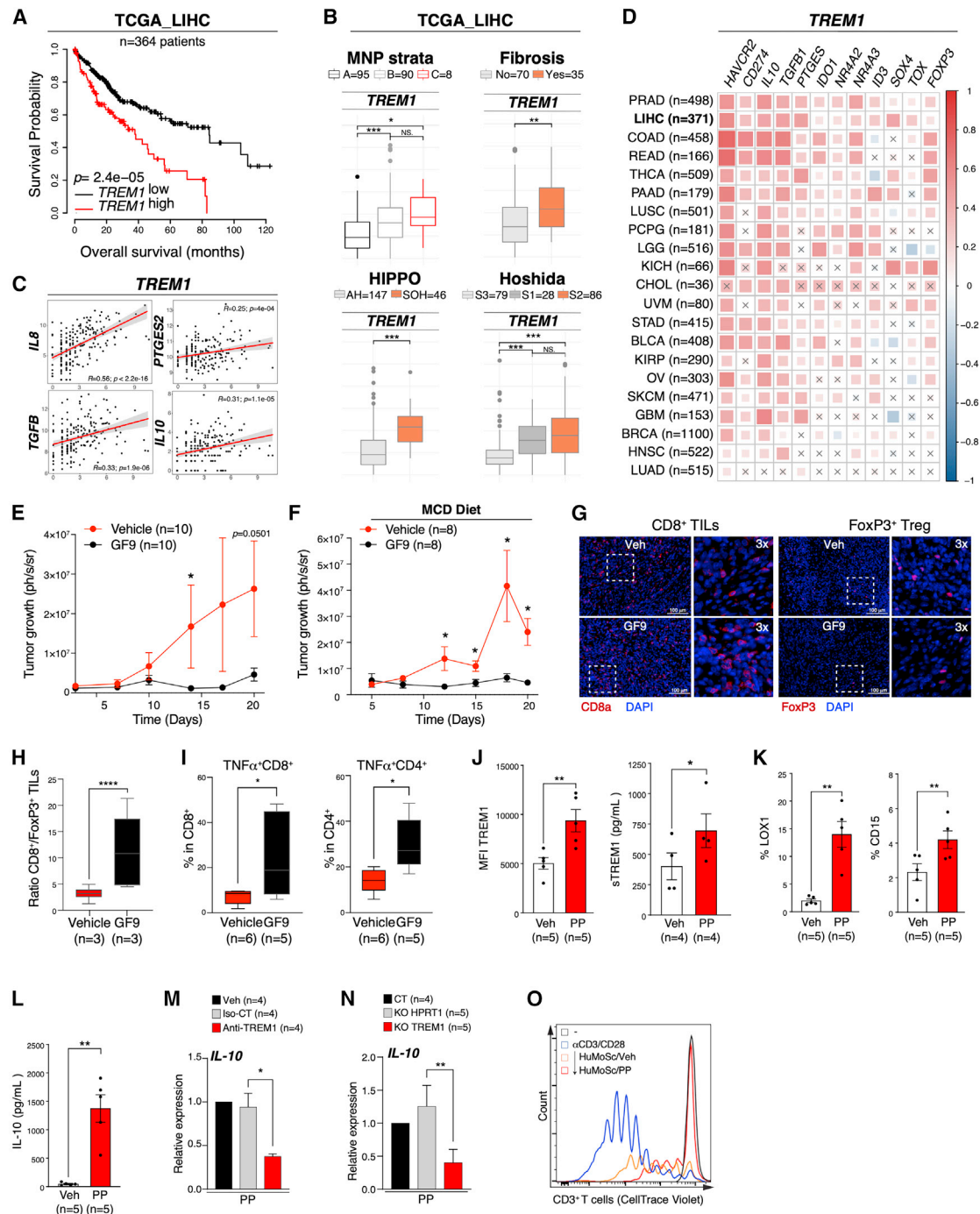


Figure 4. TREM1 associates with poor prognosis and contributes to the immunosuppressive activity of THBS1⁺ M_{reg} cells

(A) Kaplan-Meier survival curves of patients with HCC (n = 364)³⁰ according to *TREM1* expression.
 (B) Boxplots depicting the expression of *TREM1* in TCGA_LIHC according to patient strata (Figure 3J), fibrosis, HIPPO status, or Hoshida class.
 (C) Scatterplots depicting Pearson correlations between the log-normalized expression of *TREM1* and *TGFB*, *IL10*, *IL8*, or *PTGES2*.
 (D) Correlation between the expression of *TREM1* and genes implicated in immunosuppression (*HAVCR2*, *CD274*, *IL10*, *TGFB1*, *PTGES*, *IDO1*), T cell exhaustion (*NR4A2/3*, *ID3*, *SOX4*, *TOX*), or T_{reg} (*FOXP3*) in different solid tumors. Values were obtained using TIMER2.0. Black crosses indicate non-significant correlations.
 (E) Tumor volume by luminescence quantification in a transplantable liver orthotopic model of HCC using Hep5.1C cell line transduced with a lentivirus encoding luciferase. Mice were treated with a vehicle control or the *TREM1* inhibitory peptide GF9. Pool of two independent experiments of 5 mice per condition. Error bars represent SEM. *p < 0.05 using the Mann-Whitney test.

(legend continued on next page)

THBS1⁺ M_{reg} cells correlate with poor clinical outcomes in patients with HCC

To extend our findings to a larger cohorts of patients, we used the deconvolution algorithm CIBERSORTx⁴² trained with our scRNA-seq data to infer the intra-tumoral abundance of MNP subsets defined in our study in primary tumors (PTs) and adjacent NT tissue of patients with HCC in two cohorts: TCGA_LIHC (371 patients) and GSE76427 (115 patients).⁴³ Our results show a consistent tumoral depletion of LYVE1⁺ macrophages (c10) and OLR1^{high} PMN-MDSC-like (c0) in both cohorts but a variable distribution of SPP1⁺ macrophages (c17) and MEGF9^{high} M-MDSC-like (c3) cells. In contrast, THBS1⁺ M_{reg} (c4), iMono (c7), and moDC (c6) were consistently more abundant in the PT compared to NT tissue (Figures 3H and S3K) and associated with higher pathological tumor grade (stages III and IV), serum alpha-fetoprotein (AFP) levels, an important prognostic biomarker of mortality,⁴⁴ the silence of HIPPO [SOH] signature, reported to predict poor prognosis in patients with HCC,⁴⁵ and the Hoshida S2 subclass, characterized by larger and poorly differentiated tumors, elevated serum AFP, and poor mOS⁴⁶ (Figures 3I and S3L).

We wondered whether the nature of the myeloid infiltrate could stratify HCC patients and serve as an immunological biomarker of clinical outcomes. To address this, we performed unsupervised hierarchical clustering of HCC patients in TCGA_LIHC based on CIBERSORTx predicted scores of the MNP populations characterized in this study. Tumor-infiltrating MNP profiles divided HCC patients into three strata (Figures 3J and 3K) with significantly different mOS (Figure 3L). Group A patients with the best mOS had higher proportions of LYVE1⁺ macrophages (c10) (Figures 3J–3I), whereas group B patients with an intermediate mOS had more SPP1⁺ macrophages (c17) (Figures 3J–3I). Group C patients, with markedly reduced mOS (Figure 3L), had the highest proportions of THBS1⁺ M_{reg} (c4), moDC (c6), and iMono (c7) (Figure 3K). Given the sexual dimorphism present in HCC patients, we further explored the effect of sex on estimated proportions of MNPs in TCGA_LIHC in each patient strata and quantified survival according to sex and MNP content. The data show sex-specific differences in MNP subsets and patient

survival according to MNP class (Figures S3M and S3N). The analysis of sex-specific difference of the populations enriched in strata C (poorest survival) was limited by the small number of patients in this severe group. To extend our findings, we next examined the enrichment of THBS1⁺ M_{reg} specifically in NASH-HCC. We explored two cohorts of patients (GSE164760 and GSE63898) including 53 with NASH-HCC and 184 with HCC of other etiologies. This analysis showed higher predicted content of THBS1⁺ M_{reg} in patients with NASH-HCC (Figures 3M and S3O), identifying THBS1⁺ M_{reg} cells, as a tumor-infiltrating myeloid cell population, enriched in SLD-HCC and associated with disease severity.

TREM1 confers immunosuppression and associates with poor prognosis in HCC

Among the 10 genes constituting the THBS1⁺ M_{core} signature, *TREM1* confers the highest hazard ratio on HCC survival in TCGA_LIHC (Figures 2A and 4A), consistent with previous reports.^{47,48} We wondered whether *TREM1* per se is associated with poor clinical outcomes and if it plays a direct role in immunosuppression. We interrogated *TREM1* expression in the three HCC patient groups from TCGA_LIHC classified according to MNP profiles. We observed the highest expression of *TREM1* in group C patients (Figure 4B), who have the highest content of THBS1⁺ M_{reg} cells and the poorest mOS (Figures 3K–3L). In addition, *TREM1* was significantly associated with fibrosis, SOH status, and the Hoshida S2 class (Figure 4B). Expression of *TREM1* positively correlated with that of *TGFB*, *IL10*, *PTGES2*, and *IL8* in HCC (Figure 4C), as well as with several effectors of immunosuppression and CD8 T cell exhaustion in several solid tumors (Figure 4D), pointing to *TREM1* as a potential effector of tumor progression and immunosuppression.

To experimentally address the role of *TREM1* in HCC tumor control, we investigated the impact of its inhibition in mouse models, either in the absence or presence of underlying SLD, which was induced by feeding C57Bl/6 mice with a methionine- and choline-deficient (MCD) diet and evidenced by increased aspartate aminotransferase (AST) levels (Figure S4A) prior to Hep55.1C tumor orthotopic implantation. Our results show that

(F) C57Bl/6/J mice were fed a methionine- and choline-deficient (MCD) diet prior to tumor inoculation as in (E). n = 8 mice per condition. Error bars represent SEM. *p < 0.05 using the Mann-Whitney test.

(G) Epifluorescence images of Hep55.1C tumors liver sections from mice treated with vehicle control or GF9 as in (E) on day 20 post Hep55.1C injection stained with antibodies against CD8a or FoxP3 and DAPI to label nuclei. Insets correspond to boxed regions.

(H) Ratio of quantified stain-positive cells in (G). n = 3 mice per treatment. Error bars represent SEM. ****p < 0.0001 using the unpaired t test.

(I) Percentage (%) of TNF⁺CD8⁺ cells (left) and of TNF⁺CD4⁺ cells (right) in residual Hep55.1C tumors. n = 5 to 6 mice per condition. Error bars represent SEM. *p < 0.05 using the unpaired t test.

(J) Mean fluorescence intensity (MFI, median) of *TREM1* expression on HuMoSC (left) and concentration of s*TREM1* released from HuMoSC (right) treated on day 6 of differentiation with vehicle (water, white bars) or a complex of peptidoglycan (PGN) and PGN recognition protein 1 (PGLYRP1) (PP, red bars) for 24 h. n = 4–5 donors. Error bars represent SEM. *p < 0.05, **p < 0.01 using the paired t test.

(K) Quantification of HuMoSCs positive for the expression of *LOX-1* or *CD15* following a 24-h treatment with either vehicle (water) or PP as in (J). n = 5 donors. Error bars represent SEM. **p < 0.01 using the paired t test.

(L) Bar graphs depicting the concentration of soluble *IL-10* released from HuMoSCs treated with vehicle (water) or PP as in (J). n = 5 donors. Error bars represent SEM. **p < 0.01 using the paired t test.

(M) Expression of *IL10* in HuMoSCs measured by qRT-PCR. HuMoSCs were treated with PP complex alone (vehicle, water) or together with ino-2 antibody that blocks *TREM-1* (red bars) or isotype control (Iso-CT; gray bars). n = 4 donors. Error bars represent SEM. *p < 0.01 using the paired t test.

(N) Expression of *IL10* in HuMoSCs measured by qRT-PCR. HuMoSCs were treated with PP complex for 24 h. HuMoSCs were generated from monocytes nucleofected with sgHPRT1 (gray bars), sg*TREM1* (red bars), or vehicle (PBS, black bars). n = 5 donors. Error bars represent SEM. **p < 0.01 using the paired t test.

(O) Representative FACS histogram depicting CellTrace Violet dilution as a readout of CD3⁺ T cell proliferation over 6 days in the listed conditions. Veh, vehicle (water). See also Figure S4.

inhibition of TREM1 signaling by the GF9 peptide that interferes with TREM1 binding to its signaling adaptor DAP12⁴⁹ resulted in rapid tumor eradication (Figures 4E and 4F) and was more efficient than anti-PD-1 in the SLD context (Figure S4B). The effects of GF9 on tumor growth correlated with a significant increase in CD8⁺/FoxP3⁺ T cell ratio in the TME (Figures 4G and 4H) and enhanced T cell activation (Figure 4I). The rapid tumor eradication kinetics observed with GF9 was comparable to that with anti-Gr1 (Figure S4C), which depleted intra-tumoral Ly6G⁺ Ly6C⁻ cells expressing TREM1 (Figure S4D), arguing albeit indirectly that the observed GF9 effects are mediated by TREM1 inhibition on these cells. To address the specific role of TREM1 in myeloid cells, we used the HuMoSC model in co-culture with T cells *ex vivo*. We observed an induction of TREM1 cell surface expression in HuMoSC compared to monocytes (Figure S4E), suggesting that a suppressive function is linked to TREM1 expression. Treatment of HuMoSC with the TREM1 ligand PGLYRP1 (peptidoglycan recognition protein 1) in complex with peptidoglycan (PGN) (PP) further increased TREM1 cell surface expression and its release (sTREM1) (Figure 4J) and induced LOX-1 and CD15, two markers associated with a granulocytic phenotype (Figure 4K). In addition, PP induced IL-10 (Figure 4L), which was TREM1 dependent as demonstrated using anti-TREM1 antibody (Figure 4M) or *TREM1* knockout (Figures 4N and S4F). Importantly, TREM1 stimulation by PP further enhanced the capacity of HuMoSCs to suppress T cell proliferation (Figure 4O) and effector functions, e.g., inhibition of TNF α production (Figure S4G), which was partially mediated by IL-10 (Figure S4G). Together, these results suggest that the SLD environment promotes the expansion of THBS1⁺ M_{reg} cells with strong immunosuppressive and pro-tumoral functions and point to TREM1 as a potential immunotherapeutic target in HCC.

DISCUSSION

Here, investigation of the innate immune cellular landscape of patients with HCC revealed previously unreported myeloid cell subsets. Our work presents four findings with important clinical implications: (1) HCC-associated genesis of cells with intermyeloid mixed states, potentially stemming from emergency myelopoiesis⁵⁰ and/or trained immunity responses to tumor growth^{51–53}; (2) a heterogeneity of myeloid states, yet with only specific subsets infiltrating the tumor; (3) identification of THBS1⁺ M_{reg} subset with immunosuppressive activity that expands in the SLD setting, populates fibrotic lesions in HCC, and associates with poor prognosis; and (4) demonstration of a role of TREM1 in amplifying the immunosuppressive function of human monocyte-derived suppressor cells and in promoting HCC growth *in vivo*.

Our analysis demonstrates the heterogeneity of myeloid populations and shows that THBS1 expression marks myeloid cells enriched in MDSC signature.²⁷ They were found in three distinct states in HCC, including one with dual macrophage/DC and granulocyte features. Our results show that this subset exhibits a more potent immunosuppressive activity compared to other THBS1⁺ M cells. We show, using spatial transcriptomics, that this subset populates fibrotic lesions in HCC in close association with pro-fibrogenic and pro-tumorigenic CAFs. This subset was

more abundant in HCC in the SLD setting compared to other etiologies, as shown in our discovery and validation cohorts and predicted by deconvolution of larger patient cohort datasets.

TREM1 has been previously described as an amplifier of inflammation.⁵⁴ It was initially proposed to promote HCC development through pro-inflammatory cytokine production by Kupffer cells.⁵⁵ However, this early analysis used a non-discriminatory staining that marks a heterogeneous group of myeloid cells, preventing precise identification of deleterious myeloid cell subsets. Our scRNA-seq data reveal that TREM1 is a discriminatory feature of THBS1⁺ M cells distinguishing them from other MNPs in the liver of HCC patients. We show that TREM1 expression per se is predictive of poor clinical outcomes in HCC and is associated with the expression of immunosuppression and exhaustion markers in several solid tumors. TREM1 has been implicated in mediating liver fibrosis⁵⁶ and immunotherapy resistance in a mouse model of liver cancer.⁵⁷ Additionally, a recent study⁵⁸ reported that sTREM1 might engage Robo2 to activate hepatic stellate cells and liver fibrosis, pointing to TREM1 as a deleterious molecule in liver diseases. We demonstrate that TREM1 ligation by cognate ligand on HuMoSCs promotes their acquisition of features linked to a suppressive phenotype and boosts their capacity to suppress T cell proliferation and effector functions.

Collectively, our study supports the stratification of patients according to HCC etiology to define optimal therapeutic regimens, and it points to TREM1 targeting as an attractive therapeutic option in SLD-associated HCC.

Limitations of the study

In this study, we characterized the innate immune landscape of a small cohort of patients with HCC and identified a subset of THBS1⁺ myeloid cells that expands in the SLD etiology. Future studies are needed to identify this population by multiplex immunofluorescence in larger patient cohorts. These studies will also help to interrogate the emergence of this myeloid population by SLD triggers and its functional relationship with other cells in the TME. Specific deletion of *Trem1* in the myeloid compartment and application of additional models of SLD will help determine the extent to which the observed effects of GF9 are attributed to TREM1 expression on myeloid cells with features similar to THBS1⁺ M_{reg} cells.

STAR★METHODS

Detailed methods are provided in the online version of this paper and include the following:

- KEY RESOURCES TABLE
- RESOURCE AVAILABILITY
 - Lead contact
 - Materials availability
 - Data and code availability
- EXPERIMENTAL MODEL AND STUDY PARTICIPANT DETAILS
 - Study participants
 - Animal models
 - Cell culture

● **METHOD DETAILS**

- Generation of HuMoSCs
- CRISPR/Cas9 mediated TREM1 Knock-out
- Human tissue dissociation
- Flow cytometry staining
- Single-cell FACS sorting
- scRNA-seq
- Visium spatial gene expression processing
- Co-culture experiments
- MCD-diet mouse model
- Orthotopic tumor injection and tumor growth monitoring
- Mouse tumor dissociation
- Immunofluorescence and multiplex Immunohistochemistry staining and imaging
- RNA extraction and RT-qPCR
- Transcriptomic analyses of sorted innate immune cells and sorted THBS1⁺ myeloid cells – Sample preparation
- scRNA-seq data processing, quality control and cleaning
- Cell doublet detection and removal
- Normalization and data integration
- Unsupervised clustering, dimensionality reduction and data visualization
- Cell type/state annotation
- Identification of signature genes
- Phylogenetic relationships of clusters based on gene expression
- Trajectory inference
- RNA velocity estimation
- Estimation of differentiation potency or signaling entropy
- Differential expression analysis, gene ontology and gene set enrichment analysis
- Pre-processing and visualization of spatial transcriptomic data
- Spatial co-occurrence analysis
- Cell-cell communication analysis
- Transcriptomic source data of external cohorts
- Immuno-deconvolution and cancer genomics
- Transcriptomic analyses of sorted innate immune cells and sorted THBS1⁺ monocytes – data processing and analysis

● **QUANTIFICATION AND STATISTICAL ANALYSIS**

SUPPLEMENTAL INFORMATION

Supplemental information can be found online at <https://doi.org/10.1016/j.celrep.2024.113773>.

ACKNOWLEDGMENTS

We thank Aurélie Le Dantec, Gaël Galli, and Sébastien Lillo from the Saleh lab for help and advice and Marie-Elise Truchetet, Damien Brisou, Elodie Sifré, and Christine Varon from the University of Bordeaux for materials and technical support. We thank Alexander B. Sigalov (SignaBlok, Inc.) for advice on GF9 peptide utilization *in vivo* and the Llovet team for help on best annotating NASH and non-NASH cohorts. We thank TBMCORE platforms (CBiB, CRISP'edit, FACSility, One Cell, and Histopatology platforms), the Magendie Neurocenter laser microdissection platform, the Bordeaux Imaging Center,

the GeT-Santé facility in Toulouse, and the CRB-K (Center de Ressources Biologiques – Cancer) of Bordeaux University Hospital. This work is funded by operating grants to M.S. from the ARC foundation, IDEX Bordeaux, and ITMO cancer and an infrastructure grant to M.S. from the New Aquitaine region. J.G. and D.C. are funded by the ARC foundation and ITMO cancer, and E.R. received a studentship from the SIRIC BRIO. J.G., D.C., and E.R. also received salary support from the New Aquitaine region.

AUTHOR CONTRIBUTIONS

Conceptualization, J.G., D.C., and M.S.; investigation, J.G., D.C., E.R., T.B., A.Z., and M.-A.D.; formal analysis, J.G., D.C., and M.S.; resources, N.L., O.A., B.L., C.L., L.C., and M.D.; writing—original draft, M.S.; writing—review & editing, J.G., D.C., and M.S.; supervision, M.N. and M.S.; funding acquisition, M.S. All of the authors commented on the manuscript.

DECLARATION OF INTERESTS

M.D. is co-founder, chief scientific officer, and employee of Inotrem SA, a French company that develops TREM1 inhibitors.

Received: April 19, 2023

Revised: November 5, 2023

Accepted: January 25, 2024

Published: February 12, 2024

REFERENCES

1. Rinella, M.E., Lazarus, J.V., Ratzliff, V., Francque, S.M., Sanyal, A.J., Kanwal, F., Romero, D., Abdelmalek, M.F., Anstee, Q.M., Arab, J.P., et al. (2023). A multisociety Delphi consensus statement on new fatty liver disease nomenclature. *Hepatology* 78, 1966–1986. <https://doi.org/10.1097/HEP.0000000000000520>.
2. Llovet, J.M., Kelley, R.K., Villanueva, A., Singal, A.G., Pikarsky, E., Roayaie, S., Lencioni, R., Koike, K., Zucman-Rossi, J., and Finn, R.S. (2021). Hepatocellular carcinoma. *Nat. Rev. Dis. Primers* 7, 6. <https://doi.org/10.1038/s41572-020-00240-3>.
3. Finn, R.S., Qin, S., Ikeda, M., Galle, P.R., Ducreux, M., Kim, T.Y., Kudo, M., Breder, V., Merle, P., Kaseb, A.O., et al. (2020). Atezolizumab plus Bevacizumab in Unresectable Hepatocellular Carcinoma. *N. Engl. J. Med.* 382, 1894–1905. <https://doi.org/10.1056/NEJMoa1915745>.
4. Abou-Alfa, G.K., Lau, G., Kudo, M., Chan, S.L., Kelley, R.K., Furuse, J., Sukeepaisarnjaroen, W., Kang, Y.K., Van Dao, T., De Toni, E.N., et al. (2022). Tremelimumab plus Durvalumab in Unresectable Hepatocellular Carcinoma. *NEJM Evid.* 1. <https://doi.org/10.1056/EVIDoa2100070>.
5. Giraud, J., Chalopin, D., Blanc, J.F., and Saleh, M. (2021). Hepatocellular Carcinoma Immune Landscape and the Potential of Immunotherapies. *Front. Immunol.* 12, 655697. <https://doi.org/10.3389/fimmu.2021.655697>.
6. Pfister, D., Núñez, N.G., Pinyol, R., Govaere, O., Pinter, M., Szydlowska, M., Gupta, R., Qiu, M., Deczkowska, A., Weiner, A., et al. (2021). NASH limits anti-tumour surveillance in immunotherapy-treated HCC. *Nature* 592, 450–456. <https://doi.org/10.1038/s41586-021-03362-0>.
7. Goswami, S., Anandhan, S., Raychaudhuri, D., and Sharma, P. (2023). Myeloid cell-targeted therapies for solid tumours. *Nat. Rev. Immunol.* 23, 106–120. <https://doi.org/10.1038/s41577-022-00737-w>.
8. Zheng, C., Zheng, L., Yoo, J.K., Guo, H., Zhang, Y., Guo, X., Kang, B., Hu, R., Huang, J.Y., Zhang, Q., et al. (2017). Landscape of Infiltrating T Cells in Liver Cancer Revealed by Single-Cell Sequencing. *Cell* 169, 1342–1356.e16. <https://doi.org/10.1016/j.cell.2017.05.035>.
9. Zhang, Q., He, Y., Luo, N., Patel, S.J., Han, Y., Gao, R., Modak, M., Carotta, S., Haslinger, C., Kind, D., et al. (2019). Landscape and Dynamics of Single Immune Cells in Hepatocellular Carcinoma. *Cell* 179, 829–845.e20. <https://doi.org/10.1016/j.cell.2019.10.003>.
10. Sharma, A., Seow, J.J.W., Dutertre, C.A., Pai, R., Blériot, C., Mishra, A., Wong, R.M.M., Singh, G.S.N., Sudhagar, S., Khalilnezhad, S., et al.

- (2020). Onco-fetal Reprogramming of Endothelial Cells Drives Immunosuppressive Macrophages in Hepatocellular Carcinoma. *Cell* 183, 377–394.e21. <https://doi.org/10.1016/j.cell.2020.08.040>.
11. Song, G., Shi, Y., Zhang, M., Goswami, S., Afridi, S., Meng, L., Ma, J., Chen, Y., Lin, Y., Zhang, J., et al. (2020). Global immune characterization of HBV/HCV-related hepatocellular carcinoma identifies macrophage and T-cell subsets associated with disease progression. *Cell Discov.* 6, 90. <https://doi.org/10.1038/s41421-020-00214-5>.
 12. Sun, Y., Wu, L., Zhong, Y., Zhou, K., Hou, Y., Wang, Z., Zhang, Z., Xie, J., Wang, C., Chen, D., et al. (2021). Single-cell landscape of the ecosystem in early-relapse hepatocellular carcinoma. *Cell* 184, 404–421.e16. <https://doi.org/10.1016/j.cell.2020.11.041>.
 13. Ma, L., Hernandez, M.O., Zhao, Y., Mehta, M., Tran, B., Kelly, M., Rae, Z., Hernandez, J.M., Davis, J.L., Martin, S.P., et al. (2019). Tumor Cell Biodiversity Drives Microenvironmental Reprogramming in Liver Cancer. *Cancer Cell* 36, 418–430.e6. <https://doi.org/10.1016/j.ccell.2019.08.007>.
 14. Ma, L., Wang, L., Khatib, S.A., Chang, C.W., Heinrich, S., Dominguez, D.A., Forgues, M., Candia, J., Hernandez, M.O., Kelly, M., et al. (2021). Single-cell atlas of tumor cell evolution in response to therapy in hepatocellular carcinoma and intrahepatic cholangiocarcinoma. *J. Hepatol.* 75, 1397–1408. <https://doi.org/10.1016/j.jhep.2021.06.028>.
 15. Hibino, S., Chikuma, S., Kondo, T., Ito, M., Nakatsukasa, H., Omata-Mise, S., and Yoshimura, A. (2018). Inhibition of Nr4a Receptors Enhances Antitumor Immunity by Breaking Treg-Mediated Immune Tolerance. *Cancer Res.* 78, 3027–3040. <https://doi.org/10.1158/0008-5472.CAN-17-3102>.
 16. Sekiya, T., Kashiwagi, I., Inoue, N., Morita, R., Hori, S., Waldmann, H., Rudensky, A.Y., Ichinose, H., Metzger, D., Chambon, P., and Yoshimura, A. (2011). The nuclear orphan receptor Nr4a2 induces Foxp3 and regulates differentiation of CD4+ T cells. *Nat. Commun.* 2, 269. <https://doi.org/10.1038/ncomms1272>.
 17. Liu, X., Wang, Y., Lu, H., Li, J., Yan, X., Xiao, M., Hao, J., Alekseev, A., Khong, H., Chen, T., et al. (2019). Genome-wide analysis identifies NR4A1 as a key mediator of T cell dysfunction. *Nature* 567, 525–529. <https://doi.org/10.1038/s41586-019-0979-8>.
 18. Seo, H., Chen, J., González-Avalos, E., Samaniego-Castruita, D., Das, A., Wang, Y.H., López-Moyado, I.F., Georges, R.O., Zhang, W., Onodera, A., et al. (2019). TOX and TOX2 transcription factors cooperate with NR4A transcription factors to impose CD8(+) T cell exhaustion. *Proc. Natl. Acad. Sci. USA* 116, 12410–12415. <https://doi.org/10.1073/pnas.1905675116>.
 19. Zhu, Y.P., Eggert, T., Araujo, D.J., Vijayanand, P., Ottensmeier, C.H., and Hedrick, C.C. (2020). CyTOF mass cytometry reveals phenotypically distinct human blood neutrophil populations differentially correlated with melanoma stage. *J. Immunother. Cancer* 8, e000473. <https://doi.org/10.1136/jitc-2019-000473>.
 20. Yáñez, A., Coetzee, S.G., Olsson, A., Muench, D.E., Berman, B.P., Hazlett, D.J., Salomonis, N., Grimes, H.L., and Goodridge, H.S. (2017). Granulocyte-Monocyte Progenitors and Monocyte-Dendritic Cell Progenitors Independently Produce Functionally Distinct Monocytes. *Immunity* 47, 890–902.e4. <https://doi.org/10.1016/j.immuni.2017.10.021>.
 21. Bill, R., Wirapati, P., Messesmaker, M., Roh, W., Zitti, B., Duval, F., Kiss, M., Park, J.C., Saal, T.M., Hoelzl, J., et al. (2023). CXCL9:SPP1 macrophage polarity identifies a network of cellular programs that control human cancers. *Science* 381, 515–524. <https://doi.org/10.1126/science.ade2292>.
 22. Nalio Ramos, R., Missolo-Koussou, Y., Gerber-Ferder, Y., Bromley, C.P., Bugatti, M., Núñez, N.G., Tosello Boari, J., Richer, W., Menger, L., Denizeau, J., et al. (2022). Tissue-resident FOLR2(+) macrophages associate with CD8(+) T cell infiltration in human breast cancer. *Cell* 185, 1189–1207.e25. <https://doi.org/10.1016/j.cell.2022.02.021>.
 23. Sadik, A., Somarribas Patterson, L.F., Öztürk, S., Mohapatra, S.R., Panitz, V., Secker, P.F., Pfänder, P., Loth, S., Salem, H., Prentzell, M.T., et al. (2020). IL411 Is a Metabolic Immune Checkpoint that Activates the AHR and Promotes Tumor Progression. *Cell* 182, 1252–1270.e34. <https://doi.org/10.1016/j.cell.2020.07.038>.
 24. Miller, J.C., Brown, B.D., Shay, T., Gautier, E.L., Jojic, V., Cohain, A., Pandey, G., Leboeuf, M., Elpek, K.G., Helft, J., et al. (2012). Deciphering the transcriptional network of the dendritic cell lineage. *Nat. Immunol.* 13, 888–899. <https://doi.org/10.1038/ni.2370>.
 25. Maier, B., Leader, A.M., Chen, S.T., Tung, N., Chang, C., LeBerichel, J., Chudnovskiy, A., Maskey, S., Walker, L., Finnigan, J.P., et al. (2020). A conserved dendritic-cell regulatory program limits antitumor immunity. *Nature* 580, 257–262. <https://doi.org/10.1038/s41586-020-2134-y>.
 26. Weinreb, C., Rodriguez-Fraticelli, A., Camargo, F.D., and Klein, A.M. (2020). Lineage tracing on transcriptional landscapes links state to fate during differentiation. *Science* 367, eaaw3381. <https://doi.org/10.1126/science.aaw3381>.
 27. Condamine, T., Dominguez, G.A., Youn, J.I., Kossenkov, A.V., Mony, S., Alicea-Torres, K., Tcyganov, E., Hashimoto, A., Nefedova, Y., Lin, C., et al. (2016). Lectin-type oxidized LDL receptor-1 distinguishes population of human polymorphonuclear myeloid-derived suppressor cells in cancer patients. *Sci. Immunol.* 1, aaf8943. <https://doi.org/10.1126/sciimmunol.aaf8943>.
 28. Veglia, F., Sanseviero, E., and Gabrilovich, D.I. (2021). Myeloid-derived suppressor cells in the era of increasing myeloid cell diversity. *Nat. Rev. Immunol.* 21, 485–498. <https://doi.org/10.1038/s41577-020-00490-y>.
 29. Travaglini, K.J., Nabhan, A.N., Penland, L., Sinha, R., Gillich, A., Sit, R.V., Chang, S., Conley, S.D., Mori, Y., Seita, J., et al. (2020). A molecular cell atlas of the human lung from single-cell RNA sequencing. *Nature* 587, 619–625. <https://doi.org/10.1038/s41586-020-2922-4>.
 30. Menyhárt, O., Nagy, Á., and Györfy, B. (2018). Determining consistent prognostic biomarkers of overall survival and vascular invasion in hepatocellular carcinoma. *R. Soc. Open Sci.* 5, 181006. <https://doi.org/10.1098/rsos.181006>.
 31. Teschendorff, A.E., and Enver, T. (2017). Single-cell entropy for accurate estimation of differentiation potency from a cell's transcriptome. *Nat. Commun.* 8, 15599. <https://doi.org/10.1038/ncomms15599>.
 32. Teschendorff, A.E., Maity, A.K., Hu, X., Weiyan, C., and Lechner, M. (2021). Ultra-fast scalable estimation of single-cell differentiation potency from scRNA-Seq data. *Bioinformatics* 37, 1528–1534. <https://doi.org/10.1093/bioinformatics/btaa987>.
 33. Bronte, V., Brandau, S., Chen, S.H., Colombo, M.P., Frey, A.B., Greten, T.F., Mandruzzato, S., Murray, P.J., Ochoa, A., Ostrand-Rosenberg, S., et al. (2016). Recommendations for myeloid-derived suppressor cell nomenclature and characterization standards. *Nat. Commun.* 7, 12150. <https://doi.org/10.1038/ncomms12150>.
 34. Lauret Marie Joseph, E., Laheurte, C., Jary, M., Boullerot, L., Asgarov, K., Gravelin, E., Bouard, A., Rangan, L., Dosset, M., Borg, C., and Adotévi, O. (2020). Immunoregulation and Clinical Implications of ANGPT2/TIE2(+) M-MDSC Signature in Non-Small Cell Lung Cancer. *Cancer Immunol. Res.* 8, 268–279. <https://doi.org/10.1158/2326-6066.CIR-19-0326>.
 35. Janikashvili, N., Trad, M., Gautheron, A., Samson, M., Lamarthée, B., Bonnefoy, F., Lemaire-Ewing, S., Ciudad, M., Rekhviashvili, K., Seaphanh, F., et al. (2015). Human monocyte-derived suppressor cells control graft-versus-host disease by inducing regulatory forkhead box protein 3-positive CD8+ T lymphocytes. *J. Allergy Clin. Immunol.* 135, 1614–1624.e4. <https://doi.org/10.1016/j.jaci.2014.12.1868>.
 36. Hegde, S., Leader, A.M., and Merad, M. (2021). MDSC: Markers, development, states, and unaddressed complexity. *Immunity* 54, 875–884. <https://doi.org/10.1016/j.immuni.2021.04.004>.
 37. Fichtner-Feigl, S., Strober, W., Kawakami, K., Puri, R.K., and Kitani, A. (2006). IL-13 signaling through the IL-13alpha2 receptor is involved in induction of TGF-beta1 production and fibrosis. *Nat. Med.* 12, 99–106. <https://doi.org/10.1038/nm1332>.
 38. Lee, C.G., Homer, R.J., Zhu, Z., Lanone, S., Wang, X., Kotliansky, V., Shipley, J.M., Gotwals, P., Noble, P., Chen, Q., et al. (2001). Interleukin-13 induces tissue fibrosis by selectively stimulating and activating transforming growth factor beta(1). *J. Exp. Med.* 194, 809–821. <https://doi.org/10.1084/jem.194.6.809>.

39. Halaby, M.J., Hezaveh, K., Lamorte, S., Ciudad, M.T., Kloetgen, A., MacLeod, B.L., Guo, M., Chakravarthy, A., Medina, T.D.S., Ugel, S., et al. (2019). GCN2 drives macrophage and MDSC function and immunosuppression in the tumor microenvironment. *Sci. Immunol.* *4*, eaax8189. <https://doi.org/10.1126/sciimmunol.aax8189>.
40. Kieffer, Y., Hocine, H.R., Gentric, G., Pelon, F., Bernard, C., Bourachot, B., Lameiras, S., Albergante, L., Bonneau, C., Guyard, A., et al. (2020). Single-Cell Analysis Reveals Fibroblast Clusters Linked to Immunotherapy Resistance in Cancer. *Cancer Discov.* *10*, 1330–1351. <https://doi.org/10.1158/2159-8290.CD-19-1384>.
41. Qi, J., Sun, H., Zhang, Y., Wang, Z., Xun, Z., Li, Z., Ding, X., Bao, R., Hong, L., Jia, W., et al. (2022). Single-cell and spatial analysis reveal interaction of FAP(+) fibroblasts and SPP1(+) macrophages in colorectal cancer. *Nat. Commun.* *13*, 1742. <https://doi.org/10.1038/s41467-022-29366-6>.
42. Steen, C.B., Liu, C.L., Alizadeh, A.A., and Newman, A.M. (2020). Profiling Cell Type Abundance and Expression in Bulk Tissues with CIBERSORTx. *Methods Mol. Biol.* *2117*, 135–157. https://doi.org/10.1007/978-1-0716-0301-7_7.
43. Grinchuk, O.V., Yenamandra, S.P., Iyer, R., Singh, M., Lee, H.K., Lim, K.H., Chow, P.K.H., and Kuznetsov, V.A. (2018). Tumor-adjacent tissue co-expression profile analysis reveals pro-oncogenic ribosomal gene signature for prognosis of resectable hepatocellular carcinoma. *Mol. Oncol.* *12*, 89–113. <https://doi.org/10.1002/1878-0261.12153>.
44. Tsukuma, H., Hiyama, T., Tanaka, S., Nakao, M., Yabuuchi, T., Kitamura, T., Nakanishi, K., Fujimoto, I., Inoue, A., Yamazaki, H., et al. (1993). Risk factors for hepatocellular carcinoma among patients with chronic liver disease. *N. Engl. J. Med.* *328*, 1797–1801. <https://doi.org/10.1056/NEJM199306243282501>.
45. Sohn, B.H., Shim, J.J., Kim, S.B., Jang, K.Y., Kim, S.M., Kim, J.H., Hwang, J.E., Jang, H.J., Lee, H.S., Kim, S.C., et al. (2016). Inactivation of Hippo Pathway Is Significantly Associated with Poor Prognosis in Hepatocellular Carcinoma. *Clin. Cancer Res.* *22*, 1256–1264. <https://doi.org/10.1158/1078-0432.CCR-15-1447>.
46. Hoshida, Y., Nijman, S.M.B., Kobayashi, M., Chan, J.A., Brunet, J.P., Chiang, D.Y., Villanueva, A., Newell, P., Ikeda, K., Hashimoto, M., et al. (2009). Integrative transcriptome analysis reveals common molecular subclasses of human hepatocellular carcinoma. *Cancer Res.* *69*, 7385–7392. <https://doi.org/10.1158/0008-5472.CAN-09-1089>.
47. Liao, R., Sun, T.W., Yi, Y., Wu, H., Li, Y.W., Wang, J.X., Zhou, J., Shi, Y.H., Cheng, Y.F., Qiu, S.J., and Fan, J. (2012). Expression of TREM-1 in hepatic stellate cells and prognostic value in hepatitis B-related hepatocellular carcinoma. *Cancer Sci.* *103*, 984–992. <https://doi.org/10.1111/j.1349-7006.2012.02273.x>.
48. Duan, M., Wang, Z.C., Wang, X.Y., Shi, J.Y., Yang, L.X., Ding, Z.B., Gao, Q., Zhou, J., and Fan, J. (2015). TREM-1, an inflammatory modulator, is expressed in hepatocellular carcinoma cells and significantly promotes tumor progression. *Ann. Surg. Oncol.* *22*, 3121–3129. <https://doi.org/10.1245/s10434-014-4191-7>.
49. Shen, Z.T., and Sigalov, A.B. (2017). Rationally designed ligand-independent peptide inhibitors of TREM-1 ameliorate collagen-induced arthritis. *J. Cell Mol. Med.* *21*, 2524–2534. <https://doi.org/10.1111/jcmm.13173>.
50. Loftus, T.J., Mohr, A.M., and Moldawer, L.L. (2018). Dysregulated myelopoiesis and hematopoietic function following acute physiologic insult. *Curr. Opin. Hematol.* *25*, 37–43. <https://doi.org/10.1097/MOH.0000000000000395>.
51. Pietras, E.M., Mirantes-Barbeito, C., Fong, S., Loeffler, D., Kovtonyuk, L.V., Zhang, S., Lakshminarasimhan, R., Chin, C.P., Techner, J.M., Will, B., et al. (2016). Chronic interleukin-1 exposure drives haematopoietic stem cells towards precocious myeloid differentiation at the expense of self-renewal. *Nat. Cell Biol.* *18*, 607–618. <https://doi.org/10.1038/ncb3346>.
52. Sica, A., Guarneri, V., and Gennari, A. (2019). Myelopoiesis, metabolism and therapy: a crucial crossroads in cancer progression. *Cell Stress* *3*, 284–294. <https://doi.org/10.15698/cst2019.09.197>.
53. Mulder, W.J.M., Ochando, J., Joosten, L.A.B., Fayad, Z.A., and Netea, M.G. (2019). Therapeutic targeting of trained immunity. *Nat. Rev. Drug Discov.* *18*, 553–566. <https://doi.org/10.1038/s41573-019-0025-4>.
54. Bouchon, A., Facchetti, F., Weigand, M.A., and Colonna, M. (2001). TREM-1 amplifies inflammation and is a crucial mediator of septic shock. *Nature* *410*, 1103–1107. <https://doi.org/10.1038/35074114>.
55. Wu, J., Li, J., Salcedo, R., Mivechi, N.F., Trinchieri, G., and Horuzsko, A. (2012). The proinflammatory myeloid cell receptor TREM-1 controls Kupffer cell activation and development of hepatocellular carcinoma. *Cancer Res.* *72*, 3977–3986. <https://doi.org/10.1158/0008-5472.CAN-12-0938>.
56. Nguyen-Lefebvre, A.T., Ajith, A., Portik-Dobos, V., Horuzsko, D.D., Arbab, A.S., Dzutsev, A., Sadek, R., Trinchieri, G., and Horuzsko, A. (2018). The innate immune receptor TREM-1 promotes liver injury and fibrosis. *J. Clin. Invest.* *128*, 4870–4883. <https://doi.org/10.1172/JCI98156>.
57. Wu, Q., Zhou, W., Yin, S., Zhou, Y., Chen, T., Qian, J., Su, R., Hong, L., Lu, H., Zhang, F., et al. (2019). Blocking Triggering Receptor Expressed on Myeloid Cells-1-Positive Tumor-Associated Macrophages Induced by Hypoxia Reverses Immunosuppression and Anti-Programmed Cell Death Ligand 1 Resistance in Liver Cancer. *Hepatology* *70*, 198–214. <https://doi.org/10.1002/hep.30593>.
58. Liu, T., Chen, S., Xie, X., Liu, H., Wang, Y., Qi, S., Shi, L., Zhou, X., Zhang, J., Wang, S., et al. (2021). Soluble TREM-1, as a new ligand for the membrane receptor Robo2, promotes hepatic stellate cells activation and liver fibrosis. *J. Cell Mol. Med.* *25*, 11113–11127. <https://doi.org/10.1111/jcmm.17033>.
59. Dosset, M., Vauchy, C., Beziaud, L., Adotevi, O., and Godet, Y. (2013). Universal tumor-reactive helper peptides from telomerase as new tools for anticancer vaccination. *Oncolimmunology* *2*, e23430. <https://doi.org/10.4161/onci.23430>.
60. Laurent, P., Allard, B., Manicki, P., Jolivel, V., Levionnois, E., Jeljeli, M., Henrot, P., Izotte, J., Leleu, D., Groppi, A., et al. (2021). TGFbeta promotes low IL10-producing ILC2 with profibrotic ability involved in skin fibrosis in systemic sclerosis. *Ann. Rheum. Dis.* *80*, 1594–1603. <https://doi.org/10.1136/annrheumdis-2020-219748>.
61. Gulati, G.S., Sikandar, S.S., Wesche, D.J., Manjunath, A., Bharadwaj, A., Berger, M.J., Ilagan, F., Kuo, A.H., Hsieh, R.W., Cai, S., et al. (2020). Single-cell transcriptional diversity is a hallmark of developmental potential. *Science* *367*, 405–411. <https://doi.org/10.1126/science.aax0249>.
62. Li, T., Fu, J., Zeng, Z., Cohen, D., Li, J., Chen, Q., Li, B., and Liu, X.S. (2020). TIMER2.0 for analysis of tumor-infiltrating immune cells. *Nucleic Acids Res.* *48*, W509–W514. <https://doi.org/10.1093/nar/gkaa407>.
63. Raudvere, U., Kolberg, L., Kuzmin, I., Arak, T., Adler, P., Peterson, H., and Vilo, J. (2019). g:Profiler: a web server for functional enrichment analysis and conversions of gene lists (2019 update). *Nucleic Acids Res.* *47*, W191–W198. <https://doi.org/10.1093/nar/gkz369>.
64. Láncozky, A., and Györfy, B. (2021). Web-Based Survival Analysis Tool Tailored for Medical Research (KMplot): Development and Implementation. *J. Med. Internet Res.* *23*, e27633. <https://doi.org/10.2196/27633>.
65. Jin, S., Guerrero-Juarez, C.F., Zhang, L., Chang, I., Ramos, R., Kuan, C.H., Myung, P., Plikus, M.V., and Nie, Q. (2021). Inference and analysis of cell-cell communication using CellChat. *Nat. Commun.* *12*, 1088. <https://doi.org/10.1038/s41467-021-21246-9>.
66. Haeussler, M., Schönig, K., Eckert, H., Eschstruth, A., Mianné, J., Renaud, J.B., Schneider-Maunoury, S., Shkumatava, A., Teboul, L., Kent, J., et al. (2016). Evaluation of off-target and on-target scoring algorithms and integration into the guide RNA selection tool CRISPOR. *Genome Biol.* *17*, 148. <https://doi.org/10.1186/s13059-016-1012-2>.
67. Denisenko, E., Guo, B.B., Jones, M., Hou, R., de Kock, L., Lassmann, T., Poppe, D., Clément, O., Simmons, R.K., Lister, R., and Forrest, A.R.R. (2020). Systematic assessment of tissue dissociation and storage biases in single-cell and single-nucleus RNA-seq workflows. *Genome Biol.* *21*, 130. <https://doi.org/10.1186/s13059-020-02048-6>.

68. McGinnis, C.S., Murrow, L.M., and Gartner, Z.J. (2019). DoubletFinder: Doublet Detection in Single-Cell RNA Sequencing Data Using Artificial Nearest Neighbors. *Cell Syst.* 8, 329–337.e4. <https://doi.org/10.1016/j.cels.2019.03.003>.
69. Germain, P., Lun, A., Macnair, W., and Robinson, M. (2021). Doublet identification in single-cell sequencing data using scdblfinder [version 1; peer review: 1 approved, 1 approved with reservations. *F1000Research* 10. <https://doi.org/10.12688/f1000research.73600.1>.
70. Bais, A.S., and Kostka, D. (2020). scds: computational annotation of doublets in single-cell RNA sequencing data. *Bioinformatics* 36, 1150–1158. <https://doi.org/10.1093/bioinformatics/btz698>.
71. Domínguez Conde, C., Xu, C., Jarvis, L.B., Rainbow, D.B., Wells, S.B., Gomes, T., Howlett, S.K., Suchanek, O., Polanski, K., King, H.W., et al. (2022). Cross-tissue immune cell analysis reveals tissue-specific features in humans. *Science* 376, eabl5197. <https://doi.org/10.1126/science.abl5197>.
72. Patil, A., and Patil, A. (2022). Cellkb immune: a manually curated database of mammalian hematopoietic marker gene sets for rapid cell type identification. Preprint at bioRxiv. <https://doi.org/10.1101/2020.12.01.389890>.
73. Kolberg, L., Raudvere, U., Kuzmin, I., Vilo, J., and Peterson, H. (2020). Gprofiler2 – an R package for gene list functional enrichment analysis and namespace conversion toolset g:profiler. *F1000Res* 9. <https://doi.org/10.12688/f1000research.24956.2>.
74. Ozisik, O., Térézol, M., and Baudot, A. (2022). orsum: a Python package for filtering and comparing enrichment analyses using a simple principle. *BMC Bioinf.* 23, 293. <https://doi.org/10.1186/s12859-022-04828-2>.
75. Cancer Genome Atlas Research Network Electronic address wheeler@bcm.edu; Cancer Genome Atlas Research Network (2017). Comprehensive and Integrative Genomic Characterization of Hepatocellular Carcinoma Electronic address, w.b.e., and Cancer Genome Atlas Research, N. *Cell* 169, 1327–1341.e23. <https://doi.org/10.1016/j.cell.2017.05.046>.
76. Pinyol, R., Torrecilla, S., Wang, H., Montironi, C., Piqué-Gili, M., Torres-Martin, M., Wei-Qiang, L., Willoughby, C.E., Ramadori, P., Andreu-Oller, C., et al. (2021). Molecular characterisation of hepatocellular carcinoma in patients with non-alcoholic steatohepatitis. *J. Hepatol.* 75, 865–878. <https://doi.org/10.1016/j.jhep.2021.04.049>.
77. Villanueva, A., Portela, A., Sayols, S., Battiston, C., Hoshida, Y., Méndez-González, J., Imbeaud, S., Letouzé, E., Hernandez-Gea, V., Cornella, H., et al. (2015). DNA methylation-based prognosis and epidrivers in hepatocellular carcinoma. *Hepatology* 61, 1945–1956. <https://doi.org/10.1002/hep.27732>.
78. Chen, S., Zhou, Y., Chen, Y., and Gu, J. (2018). fastp: an ultra-fast all-in-one FASTQ preprocessor. *Bioinformatics* 34, i884–i890. <https://doi.org/10.1093/bioinformatics/bty560>.
79. Dobin, A., Davis, C.A., Schlesinger, F., Drenkow, J., Zaleski, C., Jha, S., Batut, P., Chaisson, M., and Gingeras, T.R. (2013). STAR: ultrafast universal RNA-seq aligner. *Bioinformatics* 29, 15–21. <https://doi.org/10.1093/bioinformatics/bts635>.
80. Ewels, P., Magnusson, M., Lundin, S., and Käller, M. (2016). MultiQC: summarize analysis results for multiple tools and samples in a single report. *Bioinformatics* 32, 3047–3048. <https://doi.org/10.1093/bioinformatics/btw354>.

STAR★METHODS

KEY RESOURCES TABLE

REAGENT or RESOURCE	SOURCE	IDENTIFIER
Antibodies		
anti-Human CD14 (clone REA 599) APC-Vio770	Miltenyi	Cat#130-110-580; RRID: AB_2655062
anti-Human CD15 (clone HI98) BV786	BD Biosciences	Cat#563838; RRID:AB_2738444
anti-Human CD163 (clone REA812) PE-Vio770	Miltenyi	Cat#130-112-130; RRID:AB_2655485
anti-Human CD19 (clone REA675) APC-Vio770	Miltenyi	Cat#130-113-643; RRID:AB_2726196
anti-Human CD19 (clone REA675) PE-Vio770	Miltenyi	Cat#130-113-647; RRID:AB_2726200
anti-Human CD3 (clone REA613) APC-Vio770	Miltenyi	Cat#130-113-136; RRID:AB_2725964
anti-Human CD3 (clone HIT3a) PE	BD Biosciences	Cat#555340; RRID:AB_395746
anti-Human CD33 (clone REA 775) PE-Vio615	Miltenyi	Cat#130-111-026; RRID:AB_2657565
anti-Human CD36 (clone REA760) FITC	Miltenyi	Cat#130-110-739; RRID:AB_2657727
anti-Human CD4 (clone M-T466) PE-Vio770	Miltenyi	Cat#130-113-255; RRID:AB_2726057
anti-Human CD45 (clone H130) FITC	BioLegend	Cat#304054; RRID:AB_314393
anti-Human CD45 (clone REA747) Viogreen	Miltenyi	Cat#130-110-638; RRID:AB_2658245
anti-Human CD56 (clone REA196) APC-Vio770	Miltenyi	Cat#130-114-548; RRID:AB_2733136
anti-Human HLA-DR (clone REA805) FITC	Miltenyi	Cat#130-111-788; RRID:AB_2652156
anti-Human IFN- γ (clone REA600) APC	Miltenyi	Cat#130-113-495; RRID:AB_2751118
anti-Human LOX-1 (clone REA1188) APC	Miltenyi	Cat#130-122-111; RRID:AB_2784411
anti-Human TCR α/β (clone REA652) APC-Vio770	Miltenyi	Cat# 130-113-536; RRID:AB_2733169
anti-Human TNF- α (clone REA) FITC	Miltenyi	Cat#130-127-530; RRID:AB_2905444
anti-Human TREM1 (clone TREM-26) PE	BioLegend	Cat#314906; RRID:AB_389355
anti-Mouse TNF (clone MP6-XT22) FITC	BD Biosciences	Cat#554418; RRID:AB_395379
anti-Mouse CD4 (clone RM4-5) BV786	BD Biosciences	Cat#563727; RRID:AB_2728707
anti-Mouse CD8a (clone REA601) APC-Vio770	Miltenyi	Cat#130-120-737; RRID:AB_2752183
anti-Mouse CD3E (clone MP6-XT22) BB700	BD Biosciences	Cat#566495; RRID:AB_2744393
anti-Mouse CD45 (Clone 737) Viogreen	Miltenyi	Cat#130-110-665; RRID:AB_2658225
anti-Mouse TREM1 (clone 174031) BV421	BD Biosciences	Cat#747899; RRID:AB_2872361
anti-Mouse Ly-6G (clone REA 526) APC-Vio770	Miltenyi	Cat#130-119-126; RRID:AB_2733089
anti-Mouse Ly-6C (clone 796) BB700	Miltenyi	Cat#130-111-782; RRID:AB_2652815
anti-Mouse CD11b (clone REA 592) FITC	Miltenyi	Cat#130-113-243; RRID:AB_2726049
anti-Mouse CD49b (clone HM α 2) BV711	BD biosciences	Cat#740704; RRID:AB_2740388
anti-Mouse CD16/CD32 (clone 93)	Thermo Fisher Scientific	Cat#14-0161-83; RRID:AB_467133
Rat anti-Mouse FoxP3 (clone FJK-16s)	Thermo Fisher Scientific	Cat#14-5773-82; RRID:AB_467576
Rat anti-Mouse CD8a (clone 4SM15)	Thermo Fisher Scientific	Cat#14-0808-82; RRID:AB_2572861
Mouse anti-Human CD163 (clone 10D6)	Invitrogen	Cat#MA5-11458; RRID:AB_10982556
Mouse anti-Human CLEC4E (clone E-5)	Santa Cryz	Cat# sc-390807L
Rabbit anti-Human TREM1	LSBio	Cat#LS-C818338
anti-Human IL10 (Clone 23738)	R&D System	Cat#MAB217; RRID:AB_358064
Mouse IgG1, Isotype control (clone MOPC-21)	BioLegend	Cat# 400102; RRID:AB_2891079
Ultra-LEAF Purified anti-mouse Gr-1 Antibody (clone RB6-8C5)	BioLegend	Cat#108453; RRID:AB_2876420
Ultra-LEAF Purified anti-mouse PD1 Antibody (clone RMP1-14)	BioLegend	Cat#114122; RRID:AB_2616682
Ultra-LEAF Purified Rat IgG2a, κ Isotype Ctrl Antibody	BioLegend	Cat#400573; RRID:AB_11148951
Goat anti-Rat Alexa 568	Invitrogen	Cat# A11077; RRID:AB_2534121
anti-Human CD15 (clone HI98) BV786	BD Biosciences	Cat#563838; RRID:AB_2738444
anti-Human CD163 (clone REA812) PE-Vio770	Miltenyi	Cat#130-112-130; RRID:AB_2655485

(Continued on next page)

Continued

REAGENT or RESOURCE	SOURCE	IDENTIFIER
anti-Human CD19 (clone REA675) APC-Vio770	Miltenyi	Cat#130-113-643; RRID:AB_2726196
anti-Human CD19 (clone REA675) PE-Vio770	Miltenyi	Cat#130-113-647; RRID:AB_2726200
anti-Human CD3 (clone REA613) APC-Vio770	Miltenyi	Cat#130-113-136; RRID:AB_2725964
anti-Human CD3 (clone HIT3a) PE	BD Biosciences	Cat#555340; RRID:AB_395746
anti-Human CD33 (clone REA 775) PE-Vio615	Miltenyi	Cat#130-111-026; RRID:AB_2657565
anti-Human CD36 (clone REA760) FITC	Miltenyi	Cat#130-110-739; RRID:AB_2657727
anti-Human CD4 (clone M-T466) PE-Vio770	Miltenyi	Cat#130-113-255; RRID:AB_2726057
anti-Human CD45 (clone H130) FITC	BioLegend	Cat#304054; RRID:AB_314393
anti-Human CD45 (clone REA747) Viogreen	Miltenyi	Cat#130-110-638; RRID:AB_2658245
anti-Human CD56 (clone REA196) APC-Vio770	Miltenyi	Cat#130-114-548; RRID:AB_2733136
anti-Human HLA-DR (clone REA805) FITC	Miltenyi	Cat#130-111-788; RRID:AB_2652156
anti-Human IFN- γ (clone REA600) APC	Miltenyi	Cat#130-113-495; RRID:AB_2751118
anti-Human LOX-1 (clone REA1188) APC	Miltenyi	Cat#130-122-111; RRID:AB_2784411
anti-Human TCR α/β (clone REA652) APC-Vio770	Miltenyi	Cat# 130-113-536; RRID:AB_2733169
anti-Human TNF- α (clone REA) FITC	Miltenyi	Cat#130-127-530; RRID:AB_2905444
anti-Human TREM1 (clone TREM-26) PE	BioLegend	Cat#314906; RRID:AB_389355
anti-Mouse TNF (clone MP6-XT22) FITC	BD Biosciences	Cat#554418; RRID:AB_395379
anti-Mouse CD4 (clone RM4-5) BV786	BD Biosciences	Cat#563727; RRID:AB_2728707
anti-Mouse CD8a (clone REA601) APC-Vio770	Miltenyi	Cat#130-120-737; RRID:AB_2752183
anti-Mouse CD3E (clone MP6-XT22) BB700	BD Biosciences	Cat#566495; RRID:AB_2744393
anti-Mouse CD45 (Clone 737) Viogreen	Miltenyi	Cat#130-110-665; RRID:AB_2658225
anti-Mouse TREM1 (clone 174031) BV421	BD Biosciences	Cat#747899; RRID:AB_2872361
anti-Mouse Ly-6G (clone REA 526) APC-Vio770	Miltenyi	Cat#130-119-126; RRID:AB_2733089
anti-Mouse Ly-6C (clone 796) BB700	Miltenyi	Cat#130-111-782; RRID:AB_2652815
anti-Mouse CD11b (clone REA 592) FITC	Miltenyi	Cat#130-113-243; RRID:AB_2726049
anti-Mouse CD49b (clone HM α 2) BV711	BB biosciences	Cat#740704; RRID:AB_2740388
anti-Mouse CD16/CD32 (clone 93)	Thermo Fisher Scientific	Cat#14-0161-83; RRID:AB_467133
Rat anti-Mouse FoxP3 (clone FJK-16s)	Thermo Fisher Scientific	Cat#14-5773-82; RRID:AB_467576
Rat anti-Mouse CD8a (clone 4SM15)	Thermo Fisher Scientific	Cat#14-0808-82; RRID:AB_2572861
Mouse anti-Human CD163 (clone 10D6)	Invitrogen	Cat#MA5-11458; RRID:AB_10982556
Mouse anti-Human CLEC4E (clone E-5)	Santa Cruz	Cat#sc-390807L
Rabbit anti-Human TREM1	LSBio	Cat#LS-C818338
anti-Human IL10 (Clone 23738)	R&D System	Cat#MAB217; RRID:AB_358064
Mouse IgG1, Isotype control (clone MOPC-21)	BioLegend	Cat# 400102; RRID:AB_2891079
Ultra-LEAF Purified anti-mouse Gr-1 Antibody (clone RB6-8C5)	BioLegend	Cat#108453; RRID:AB_2876420
Ultra-LEAF Purified anti-mouse PD1 Antibody (clone RMP1-14)	BioLegend	Cat#114122; RRID:AB_2800575
Ultra-LEAF Purified Rat IgG2a, κ Isotype Ctrl Antibody	BioLegend	Cat#400573; RRID:AB_11148951
Goat anti-Rat Alexa 568	Invitrogen	Cat#A11077; RRID:AB_2534121

Biological samples

HCC and adjacent non-tumoral liver	Department of Oncology, Haut Leveque Hospital, Pessac, France	See Table S1 for details
------------------------------------	---	--

Chemicals, peptides, and recombinant proteins

GF9 peptide	Genentech	GLLSKSLVF
Control peptide	Genentech	GLLSGSLVF
UCP4 TERT Peptide	Eurofin	SLCYSILKAKNAGMS
Recombinant Human IL-6	Miltenyi	Cat#130-093-929
Recombinant Human GM-CSF	Miltenyi	Cat#130-093-862

(Continued on next page)

Continued

REAGENT or RESOURCE	SOURCE	IDENTIFIER
Phorbol 12-myristate 13-acetate	Sigma-Aldrich	Cat#79346
Ionomycin	Sigma-Aldrich	Cat#10634
rhPGLYRP1/PGRP-S	R&D system	Cat#2590-PGB-050
PGN-SA	Invivogen	Cat#tlrl-pgns2
Propylene glycol	Thermo Fisher Scientific	Cat#158720010
Isopentane RE	Carlo Erba	Cat#528492
Critical commercial assays		
Red Blood Cell Lysis Buffer	Merck	Cat#11814389001
GentleMACS C tubes	Miltenyi	Cat#130-096-334
Tumor Dissociation Kit, human	Miltenyi	Cat#130-095-929
RPMI Medium 1640 (1X)	GIBCO	Cat#22400071
DMEM Medium High Glucose	GIBCO	Cat#41965-09
DPBS without calcium without magnesium	Fisher Scientific	Cat#12559069
CO2 Independent medium	Fisher Scientific	Cat# 11580536
X-VIVO15 medium	Lonzo	Cat#BE02-060Q
Bovine Serum Albumin Fraction V (7.5%)	Fisher Scientific	Cat#11500496
EDTA 0.5 M UltraPure, pH 8.0	Fisher Scientific	Cat#15575020
Penicillin/Streptomycin	Fisher Scientific	Cat#11556461
Matrigel high concentration	BD Biosciences	Cat#354262
Sytox blue viability dye	Fisher Scientific	Cat#10482112
Viability 405/452 Fixable Dye	Miltenyi	Cat#130-110-205
BD Horizon™ Fixable Viability Stain 700	BD Biosciences	Cat#564997
7-Amino-Actinomycin D (7AAD)	BD Biosciences	Cat#559925
Opal 4-Color Manual IHC Kit	Akoya	Cat#NEL810001KT
Prolong Gold Antifade mountant	Thermo Fisher Scientific	Cat#P36930
Spectral DAPI solution	Akoya	Cat#FP1490A
10X AR9 buffer	Akoya	Cat#AR900250ML
OPAL 520	Akoya	Cat# FP1487001KT
OPAL 650	Akoya	Cat#FP1488001KT
Cell strainer 40µm	Corning	Cat#431750
Cell strainer 70µm	Corning	Cat#352350
Trypan blue solution	Sigma-Aldrich	Cat#T8154
Chromium i7 Multiplex Kit, 96 reactions	10x Genomics	Cat#120262
Chromium Next GEM Chip G Single Cell Kit	10x Genomics	Cat#1000120
Chromium Next GEM Single Cell 3' GEM, Library & Gel Bead Kit v3.1	10x Genomics	Cat#1000121
Bluing Buffer	Agilent	Cat#CS70230-2
Hematoxylin, Mayer's	Agilent	Cat#S30930-2
Eosin Y solution, aqueous	Merck	Cat# HT110219
Sodium dodecyl sulfate (SDS) solution, 10% in water	Merck	Cat# 71736
Visium Spatial Gene Expression Starter Kit	10x Genomics	Cat#1000200
Dual Index Kit TT Set A 96 rxns	10x Genomics	Cat#1000215
BSA Ultra Pure	Fischer Scientific	Cat#10743447
Methanol	Sigma-Aldrich	Cat#34860
Acetic Acid >99.9%	Sigma-Aldrich	Cat#A6283
Low TE Buffer	Fischer Scientific	Cat#12090-015
SSC Buffer 20x Concentrate	Sigma-Aldrich	Cat#S66391L
Potassium hydroxide solution volumetric, 8.0 M KOH	Sigma-Aldrich	Cat#P4494

(Continued on next page)

Continued

REAGENT or RESOURCE	SOURCE	IDENTIFIER
Hydrochloric acid solution volumetric, 0.1 M HCl	Sigma-Aldrich	Cat#2104
10% Tween 20	Biorad	Cat#1662404
Tris (1M) pH 7.0	Thermo Fisher Scientific	Cat#AM9850G
SPRISelect Reagent	Beckman Coulter	Cat#B23318
Fixation/Permeabilization Solution Kit with BD GolgiPlug	BD Biosciences	Cat#555028
16% Formaldehyde (W/V)	Fisher Scientific	Cat#11586711
RNeasy Minikit	Qiagen	Cat#74104
RNeasy Plus Micro Kit	Qiagen	Cat#74034
QIAshreader	Qiagen	Cat#79656
GoScript™ reverse transcription system	Promega	Cat#A5001
GoTaq® qPCR Master Mix	Promega	Cat#A6001
O.C.T. Compound	VWR	Cat#361603E
DNA LoBinding Tubes, 1.5 mL	Eppendorf	Cat#022431021
Irradiated MCD-Diet AIN-76	SAFE	Cat#v248
DNase I	Sigma-Aldrich	Cat#DN25
Collagenase IV	Sigma-Aldrich	Cat#C5138
Human pan T cell isolation kit	Miltenyi	Cat#130-096-535
Dynabeads human T-activator CD3/CD28	Gibco	Cat#11131D
Human CD14 ⁺ cell isolation kit	Miltenyi	130-050-201
Human IL-10 ELISA Duoset	R&D system	Cat#DY217B-05
Human sTREM1 ELISA Quantikine	R&D system	Cat#DTRM10C
CellTrace Violet system	Thermo Fisher Scientific	Cat#C34571

Deposited data

scRNA-seq raw and processed data (20 samples)	This paper	GEO:GSE245906
Spatial Visium raw and processed data (2 samples)	This paper	GEO:GSE245908
Bulk RNA-seq raw and processed data (9 samples)	This paper	GEO:GSE245905
Human reference genome NCBI build 38, GRCh38	Genome Reference Consortium	http://www.ncbi.nlm.nih.gov/projects/genome/assembly/grc/human/

Experimental models: Cell lines

Murine: Hep55.1C cells	CLS	Cat#400201
Human: TERT-specific CD4 ⁺ T cell clone	Dosset et al. ⁵⁹	N/A
Human: Fibroblasts	Laurent et al. ⁶⁰	N/A

Experimental models: Organisms/strains

Mouse: C57BL/6J SPF	Charles River	Cat#632
---------------------	---------------	---------

Oligonucleotides

sgRNA#5 target for TREM1	Integrated DNA Technology	5'-GTTTCGATCGCATCCGCTTGG-3'
sgRNA#6 target for TREM1	Integrated DNA Technology	5'-CAGCTCGGAGTTCTATAAGC-3'
Primers for <i>COL1A1</i> , <i>RPL0</i> , <i>18S</i> , <i>TGFB1</i> , <i>TIMP1</i> , <i>TREM1</i> and <i>IL10</i>	This paper	See STAR Methods details for primer sequence

Software and algorithms

Biorender	N/A	https://www.biorender.com/
DIVA	BD Biosciences	https://www.bdbiosciences.com/en-fr
FlowJo v.10.5.3	FlowJo	https://www.flowjo.com
NDP View2	Hamamatsu	https://www.hamamatsu.com
GraphPad Prism 9	GraphPad	https://www.graphpad.com/scientific-software/prism/
Adobe Illustrator	Adobe	www.adobe.com

(Continued on next page)

Continued

REAGENT or RESOURCE	SOURCE	IDENTIFIER
Cell Ranger v6.0.0	10X Genomics	https://support.10xgenomics.com/single-cell-gene-expression/software/overview/welcome
Space Ranger v1.3.0	10X Genomics	https://support.10xgenomics.com/single-cell-gene-expression/software/overview/welcome
R 4.0.0	The R core Team	https://www.r-project.org
CellTypist	Dominguez Conde et al. ⁷¹	https://github.com/Teichlab/celltypist
BBrowser BioTuring	https://www.biorxiv.org/content/10.1101/2020.12.11.414136v1	https://bioturing.com/bbrowser
Python 3.6	Python Software Foundation	https://www.python.org
CytoTRACE	Gulati et al. ⁶¹	https://cytotrace.stanford.edu/
CIBERSORTx	Steen et al. ⁴²	https://cibersort.stanford.edu/
TIMER2.0	Li et al. ⁶²	http://timer.cistrome.org/
g:Profiler	Raudvere et al. ⁶³	https://biit.cs.ut.ee/gprofiler/gost
Kaplan-Meier plotter	Lanczky et al. ⁶⁴	https://kmplot.com/analysis/
CellChat v2 R package	Jin et al. ⁶⁵	http://www.cellchat.org/
Other		
NanoZoomer 2.0HT	Hamamatsu	N/A

RESOURCE AVAILABILITY

Lead contact

Further information and requests for resources and reagents should be directed to and will be fulfilled by the lead contact Dr. Maya Saleh (maya.saleh@inrs.ca).

Materials availability

This study did not generate new unique reagents.

Data and code availability

- Single-cell RNA-seq, spatial transcriptomic and bulk RNA-seq data have been deposited at GEO with accession number GSE245909 and are publicly available as of the date of publication. Subseries accession numbers are listed in the [key resources table](#).
- This paper does not report original code.
- Any additional information required to reanalyze the data reported in this paper is available from the [lead contact](#) upon request.

EXPERIMENTAL MODEL AND STUDY PARTICIPANT DETAILS

Study participants

The adjacent non-tumoral (NT) and tumoral (HCC) tissues were obtained from patients undergoing liver resection surgery at the Haut Leveque Hospital (Pessac, France). The patients' sex (9 men and 1 woman), age range in years (60–85) and detailed clinical characteristics are summarized in [Table S1](#). Gender information was not provided. Patients were informed about the secondary use of their data and their tissue samples for research purposes, and gave consent. This study was approved by the Health and Research Ethics Center of Bordeaux (reference CER-BDX 2024 - 10).

Animal models

The mice used in this study were male C57BL/6J purchased from Charles River at 8–10 weeks of age. Mice were housed under specific pathogen-free conditions at the animal facility at Pessac (University of Bordeaux). All experimental procedures were approved by the local ethical committee in accordance with the regulations of the French ministry. Mice were housed in a controlled environment with specific pathogen-free conditions of 20°C–22°C, 12 h light/12 h dark cycle, 50–70% humidity. The food and water were provided *ad libitum*. Mice were randomly assigned to experimental groups and conditions before starting experiments.

Cell culture

Hep55.1C murine syngenic cell-line was obtained from the CLS Collection and grown in DMEM, high glucose, GlutaMAX Supplement, pyruvate (Fisher 11594446) supplemented with fetal bovine serum (FBS, 10%) and penicillin/streptomycin (1%). UCP4-specific CD4⁺ T cells were cultured as previously reported.⁵⁹ Fibroblasts were obtained from skin reduction mammaplasties and were isolated and cultured according to.⁶⁰ Human peripheral blood mononuclear cells were isolated from blood donors at the local Blood transfusion center (University Hospital, Bordeaux, agreement n° 16PLER023). All cell-lines were grown at 37°C in a humidified chamber with 5% CO₂ and regularly tested as negative for mycoplasma.

METHOD DETAILS

Generation of HuMoSCs

HuMoSCs were generated according to a published protocol.³⁵ Briefly, healthy donor PBMC were obtained from buffy coats by the means of Ficoll density gradient centrifugation. Monocytes were then isolated from PBMC by magnetic cell sorting (human CD14⁺ cell isolation kit; Miltenyi Biotec, 130-050-201). HuMoSCs were generated by incubating monocytes (1.10⁶ cells/mL) in RPMI 1640 supplemented with 10% FBS, 1% glutamine, pyruvate, HEPES, non-essential amino acid and recombinant human GM-CSF (10 ng/mL; Miltenyi Biotec, 130-093-862) and IL-6 (10 ng/mL; Miltenyi Biotec, 130-093-929) for 7 days. Sixty percent of the medium was replaced every 3 days. PGN/PGLYRP1 complex (2 μg/mL and 1 μg/mL, respectively) or water were added in the HuMoSC medium on day 6 for 24 h sTREM1 and IL-10 were quantified in the medium of HuMoSC cultures on day 7. Neutralizing anti-IL10 (Clone 23738) or isotype CT (clone MOPC-21) was added in the HuMoSC medium at day 6, and 15 min before PP treatment for 24 h.

CRISPR/Cas9 mediated TREM1 Knock-out

Two sgRNA target DNA sequences were designed using CRISPOR algorithm (crispor.tefor.net;⁶⁶) to target the *TREM1* gene. Corresponding Alt-R-crRNA was purchased from Integrated DNA Technologies (IDT) as well as human crRNA negative control and human crRNA positive control targeting the *HPRT* gene (IDT:1072541) and suspended to 200 μM in TE buffer. They were then equally mixed with 200 μM Alt-R-tracrRNA (IDT), annealed by heating for 5 min at 95°C and cooled to room temperature (RT). These dual gRNA were individually mixed with 10 μg of Alt-R S.p-Cas9HIF1v3 (IDT) with a 1.6 ratio of gRNA/Cas9. After 10 min at RT, 2.5 to 2.8 millions monocytes washed in PBS and suspended in 20 μL Lonza P3 solution containing 1 μL of electroporation enhancer (IDT) were added to the CRISPR mix. Program EA-100 of the 4D-Nucleofector (Lonza) was applied. Cells were then harvested in 2 mL medium and plated in 12 wells plates.

Human tissue dissociation

The tissues were collected in CO₂ independent medium (Fisher Scientific, Cat# 11580536) and kept on ice until processing within 1 h. One histological slice was fixed in 10% buffered formalin phosphate (Sigma) and paraffin-embedded. HES- and Masson's Trichrome-stained slides were reviewed by a pathologist (Figure S1). The other slice was embedded in OCT (VWR) and put in a bath of isopentane placed in a liquid nitrogen bath. The OCT-embedded tissue blocks were stored in a sealed container at -80°C until cryo-sectioning. The last tissue was rinsed in RPMI, transferred to a sterile 60 mm² tissue culture dish and cut in <2 mm³ pieces. Tissue pieces were placed in Gentle MACS C tubes and incubated in tissue dissociation solution (tumor dissociation kit, Miltenyi) using the GentleMACS dissociator (program h_TDK_2, Miltenyi). After a first step of centrifugation at 400 xg for 8 min at 4°C, dissociated cells were passed through a 40 μm filter, rinsed with complete RPMI and centrifuged at 400 xg for 5 min at 4°C. After a treatment with 5 mL red blood cell lysis (Roche) at 4°C for 5 min, cells were washed twice with PBS 2 mM EDTA 0.1% BSA (named FACS buffer) prior to counting in Trypan blue exclusion dye.

Flow cytometry staining

Dissociated cells were incubated with cell surface antibodies in FACS buffer for 25 min at 4°C in the dark or for 15 min at room temperature and washed twice before analysis. For intracellular staining of cytokines, cells were fixed and permeabilized with Fixation/Permeabilization Solution Kit according to manufacturer instructions (BD Biosciences). Viable cells were analyzed based on side scatter and viability dye. Acquisition was performed on the BD LSRFortessa. Cells from murine samples were blocked in anti-mouse CD16/32 antibody (1:200e) for 10 min at 4°C prior to addition of cell surface antibodies.

Single-cell FACS sorting

Doublet cells were double-excluded in width against forward scatter and side scatter. For scRNA-seq experiments, freshly dissociated single-cell suspensions were sorted based on this gating: FITC-CD45⁺, APC Vio770-panTCRαβ⁺ and PE Vio770-CD19⁻ cells. For the immunosuppression experiments, dissociated tumor single-cell suspensions were thawed in complete RPMI medium and incubated for 10 min at 37°C to wash out residual DMSO in media. Cells were pelleted and suspended in cold FACS buffer prior to staining with cell surface antibodies: Viogreen-CD45⁺ APC Vio770-Lin⁻ (CD3, CD19, CD56) FITC-CD36⁺ PE-Vio770-CD163^{+/-} APC-LOX-1^{+/-}. Viable cells were analyzed based on side scatter gates and Sytox blue viability dye 1:5000 (Fisher Sci.). Cells were sorted using FACS Aria II upgraded at 4°C in pre-coated (2 h at 37°C with PBS 10% FCS) 1.5 mL low binding tubes (Eppendorf)

containing either PBS-0.04% pure BSA (for scRNA-seq experiments) or complete RPMI (for co-culture experiments). Sorted cells were centrifuged at 350 xg at 4°C for 5 min and counted with trypan blue dye before being processed.

scRNA-seq

15,000 single CD45⁺panTCR $\alpha\beta$ ⁻CD19⁻ innate immunity cells were loaded into a chip to form Gel Bead-in-Emulsion in the Chromium Controller. Single-cell libraries were generated using the Single Cell 3' reagent Kit v3.1 (10X Genomics) as per the manufacturer's protocol. cDNA was amplified by 12 PCR cycles and 12 cycles were also performed for library preparation (single index PCR). Libraries were pooled and sequenced on a NovaSeq 6000.

Visium spatial gene expression processing

OCT-embedded tissue blocks were sectioned at 10 μ m thickness using Cryostar NX70 (Leica) and tumoral tissues containing RNA with a RIN \geq 7 were included in the Visium experiments. One section per patient was cut at 10 μ m thickness and placed on Visium slide capture area (10x Genomics). Slides were then processed following the 10x Genomics Visium Spatial protocol according to the manufacturer recommendations. The slides containing tissues were methanol-fixed at -20°C and processed for H&E staining and imaging. The slides were scanned using a Nanozoomer 2.0 HT (Hamamatsu Photonics France) using objective UPS APO 20X NA 0.75 combined with an additional lens 1.75X. Virtual slides were acquired with a TDI-3CCD camera. Based on tissue optimization experiments performed on HCC#20, HCC tissues were permeabilized for 12 min. cDNA was amplified by 14 PCR cycles and 14 cycles were also performed for library preparation (dual index PCR). Libraries were pooled and sequenced on a NovaSeq 6000.

Co-culture experiments

For the immunosuppression experiment, myeloid cells sorted from HCC surgical resections were pre-incubated for 4 h in round bottom 96-well plates with a TERT-reactive CD4⁺ T lymphocyte clone at a ratio of 5:1 and then stimulated for 12 h with UCP4 TERT peptides plus BD Golgi Plug each at 1 μ g/mL final concentration. For the control, T cells were stimulated with Phorbol 12-myristate 13-acetate at 12.5 ng/mL and ionomycin at 0.5 μ g/mL (Sigma). In others immunosuppression experiments with either myeloid cells sorted from HCC surgical resections or with HuMoSCs, total T lymphocytes were purified from healthy donor PBMC from buffy coats by the means of magnetic cell sorting using human pan T cell isolation kit according to manufacturer's procedure (Miltenyi Biotec; 130-096-535). The obtained T cells were then activated with anti-CD3/CD28-coated beads (Dynabeads, Life Technologies, 11131D) and co-cultured with or without myeloid cells at different ratios (T cell/HuMoSC ratio = 1:1, 1:4). In both immunosuppression tests, cells were pelleted and suspended in FACS buffer prior to staining with cell surface antibodies (CD4-PE Vio770 and CD3-APC-Vio770) solution containing fixable viability dye. After washing, fixation and permeabilization, intracellular staining with antibody against IFN γ -APC and TNF α -FITC was performed using BD fixation/Permeabilization solutions as per the manufacturer's recommendations (BD Biosciences). The % inhibition of T cell activity was calculated as: [(% TNF α ⁺ CD4⁺/or CD8⁺ T cell in the positive control stimulation i.e., with the TERT-derived peptide or with anti-CD3/CD28 antibodies) - (% TNF α ⁺ CD4⁺/or CD8⁺ T cell in the other tested wells) \times 100]/(% TNF α ⁺ CD4⁺/or CD8⁺ T cell in the positive control stimulation). In the proliferation assay, T cells were stained with CellTrace Violet Dye (Thermo Fisher Scientific Cat# C34571) according to the manufacturer's recommendations and then activated with anti-CD3/CD28-coated beads with or without HuMoSCs (ratio 3:1). After 6 days of co-culture, proliferation of CD3⁺ T cells was analyzed by flow cytometry after CD3-PE staining and addition of viability dye (7AAD).

MCD-diet mouse model

7-weeks old C57BL/6J male mice were fed a Methionine- and Choline-Deficient (MCD) diet from week 7 to week 11.5. The diet was halted 9 days between weeks 9.3 and 10.7. Tumor cells were implanted in the liver at week 10 and mice were sacrificed at 13-week of age and tumors were recovered.

Orthotopic tumor injection and tumor growth monitoring

10-weeks old C57BL/6J male mice were treated with buprenorphine s.c. at 0.1 mg/kg 30 min prior to anesthesia with isoflurane (2L/min oxygen). Laparotomy was done to expose the left lateral liver lobe and 20 μ L of Hep55.1C cells (0.25 \times 10⁶ cells) in Matrigel (7 mg/mL) suspension was gently injected under the liver capsule. A sterile Gel foam was placed on the needle track for 2 min to prevent leakage of cells. Mice were treated with GF9 or control peptide at 25 mg/kg (in 20% propylene glycol, 10% ethanol and 2% Tween 80, i.p. injection) three times a week from day 8 post inoculation of cells till sacrifice. Mice were treated with anti-Gr1 (BioLegend Cat# 108453), anti-PD1 (BioLegend Cat# 114122) or isotype control (BioLegend Cat# 400573) (i.p. injection, 200 μ g per mice) two times a week from day 8 till sacrifice. For anti-Gr1 treatment, mice were injected a first dose of 400 μ g antibodies. Tumor growth was monitored using bioluminescence on isoflurane anesthetized mice.

Mouse tumor dissociation

Mouse tumors were dissociated in Gentle MACS C tubes containing RPMI medium supplemented with 1% glutamine, 1% P/S, 50 μ L/mL DNase I and 1 mg/mL collagenase IV for 45 min at 37°C under agitation. C tubes were run in GentleMACS dissociator before and after incubation (program mLiver_3, Miltenyi). After a first step of centrifugation at 400 xg for 8 min at 4°C, dissociated cells were passed through a 70 μ m filter, rinsed with complete RPMI and centrifuged at 400 xg for 5 min at 4°C. After a treatment

with 1 mL ACK buffer (Gibco) at room temperature (RT) for 5 min, cells were washed twice with FACS buffer and processed for flow cytometry.

Immunofluorescence and multiplex Immunohistochemistry staining and imaging

3 μ m-thick formalin-fixed paraffin-embedded tissue sections were placed at 37°C overnight and then for 1 h at 60°C. The slides were deparaffinized in fresh xylene and rehydrated in decreasing concentrations of ethanol. The slides were immersed in AR9 buffer, placed in a jar and heated in a microwave for 180 s at 1000 mw until the buffer boils, followed by an additional microwave treatment for 30 min at 160 mw. Slides were allowed to cool down for 30 min at room temperature, rinsed with PBS and blocked in PBS 10% FCS and 1% BSA for 30 min at room temperature. Primary antibody diluted in PBS 10% FCS (CD8a, 1:400e; FoxP3, 1:100) were incubated 1 h at 37°C. After washing twice in PBS, secondary antibody (Alexa 568, 1:300e) was incubated at room temperature for 30 min. Multiplex IHC was performed according to manufacturer's recommendation (Akoya). Primary antibodies (CLEC4E, 1:200e; CD163, 1:100; TREM1, 1:250) were incubated 1.5 h at RT and OPAL 520 or OPAL 650 were used at 1/200e. Slides were counterstained with spectral DAPI (Akoya) and mounted with Prolong Antifade Mountant (ThermoFisher scientific). The tissue imaging was done at the Bordeaux Imaging Center, a service unit of the CNRS-INSERM and Bordeaux University, member of the national infrastructure France BioImaging supported by the French National Research Agency (ANR-10-INBS-04). The slides were scanned using Hamamatsu NANOZOOMER 2.0HT and images were taken using objective 40X. For quantification, fluorescent objects in both channels within a fixed ROI were counted. Five ROI per mouse and 3 mice per treatment were quantified.

RNA extraction and RT-qPCR

RNA was isolated from fibroblasts or HuMoSC using the RNeasy Plus Mini Kit (Qiagen) according to the manufacturer's protocol. 100 ng of RNA was reverse transcribed (Promega) and qPCR was performed in duplicate in 384-well plate format using GoTaq qPCR Master mix with primers for human *COL1A1* (Forward [F]: 5'CCCTCCTGACGCACGG3'; Reverse [R]: 5'GTGATTGGTGGATGTCTT3'), *TGFB1* (F: 5'CTAATGGTGGAAACCCACA3'; R: 5'TATCGCCAGGAATTGTTGC3'), *TIMP1* (F: 5'CGTTATGAGATCAAGATGA3'; R: 5'CCCCTAAGGCTTGGAACCC3'), *TREM1* (F: 5'GCAGCCAGAAAGCTTGGCAGATAA3'; R: 5'ATCCACCAGCCAGGAGAATGACAA3') or *IL10* (F: 5'GAC TTTAAGGGTTACCTGG3'; R: 5'TCACATGCGCCTTGATGTC3'). The 2- $\Delta\Delta$ Ct quantification method using *RPL0* (F: 5'GCAGCATCTCAACCCCTGA3'; R: 5'CACTGGCAACATTGCGGAC3') and *18S* (F: 5'TGCCATCACTGCCATTAAG3'; R: 5' TGCTTTCCTCAACACCA CAT3') primers for normalization, was used to calculate the average mRNA expression levels.

Transcriptomic analyses of sorted innate immune cells and sorted THBS1⁺ myeloid cells – Sample preparation

Innate immune cells from six patients: HCC#17, HCC#18, HCC#19, HCC#20, HCC#23 and HCC#24 were isolated using the same sorting strategy designed for scRNA-seq experiments. THBS1⁺ M subsets were isolated according to the sorting strategy in [Figure S3E](#). Viability and single cells were verified under microscope and cells were immediately lysed in RNA extraction buffer and stored at -80°C. Sorted THBS1⁺ M cells from five HCC patients were pooled and RNA were extracted using the RNeasy Plus Micro Kit (Qiagen). Libraries were constructed using Low Input Library Prep Kit (TakaraBio) and sequenced on a NovaSeq 6000 with a run configuration of 2 × 150 bp.

scRNA-seq data processing, quality control and cleaning

A data processing summary is presented in [Figure S1C](#) and [Table S2](#). Each of the 10X Chromium single-cell Gene Expression data were pre-processed using Cell Ranger software 6.0.0, including demultiplexing, reads alignment on human reference genome assembly GRCh38 (refdata-gex-GRCh38-2020-A), barcoding and counting of unique UMI. Raw UMI count matrices were imported in R environment to perform deeper quality control steps to exclude low-quality cells. Cells containing less than 300 or more than 4,500 detected features and cells with more than 40,000 counts were discarded. Moreover, cells expressing more than 12% of mitochondrial genes or more than 15% of ribosomal genes were eliminated. A supplementary criteria was added to exclude stressed cells based on a stress response score.⁶⁷ The stress response score was calculated using AddModuleScore function from Seurat package (version 4.0.1) with the following list of genes: *FOSB*, *FOS*, *JUN*, *JUNB*, *JUND*, *ATF3*, *EGR1*, *HSPA1A*, *HSPA1B*, *HSP90AB1*, *HSPA8*, *HSPB1*, *IER3*, *IER2*, *BTG1*, *BTG2*, *DUSP1*.

Cell doublet detection and removal

Three different doublet predictions were performed using DoubletFinder (version 2.0.3),⁶⁸ scDbfFinder (version 1.7.7)⁶⁹ and scds (version 1.8.0).⁷⁰ A consensus method was applied, i.e., a cell was considered as a multiplet and discarded if identified in at least two of the three methods. On average, doublets were estimated at around 4%, ranging from 1% (sample with the lowest number of cells) to 5.8%. Cleaning and doublets removal account for 10 to 47% of the cells retrieved with Cell Ranger. Total recovery ranges from 11 to 49% ([Table S2](#)).

Normalization and data integration

The 20 pre-processed scRNA-seq data (10 adjacent non-tumoral and 10 tumoral) were normalized using SCTransform (version 0.3.2) with method = «glmGamPoi» before integration. Functions PrepSCTIntegration with 3,000 features, FindIntegrationAnchors with dims = 30, reduction = «rpca» and reference (4 samples) options, and IntegrateData from Seurat were used to integrate all 20 samples.

Unsupervised clustering, dimensionality reduction and data visualization

Unsupervised clustering, dimensionality reduction and most visualization were performed with Seurat (version 4.0.1). RunPCA function was used with 30 dimensions. The optimized number of dimensions used for RunTSNE and RunUMAP functions was automatically calculated with an in-house script. FindNeighbors and FindClusters (res = 0.5) function were used to predict the 22 clusters described in the main text. FindAllMarkers (min.pct = 0.25, logfc.threshold = 0.25) function was used to identify discriminating features between clusters.

Cell type/state annotation

Automatic and manual methods were combined to annotate as precisely as possible cell types or states: (1) expression of canonical markers were visualized and lists of discriminating markers were first manually investigated; (2) lists of markers were downloaded from Panglao database, a score method was applied using AddModuleScore and results were visualized on FeaturePlots; and (3) automatic predictions were done using CellTypist⁷¹ with the whole dataset and cellKB software⁷² using discriminating lists of markers as input.

Identification of signature genes

We defined gene signatures as the minimal number of genes allowing to discriminate a cluster from others. Top 20 discriminating genes were investigated and adjusted as necessary to refine the signatures. To validate signatures, scores were calculated using AddModuleScore and visualized using VlnPlot and FeaturePlot functions from Seurat on the different datasets. Signature specificity was calculated as the mean expression of a marker gene in a test cluster divided by the mean expression of the same gene in the cluster that expresses it at its second highest level.

Phylogenetic relationships of clusters based on gene expression

To investigate relationships between THBS1⁺ monocytes and other myeloid clusters, we removed the pDC and CYT clusters from the MNP set, and merged it with Neutro_c12 (from the innate immune dataset). We, then, selected the top 500 Highly Variable Features based on standardized variance using HVFInfo from Seurat. Finally, we used the two BuildClusterTree and PlotClusterTree functions from Seurat.

Trajectory inference

Trajectory analyses were performed using monocle (version 2.20.0) and slingshot (version 1.6.1) R packages. A reduced number of cells (n = 300) was used to increase the speed of calculation using subset function from Seurat option downsample. Differentially and temporally expressed genes were identified using differentialGeneTest function with options fullModelFormulaStr = '~Cluster' and fullModelFormulaStr = "~sm.ns(Pseudotime)", respectively.

RNA velocity estimation

Using bam files from CellRanger, we generated loom files using Velocity pipeline 63 with velocity run10x. We merged loom files of the 20 samples using loompy python package from Linnarsson Lab. We then imported the combined loom files into R and added the "spliced", "unspliced" and "ambiguous" assays into our pre-existing Seurat object. We normalized the "spliced" assay using SCTransform. Velocity estimations were calculated using RunVelocity function from Velocity.R in SeuratWrappers. Finally, we used show.velocity.on.embedding.coord function with the UMAP embedding to visualize the average velocity of nearby cells.

Estimation of differentiation potency or signaling entropy

The differentiation potency of single-cells was estimated using the SCENT package²⁹, with the provided functional gene network «net13Jun12». Normalized count matrices were log(x + 1) transformed. Signaling Entropy Rates (SR) were calculated using Correlation of Connectome and Transcriptome (CCAT) 30 with CompCCAT function, implemented in SCENT. High values indicate higher potency or signaling promiscuity/entropy (capacity to differentiate to different lineages). Furthermore, we predicted differentiation states using CytoTRACE⁶⁴. We downsampled MNP sets by using 200 cells per cluster and used the online version of CytoTRACE.

Differential expression analysis, gene ontology and gene set enrichment analysis

Differential gene expression between two clusters or between two conditions were performed using FindMarkers function from Seurat. Gene Ontology and enrichment analyses were done using gprofiler.⁷³ Filtering and visualization were done using orsum python package.⁷⁴

Pre-processing and visualization of spatial transcriptomic data

Spatial data were pre-processed and aligned using SpaceRanger software v1.3.0 with the reference human genome GRCh38 (refdata-gex-GRCh38-2020-A) to generate raw UMI count spot matrices. Raw UMI counts were normalized using SCTransform. Dimensionality reduction was performed using classical PCA and clustering was performed using Louvain clustering with FindNeighbors and FindClusters functions, as before. Signatures were spatially visualized using AddModuleScore function. Gene expression visualizations were generated using BBrowser BioTuring (Le et al. <https://www.biorxiv.org/content/10.1101/2020.12.11.414136v1>).

Spatial co-occurrence analysis

To investigate cell type co-occurrence in spatial transcriptomics, we used AddModuleScore function with cell type related signatures. We selected spots based on quantiles over a 0.9 probability as top spots scoring positive for each signature, and then defined co-localization (spots positive for two or more signatures). We used linear regression and Pearson's Chi-square (χ^2) to test the number of spots significantly enriched in multiple populations in both fibrotic and non-fibrotic regions of HCC. Fibrotic regions were also defined using the signature method.

Cell-cell communication analysis

To predict communication between THBS1⁺ M populations and CAF populations, we used CellChat v2 R package.⁶⁵ We used a subset of our MNP set including THBS1⁺ M, monocytes and macrophages. To investigate interactions with fibroblasts, we downloaded the processed count data from Qi et al.⁴¹ and only kept fibroblast populations. We used *NormalizeData()* function from Seurat package to normalize the fibroblast set before merging them with our MNP. We created a CellChat object and used the CellChatDB.human database. Default parameters were used with "triMean" average computation.

Transcriptomic source data of external cohorts

To validate the tissue distribution of MNP subsets and their association with clinical parameters, we interrogated several large cohorts of patients with HCC. We used the LIHC TCGA cohort (<https://www.cancer.gov/tcga>). Normalized count tables were downloaded using TCGAbiolinks R package⁶⁵ with GDCquery function and the following options: data.category = «Gene expression», data.type = «Gene expression quantification», platform = «Illumina HiSeq», file.type = «normalized_results». Clinical data with patient overall survival durations and tumor grades were downloaded with the GDCquery_clinic function. Supplementary clinical information of 196 patients of the LIHC cohort were retrieved from The Cancer Genome Atlas Research Network.⁷⁵ We also used a second cohort of tumor and adjacent non-tumor tissues from hepatocellular carcinoma, GSE76427.⁴³ Finally, we specifically investigated NASH and non-NASH HCC tumors using GSE164760⁷⁶ and GSE63898⁷⁷ cohorts. For these three latter cohorts, we used the GEOquery R library to download the data.

Immuno-deconvolution and cancer genomics

We estimated proportions of scRNA-seq cell subsets in the previously cited external cohorts using CIBERSORTx.⁴² We used our MNP dataset. To extract the normalized count matrix, we downsampled the number of barcodes to 200 per cell type for our MNP subsets. We built scRNA-seq signature matrices in CIBERSORTx web server. We imputed cell fractions of each immune set within each cohort described in the previous section, with option S-mode 'Batch correction'. Parsing and visualizations of the proportions were then realized using tidyverse, reshape2, ggplot2, ggsignif, pheatmap, cowplot and corplot R packages. We performed survival analyses using survminer and survival R packages. Moreover, we verified CIBERSORTx signatures for each cell-type based on signature scoring from file 'sig_inferred_refsampl.bm.K999.txt'. We extracted top-scored 100 genes per cluster. This allowed us to validate our manual signatures to identify highly specific genes.

Transcriptomic analyses of sorted innate immune cells and sorted THBS1+ monocytes – data processing and analysis

To validate the transcriptomic programs of the three THBS1⁺ myeloid populations (c0, c3, c4), we analyzed at the bulk transcriptomic level the three sequenced samples. Quality checks of the Fastq files were done using fastp 0.23.2.⁷⁸ Mapping and counting were realized using STAR 2.7.10a⁷⁹ on the human genome (Gencode v44). Mapping results were then visualized and summarized using multiQC 1.11 software.⁸⁰ Count Per Million normalization was computed on raw count matrices. Because the sequenced samples were of pooled myeloid subsets from five patients (N = 1 pool per myeloid subset), we computed further transformation to enable gene expression analyses. We used the innate immune samples as a reference transcriptome background to transform CPM values of the THBS1⁺ myeloid pools. A geometric mean of the six innate immune samples was calculated as follows: $\exp(\text{mean}(\log(x + 1)))$. Then, for each of the THBS1⁺ M pool and each feature, a ratio of (THBS1_M_CPM)/(innate Geometric Mean) was computed. Genes of interest including 'MDSC'-associated genes^{27,28} and scRNAseq-specific markers were visualized on heatmap with a Log2 transformation. To further investigate the transcriptomic programs of the three THBS1⁺ M pools, we did the following protocol independently for each THBS1⁺ M pool: 1) Z score transformation, 2) fitting of Z score distribution, and 3) right-tailed p value estimation (over-expressed features). The fitting distribution allowed us to determine significantly over-expressed features in a pool. We selected genes with a p_value < 0.01 to perform enrichment analyses using gprofiler on Z score ranked values.

QUANTIFICATION AND STATISTICAL ANALYSIS

Statistical analyses were performed with GraphPad Prism version 9 (GraphPad software) or R version 4.1. The statistical tests used are reported in the Figure Legends. n, represents the number of PBMC donors, HCC cases or mice and is reported in the Figure Legends. Cell abundance correlations were calculated using corplot (version 0.92) and Hmisc (version 4.6.0) R packages. Correlation matrix was done using cor function with pearson method and corplots were calculated using options order = "hclust". For each analysis, significant evaluation is reported in the Figure Legends. Data are presented as mean ± SEM unless otherwise indicated.

Supplemental information

THBS1⁺ myeloid cells expand in SLD hepatocellular carcinoma and contribute to immunosuppression and unfavorable prognosis through TREM1

Julie Giraud, Domitille Chalopin, Eloïse Ramel, Thomas Boyer, Atika Zouine, Marie-Alix Derieppe, Nicolas Larmonier, Olivier Adotevi, Brigitte Le Bail, Jean-Frédéric Blanc, Christophe Laurent, Laurence Chiche, Marc Derive, Macha Nikolski, and Maya Saleh

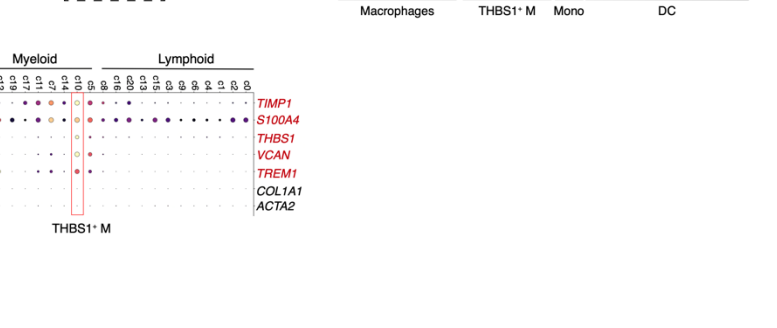
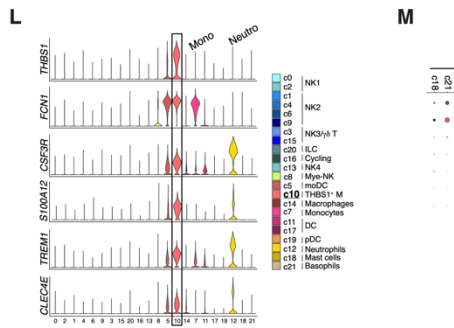
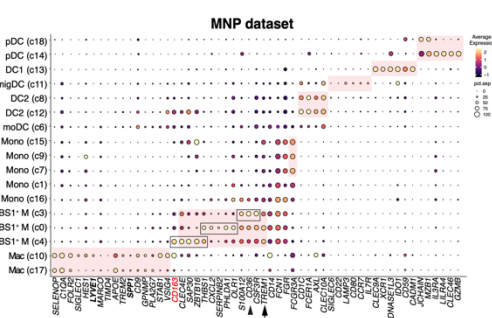
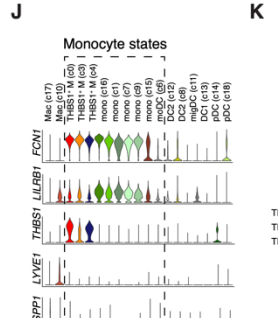
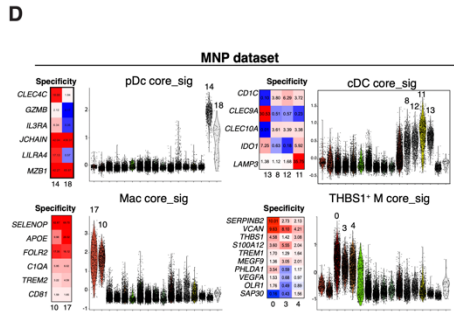
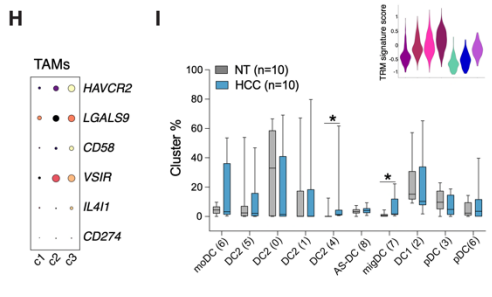
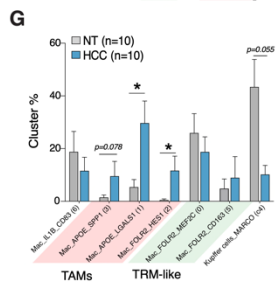
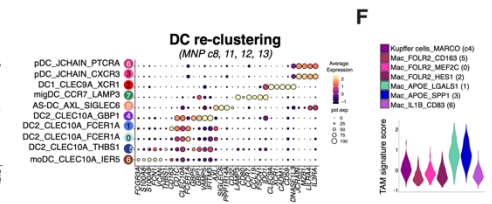
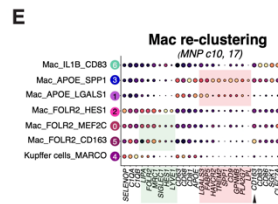
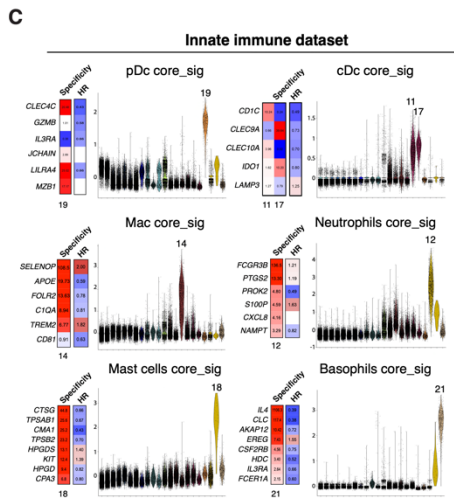
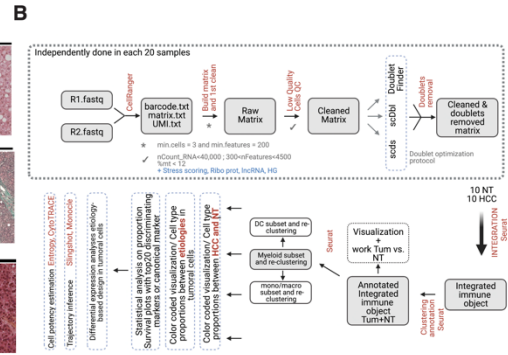
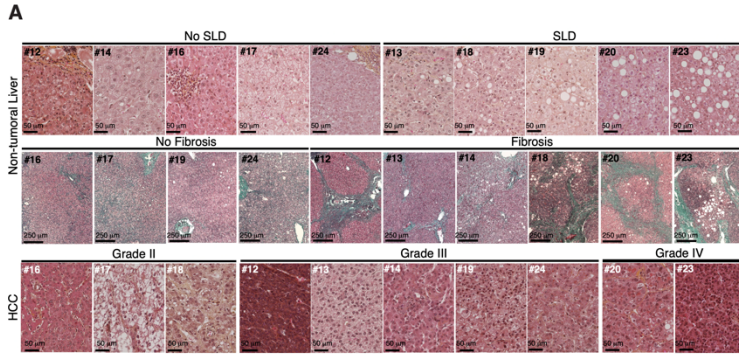


Figure S1 Related to Figure 1. Patients tissue histology and innate immune subsets gene signatures.

(A) HES and Masson's trichrome staining of non-tumoral (NT) liver and HES staining of HCC tumor sections from all patients in the study. Scale bars, 50 μ m (HES) and 250 μ m (Masson's trichrome).

(B) Pipeline of scRNA-seq bioinformatics analyses.

(C) Violin plots depicting the score per cluster of discriminating core signatures; their specificity in the innate immune dataset and association with mOS in patients with HCC from TCGA_LIHC cohort are presented. HR, hazard ratio.

(D) as in (C) but in the MNP dataset.

(E) Dot plot depicting average expression (dot color) per cluster of selected discriminating genes and percentage of cells (dot size) expressing those genes in macrophages (Mac; left) and dendritic cells (DC; right) re-clustering datasets.

(F) Violin plots depicting the score of tumor-associated macrophage (TAM) versus tissue-resident macrophage (TRM) signatures in the Mac re-clustering dataset.

(G) Macrophage cluster frequencies in the adjacent non-tumoral (NT; grey) versus HCC (blue) of the 10 patients investigated by scRNA-seq. * $p < 0.05$ using the multiple Wilcoxon test.

(H) Dot plot depicting average expression of immune checkpoint genes in TAMs.

(I) DC cluster frequencies in the adjacent NT and HCC of the 10 patients investigated by scRNA-seq. * $p < 0.05$ using the multiple Wilcoxon test.

(J) Violin plots depicting the expression per cluster of selected discriminating genes in the different MNP clusters.

(K) Dot plot depicting average expression per cluster of top discriminating genes in the MNP dataset.

(L) Violin plots depicting the expression per cluster of selected discriminating genes in the innate immune dataset.

(M) Dot plots depicting average expression and density per cluster of genes associated with fibrosis expressed in the THBS1⁺ M cluster (c10) of the innate immune dataset.

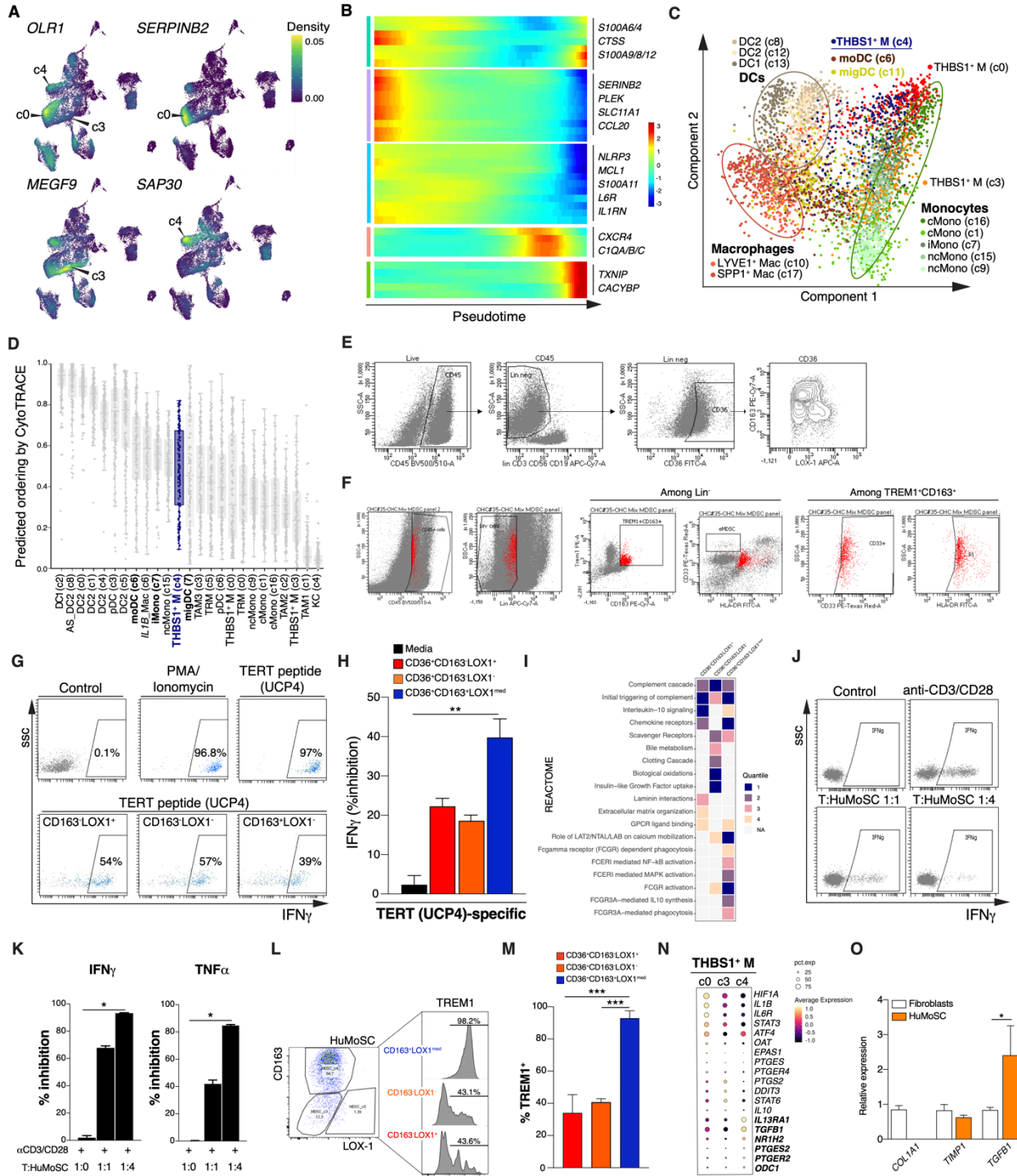


Figure S2. Related to Figure 2. Characterization of the THBS1⁺ M subsets.

- (A) Density plots using Nebulosa (R package) depicting the expression of discriminating genes of the three THBS1⁺ M clusters.
- (B) Heatmap of the top temporally expressed genes identified by Monocle2 in Figure 2i.
- (C) Principal Component Analysis of 300 cells per MNP cluster.
- (D) Predicted ordering of differentiation by CytoTRACE analysis.
- (E) Gating strategy used to sort human THBS1⁺ M subsets (c0, c3 and c4 of the MNP dataset) according to differential expression of LOX-1 and CD163 in the Lin⁻CD36^{high} population.
- (F) A conventional gating strategy used in the field to mark “MDSC”³² identifies TREM1⁺CD163⁺ myeloid cells (in red) in tumors of HCC patients.
- (G) Representative FACS scatter plots depicting intracellular IFN γ staining in TERT-specific CD4⁺ T cells stimulated or not with PMA/ionomycin or a TERT peptide (UCP4) in the presence or absence of different myeloid cell subsets sorted from HCC surgical resections according to the gating strategy in (E).
- (H) Quantification of the % inhibition of IFN γ production by CD4⁺ T cell clone stimulated with TERT peptide in co-culture with different myeloid cell subsets sorted from HCC surgical resections according to the gating strategy in (E). n=3 HCC patients. *p<0.05 using the Kruskal-Wallis test.
- (I) Heatmap representation of enriched REACTOME terms. Enrichment analysis was performed using g:profiler and REACTOME terms were filtered and ranked using Orsum python package.
- (J) Representative FACS scatter plots depicting intracellular IFN γ staining in CD3⁺ T cells stimulated or not with anti-CD3/CD28 in the presence or absence of HuMoSC at the indicated co-culture ratios.
- (K) Quantification of the % inhibition of IFN γ and TNF α production by CD3⁺ T cells stimulated with anti-CD3/CD28 in the presence or absence of HuMoSC at the indicated co-culture ratios. n=1 donor in triplicate. *p<0.05 using the Kruskal-Wallis test.
- (L) Phenotypic characterization of HuMoSC and histograms depicting TREM1 expression among the different subsets.
- (M) Quantification of the frequencies of TREM1⁺ cells among the different HuMoSC gates shown in (L). n=3 donors. ***p<0.001 using One-way Anova.
- (N) Dot plot depicting average expression of genes associated with myeloid immunosuppressive and profibrotic functions in the three THBS1⁺ M subsets.
- (O) Expression of *COL1A1*, *TIMP1* and *TGFBI* in HuMoSC and fibroblasts cultures, measured by quantitative RT-PCR. Note that *COL1A1* is barely expressed in HuMoSC. n=2 independent experiments in duplicate or triplicates. *p<0.05 using the unpaired t-test.

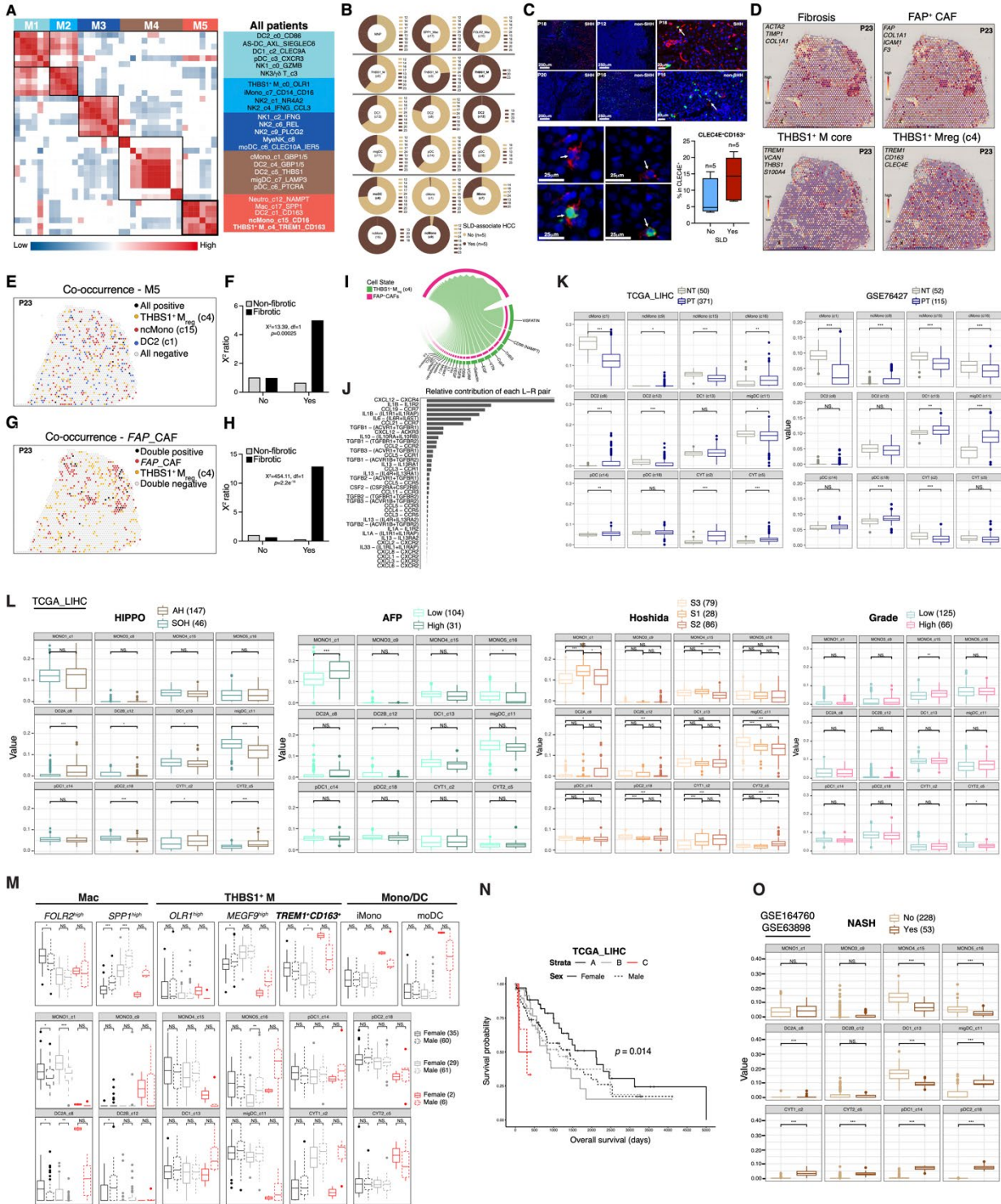


Figure S3. Related to Figure 3. Defining the innate immune populations enriched in severe HCC, associated with fibrotic lesions and expanded in the SLD setting.

(A) Cellular modules based on Pearson's correlations of cluster cell counts in the tumoral tissue and further hierarchical clustering (n=10 patients). Non-significant correlations are represented by white squares ($p > 0.05$).

(B) Donut plot depicting MNP cell proportions in HCC according to SLD positive status (brown).

(C) Epifluorescence images of HCC tumors sections stained with antibodies against CLEC4E (OPAL 520) and CD163 (OPAL 650) together with DAPI to label nuclei. n=10 HCC tumors; 5 from patients with SLD-associated HCC and 5 from patients with non-SLD-HCC.

(D) As in Figure 3C but for patient P23.

(E) As in Figure 3D but for patient P23.

(F) As in Figure 3E but for patient P23.

(G) As in Figure 3F but for patient P23.

(H) As in Figure 3G but for patient P23.

(I) Chord diagram depicting significant interaction pathways from THBS1⁺ M_{reg} (c4) as source, to FAP⁺ CAFs as target.

(J) Predicted relative contributions of each cytokine ligand (L)-receptor (R) pair in the cell-cell communication between THBS1⁺ myeloid cells and CAFs.

(K) Box plots depicting the predicted scores of MNP subsets by CIBERSORTx deconvolution of bulk transcriptomics data from two liver cancer cohorts (the TCGA_LIHC and GSE76427 cohort). NT, adjacent non-tumoral tissue; PT, primary tumor.

(L) Box plots depicting the predicted scores of MNP subsets by CIBERSORTx deconvolution of bulk transcriptomics data from the TCGA_LIHC cohort according to HIPPO status, serum AFP (<300 or >300), Hoshida class, or tumor grade (Low, pathologic T grade 1 and 2; High, pathologic T grade 3 and 4).

(M) Box plots depicting the predicted scores of MNP subsets by CIBERSORTx deconvolution of bulk transcriptomics data from the TCGA_LIHC cohort according to strata in (Figure 3J) and sex (dotted lines for female, solid lines for male).

(N) Kaplan-Meier survival curves of patients with HCC (n=193) from TCGA_LIHC cohort stratified according to the three strata in (Figure 3J) and sex.

(O) Box plots depicting the predicted scores of MNP subsets by CIBERSORTx deconvolution of bulk transcriptomics data from the GSE164760 and GSE63898 cohorts according to NASH or non-NASH tumors, using external datasets.

*** $p < 0.001$, ** $p < 0.01$, * $p < 0.05$ using Wilcoxon tests for panel (I), (J), (K) and (M).

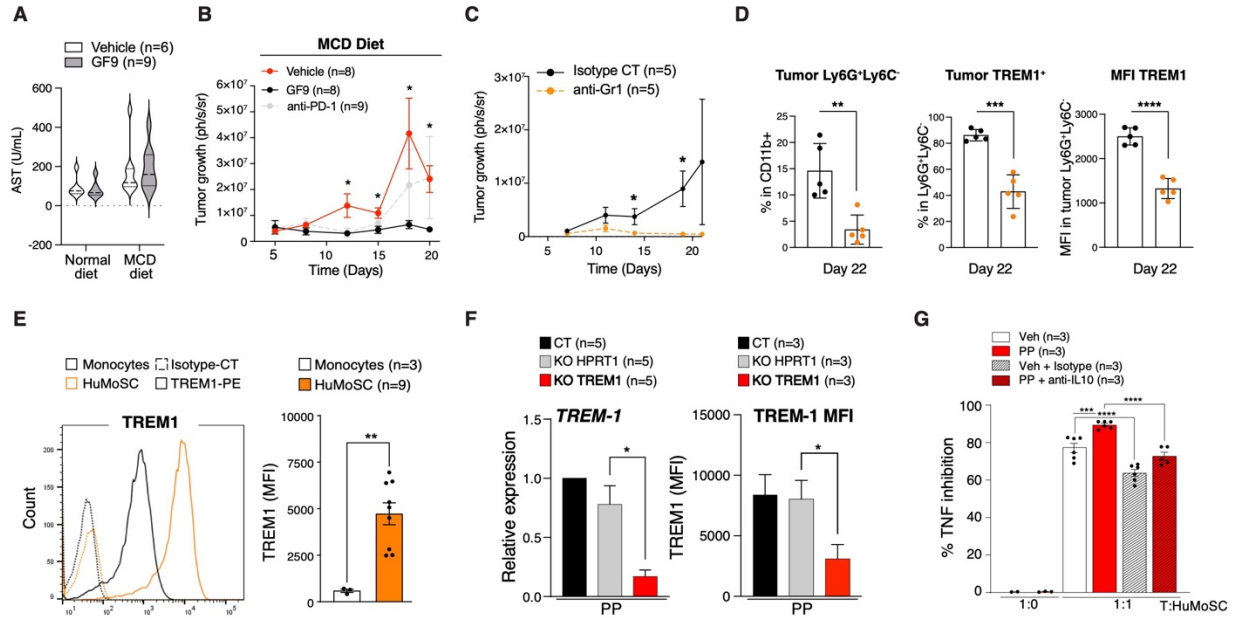


Figure S4, related to Figure 4. TREM1 expression promotes HCC tumor growth and immunosuppression.

(A) Aspartate aminotransferase (AST) serum concentration in C57BL/6J mice fed a normal or a methionine- and choline-deficient (MCD) diet.

(B) MCD diet-fed mice were treated with a vehicle control peptide, GF9 peptide, or anti-PD1 antibody. n=8 to 9 mice per condition. The data of control peptide and GF9 peptide is also shown in Figure 4F. *p<0.05 using the Mann-Whitney test comparing Vehicle to GF9.

(C) Tumor volume determined as in Figure 4E. Mice were treated with anti-Gr1 or isotype control antibody two times a week (i.p. injection). n=5 mice. *p<0.05 using the Mann-Whitney test.

(D) Percentage (%) of tumor Ly6G⁺Ly6C⁻CD11b⁺ (left panel), TREM1⁺Ly6G⁺Ly6C⁻CD11b⁺ (middle panel) and MFI (median) quantification of TREM1 in TREM1⁺Ly6G⁺Ly6C⁻CD11b⁺ (right panel) in the indicated mouse groups. Tumors were recovered on day 22 from mice in (C). n=5 mice. *p<0.05 using the unpaired t-test.

(E) FACS histograms and MFI (median) quantification of TREM1 expression on monocytes or HuMoSC on day 7 of differentiation. n=3-9 donors. **p<0.01 using the Mann-Whitney test.

(F) Expression of TREM1 in HuMoSC measured by quantitative RT-PCR (left) and MFI (median) quantification (right) on HuMoSC treated on day 6 of differentiation with PP complex for 24 hours. HuMoSC were generated from monocytes nucleofected with sgHPRT1 (grey bars), sgTREM1 (red bars) or vehicle (PBS, black bars). n=3 and 5 donors, in left and right panels, respectively. **p<0.01 and *p<0.05 using paired t-tests.

(G) Quantification of the % inhibition of TNF α production by CD3⁺ T cells stimulated with anti-CD3/CD28 with isotype control or anti-IL10 in co-culture with HuMoSC pre-treated with vehicle (water) or PP for 24 hours. n=3 donors performed in duplicates. ***p<0.001 and ****p<0.0001 using Šídák's multiple comparisons test.

TABLE S1. Patients Characteristics

HCC patients	#12	#13	#14	#16	#17	#18	#19	#20	#23	#24
Sex, male/female (m/f)	f	m	m	m	m	m	m	m	m	m
Age, years	68	63	62	85	78	78	60	74	70	69
Body Mass Index	32	39	24	22,8	19,7	25,3	32,4	26,6	30,2	31,4
INR	1.2	0.98	1.24	1.05	0.97	1.37	1.17	0.96	0.96	0.92
Bilirubin, mg/dL	11	10	16	11	9	8	44	7	10	18
Albumin level (g/L)	38.3	32	33.3	36.9	32.4	24.6	39.9	40.7	39.2	40.9
Alpha fetoprotein, ng/mL	6580	4.6	6.4	6.1	n.d.	3	96.6	78.8	3.1	4.7
Neutrophil/Lymphocyte ratio	2.60	2.42	3.04	2.97	1.76	1.17	1.34	1.82	3.10	1.56
Fibrosis (F3/F4)	yes	yes	yes	no	no	yes	no	yes	yes	no
Child Pugh Score	A	A	A	A	A	B	A	A	A	A
MELD score	8	6	9	7	7	10	12	8	7	7
Grade (Edmondson-Stainer)	III	II-III	III	II	II	II	II-III	III-IV	III-IV	II-III
Number of HCC nodules/liver; 1/2/3/>4	1	>4	1	>4	1	1	1	1	1	1
Mean largest size of HCC, mm	54 x 50 x40	72 x 72 x 60	85 x 60 x 50	38 x 33 x 30	24 x 18 x 16	27 x 25 x 22	40	95 x 60 x 50	55 x 45 x 40	19 x 17 x 10
Extrahepatic metastasis	no	no	no	no	no	no	no	no	no	no
Etiology of liver disease										
HCV/HBV	HCV	no	no	HCV	no	no	no	no	no	HCV
Alcohol	no	yes	no	no	no	no	yes	yes	no	no
Obesity	yes	yes	no	no	no	no	yes	no	yes	yes
MASH	no	yes	no	no	no	yes	no	no	yes	no
SLD	no	yes	no	no	no	yes	yes	yes	yes	no
Treatment										
Chemoembolization	yes	no	yes	no	no	yes	no	no	no	no

International normalized ratio (INR); Model for end-stage liver disease (MELD), Steatotic Liver diseases (SLD); Metabolic dysfunction-associated steatohepatitis (MASH).